AFRL-ML-WP-TR-2007-4158

A COUPLED CREEP-PLASTICITY MODEL FOR RESIDUAL STRESS RELAXATION OF A SHOT-PEENED NICKEL-BASE SUPERALLOY

Dennis Justin Buchanan

University of Dayton Research Institute
Structural Integrity Division
300 College Park
Dayton, OH 45469-0128

MAY 2007

Final Report for 01 May 2007 – 31 May 2007

Approved for public release; distribution is unlimited.

STINFO COPY

© 2007 Dennis Justin Buchanan

This work was funded in whole or in part by Department of the Air Force contract FA8650-04-C-5200. The U.S. Government has for itself and others acting on its behalf an unlimited, paid-up, nonexclusive, irrevocable worldwide license to use, modify, reproduce, release, perform, display, or disclose the work by or on behalf of the U. S. Government.

MATERIALS AND MANUFACTURING DIRECTORATE
AIR FORCE RESEARCH LABORATORY
AIR FORCE MATERIEL COMMAND
WRIGHT-PATTERSON AIR FORCE BASE, OH 45433-7750

REPORT DOCUMENTATION PAGE

Form Approved
OMB No. 0704-0188

The public reporting burden for this collection of information is estimated to average 1 hour per response, including the time for reviewing instructions, searching existing data sources, searching existing data sources, gathering and maintaining the data needed, and completing and reviewing the collection of information. Send comments regarding this burden estimate or any other aspect of this collection of information, including suggestions for reducing this burden, to Department of Defense, Washington Headquarters Services, Directorate for Information Operations and Reports (0704-0188), 1215 Jefferson Davis Highway, Suite 1204, Arlington, VA 22202-4302. Respondents should be aware that notwithstanding any other provision of law, no person shall be subject to any penalty for failing to comply with a collection of information if it does not display a currently valid OMB control number. **PLEASE DO NOT RETURN YOUR FORM TO THE ABOVE ADDRESS**.

1. REPORT DATE *(DD-MM-YY)*
May 2007

2. REPORT TYPE
Final

3. DATES COVERED *(From - To)*
01 May 2007 – 31 May 2007

4. TITLE AND SUBTITLE
A COUPLED CREEP-PLASTICITY MODEL FOR RESIDUAL STRESS RELAXATION OF A SHOT-PEENED NICKEL-BASE SUPERALLOY

5a. CONTRACT NUMBER
FA8650-04-C-5200

5b. GRANT NUMBER

5c. PROGRAM ELEMENT NUMBER
62102F

6. AUTHOR(S)
Dennis Justin Buchanan

5d. PROJECT NUMBER
4347

5e. TASK NUMBER
27

5f. WORK UNIT NUMBER
43472703

7. PERFORMING ORGANIZATION NAME(S) AND ADDRESS(ES)

University of Dayton Research Institute
Structural Integrity Division
300 College Park
Dayton, OH 45469-0128

8. PERFORMING ORGANIZATION REPORT NUMBER

9. SPONSORING/MONITORING AGENCY NAME(S) AND ADDRESS(ES)

Materials and Manufacturing Directorate
Air Force Research Laboratory
Air Force Materiel Command
Wright-Patterson AFB, OH 45433-7750

10. SPONSORING/MONITORING AGENCY ACRONYM(S)
AFRL/MLLMN

11. SPONSORING/MONITORING AGENCY REPORT NUMBER(S)
AFRL-ML-WP-TR-2007-4158

12. DISTRIBUTION/AVAILABILITY STATEMENT
Approved for public release; distribution is unlimited.

13. SUPPLEMENTARY NOTES
PAO Case Number: AFRL/WS 07-1168, 14 May 2007. Report contains color. © 2007 Dennis Justin Buchanan. This work was funded in whole or in part by Department of the Air Force contract FA8650-04-C-5200. The U.S. Government has for itself and others acting on its behalf an unlimited, paid-up, nonexclusive, irrevocable worldwide license to use, modify, reproduce, release, perform, display, or disclose the work by or on behalf of the U. S. Government.
This dissertation was submitted to The School of Engineering, University of Dayton, in partial fulfillment for a Doctor of Philosophy in Mechanical Engineering.

14. ABSTRACT
Shot peening has been employed in numerous industries for decades to impart beneficial compressive residual stresses on the surface of metal components. Compressive residual stresses retard initiation of surface cracks and therefore improve fatigue resistance and fatigue life. For elastic conditions, accurate fatigue life predictions, including credit for residual stresses, are possible for complex geometries with complicated load histories. For inelastic material behavior, shot-peened residual stresses may change continuously under cyclic loading, or elevated temperature static loading, such as thermal exposure and creep. Under inelastic conditions, taking full credit for compressive residual stresses would result in a nonconservative life prediction. As a result, designers are reluctant to incorporate any compressive residual stresses into fatigue life predictions of turbine engine components, subject to elevated temperatures and inelastic loading conditions. Identification and characterization of the underlying rate controlling deformation mechanism is required for development of a reliable relaxation model for shot-peened materials.

15. SUBJECT TERMS
relaxation model; deformation mechanism; shot peen; residual stress, fatigue, life prediction

16. SECURITY CLASSIFICATION OF:

a. REPORT	**b. ABSTRACT**	**c. THIS PAGE**	**17. LIMITATION OF ABSTRACT:**	**18. NUMBER OF PAGES**
Unclassified	Unclassified	Unclassified	SAR	128

19a. NAME OF RESPONSIBLE PERSON (Monitor)
2LT Stephen Visalli

19b. TELEPHONE NUMBER *(Include Area Code)*
(937) 255-9791

Standard Form 298 (Rev. 8-98)
Prescribed by ANSI Std. Z39-18

TABLE OF CONTENTS

LIST OF FIGURES....v

LIST OF TABLES....x

ABSTRACT....xi

ACKNOWLEDGEMENTS....xiii

LIST OF SYMBOLS....xiv

I. INTRODUCTION....1

- Problem Description....2
- Objective....3
- Significance of Research....3
- Overview....4

II. BACKGROUND AND LITERATURE REVIEW....5

- Creep and Fatigue Deformation Mechanisms and Models....6
- Shot Peening and Residual Stresses....10
- Summary of Literature Review....14

III. MODEL DEVELOPMENT....16

- Experimental Study....17
  - Material Description....18
  - Baseline Material Characterization....21
  - Residual Stress Specimen Geometry and Shot Peening....45

TABLE OF CONTENTS (concluded)

Relaxation Experiments and Analysis 49

Analytical Model Development 66

Coupled Plasticity-Creep Model..66

Model Validation and Prediction Analysis...73

IV. MODEL APPLICATION...82

Finite Element Model of Relaxation Specimen 82

Model Predictions for Residual Stress Relaxation..85

V. CONCLUSIONS AND RECOMMENDATIONS 94

Conclusions...94

Recommendations 96

REFERENCES 97

LIST OF FIGURES

1. SEM Images of IN100 Microstructure 19
2. TEM Image of Shot Peened IN100 Microstructure 20
3. Drawing of Cylindrical Dogbone Specimen Geometry 21
4. Servo-Hydraulic Test Machine used for Baseline Testing Mechanical Testing 22
5. Monotonic True Stress-True Strain for IN100 at 23°C and 650°C 24
6. Elastic Modulus of True Stress-True Strain for IN100 at 23°C 26
7. Plastic Region of True Stress-True Plastic Strain for IN100 at 23°C 27
8. Elastic Modulus of True Stress-True Strain for IN100 at 650°C 28
9. Plastic Region of True Stress-True Plastic Strain for IN100 at 650°C 29
10. Cyclic True Stress-True Strain for IN100 at 23°C 31
11. Comparison of Cyclic True Stress-True Strain for IN100 at 23°C and 650°C 32
12. Traditional Creep Strain and Creep Rate versus Time Curves 33
13. Total Strain versus Time Curves for IN100 at 650°C 34
14. Creep Rate versus Time Curves for IN100 at 650°C 35
15. Total Strain Rate versus Total Strain Curves for Virgin IN100 at 650°C 36
16. Total Strain Rate versus Total Strain for IN100 at 1000 MPa and 650°C with Different Levels of Prestrain 38
17. Total Strain Rate versus Total Strain for IN100 at 900 MPa and 650°C with Different Levels of Prestrain 39
18. Total Strain Rate versus Total Strain for IN100 at 800 MPa and 650°C with Different Levels of Prestrain 40

LIST OF FIGURES (continued)

19. Total Strain Rate versus Total Strain for IN100 at -1% 23°C Plastic Prestrain and 650°C Creep 41
20. Total Strain Rate versus Total Strain for IN100 at +1% 23°C Plastic Prestrain and 650°C Creep 42
21. Total Strain Rate versus Total Strain for IN100 at +5% 23°C Plastic Prestrain and 650°C Creep 43
22. Minimum Creep Rate versus Stress for IN100 at 650°C 44
23. Drawing of Shot Peened IN100 Flat Dogbone Geometry (All dimensions in mm) 48
24. Composite of Baseline Residual Stress and Cold Work Depth Profiles Overlaid on Shot Peened Microstructure 49
25. Variability in Baseline Residual Stress Depth Profiles in IN100 for Specimens....................51
26. Confidence Limits on Baseline Residual Stress Depth Profiles in IN100....................52
27. Schematic of Geometry and Cutout Plan for Shot Peened IN100 Thermal Relaxation Specimens and XRD Analysis....................54
28. Thermal Relaxation of Shot Peened Residual Stress Depth Profile in IN100 at 650°C Taken from Plate C1 as Shown in Table 7 56
29. Thermal Relaxation of Cold Work Depth Profile in IN100 at 650°C Taken from Plate C1 as Shown in Table 7 56
30. Stress-strain Response of Shot Peened Dogbone Specimen Subject to Fatigue Loading (σ_{max} = 900 MPa, R = 0.05) in IN100 at 650°C....................58
31. Stress-strain Response of Shot Peened Dogbone Specimen Subject to Creep Loading (σ_{max} = 900 MPa) in IN100 at 650°C....................60

LIST OF FIGURES (continued)

32. Stress-strain Response of Shot Peened Dogbone Specimen Subject to 100 hr Creep in Tension (σ_{max} = 600 MPa) and Compression (σ_{min} = -300 MPa) in IN100 at 650°C...61
33. Effect of Shot Peened Residual Stresses on Loading Stress-Strain Response in IN100 at 900 MPa and 650°C....62
34. Effect of Residual Stress on Strain versus Time Response in IN100 at 900 MPa and 650°C in Shot Peened and Virgin Samples....63
35. Stress-strain Response of Shot Peened Dogbone Specimen Subject to 10hr Creep in Tension (σ_{max} = 800 MPa, 900 MPa) in IN100 at 650°C....64
36. Effect of Residual Stress on Strain versus Time Response in IN100 at 800 & 900 MPa and 650°C in Shot Peened and Virgin Samples....65
37. Flowchart of Coupled Creep-Plasticity Model User Material Subroutine....72
38. Total Strain Rate versus Total Strain for IN100 at σ_{max} = 1000 MPa, 0% RT Prestrain, and 650°C....76
39. Total Strain Rate versus Total Strain for IN100 at σ_{max} = 1000 MPa, 1% RT Prestrain, and 650°C....76
40. Total Strain Rate versus Total Strain for IN100 at σ_{max} = 1000 MPa, 5% RT Prestrain, and 650°C....77
41. Total Strain Rate versus Total Strain for IN100 at σ_{max} = 1000 MPa, -1% RT Prestrain, and 650°C....77
42. Total Strain Rate versus Total Strain for IN100 at σ_{max} = 900 MPa, 0% RT Prestrain, and 650°C....78

LIST OF FIGURES (continued)

43. Total Strain Rate versus Total Strain for IN100 at σ_{max} = 900 MPa, 1% RT Prestrain, and 650°C 78

44. Total Strain Rate versus Total Strain for IN100 at σ_{max} = 900 MPa, 5% RT Prestrain, and 650°C 79

45. Total Strain Rate versus Total Strain for IN100 at σ_{max} = 900 MPa, -1% RT Prestrain, and 650°C 79

46. Total Strain Rate versus Total Strain for IN100 at σ_{max} = 800 MPa, 0% RT Prestrain, and 650°C 80

47. Total Strain Rate versus Total Strain for IN100 at σ_{max} = 800 MPa, 5% RT Prestrain, and 650°C 80

48. Total Strain Rate versus Total Strain for IN100 at σ_{max} = 800 MPa, -1% RT Prestrain, and 650°C 81

49. Schematic of Dogbone Specimen, Gage Section and Finite Element Geometry 83

50. Finite Element Model of Center of Gage Section used for Relaxation of Residual Stresses in Dogbone Specimens 84

51. Prediction for Retained Residual Stresses in Shot Peened Dogbone Specimen from Single Load-Unload Cycle in IN100 at 900 MPa and 650°C 86

52. Prediction for Retained Residual Stresses in Shot Peened Dogbone Specimen from 600 Cycles in IN100 at 900 MPa and 650°C 87

53. Prediction for Retained Residual Stresses in Shot Peened Dogbone Specimen from 12,000 Cycles in IN100 at 900 MPa and 650°C 88

54. Prediction for Retained Residual Stresses in Shot Peened Dogbone Specimen from 30 Min Creep in IN100 at 900 MPa and 650°C 89

LIST OF FIGURES (concluded)

55. Prediction for Retained Residual Stresses in Shot Peened Dogbone Specimen from 10 hr Creep in IN100 at 900 MPa and 650°C....................91

56. Prediction for Retained Residual Stresses in Shot Peened Dogbone Specimen from 100 hr Creep in IN100 at 600 MPa and 650°C 91

57. Prediction for Retained Residual Stresses in Shot Peened Dogbone Specimen from 100 hr Creep in IN100 at -300 MPa and 650°C 92

58. Prediction for Retained Residual Stresses in Shot Peened Dogbone Specimen from 10 hr Creep in IN100 at 800 MPa and 650°C....................93

LIST OF TABLES

1. Chemical Composition of IN100 Nickel-Base Superalloy (wt.%) 18
2. Parameters for Fit to IN100 Tensile Data at 23°C 28
3. Parameters for Fit to IN100 Tensile Data at 650°C 29
4. Creep Test Matrix for IN100 at 650°C 37
5. Minimum Creep Rates for IN100 at 650°C 44
6. Parameters for Fit of Residual Stress Depth Profile for IN100 53
7. Thermal Relaxation Test Matrix for IN100 55
8. Thermal-Mechanical Relaxation Test Matrix for IN100 57
9. Parameters in Coupled Creep-Plasticity Model for IN100 Creep Data at 650°C 81

ABSTRACT

A COUPLED CREEP-PLASTICITY MODEL FOR RESIDUAL STRESS RELAXATION OF A SHOT-PEENED NICKEL-BASE SUPERALLOY

Name: Dennis Justin Buchanan
University of Dayton, 2007

Advisor: Dr. R. A. Brockman

Shot peening has been employed in numerous industries for decades to impart beneficial compressive residual stresses on the surface of metal components. Compressive residual stresses retard initiation of surface cracks and therefore improve fatigue resistance and fatigue life. For elastic material behavior, shot-peened residual stresses remain stable under cyclic loading. Under elastic conditions, accurate fatigue life predictions, including credit for residual stresses, are possible for complex geometries with complicated load histories. For inelastic material behavior, shot-peened residual stresses may change continuously under cyclic loading, or elevated temperature static loading, such as thermal exposure and creep. Under inelastic conditions, taking full credit for compressive residual stresses would result in a nonconservative life prediction. As a result, designers are reluctant to incorporate any compressive residual stresses into fatigue life predictions of turbine engine components, subject to elevated temperatures and inelastic loading conditions. Identification and characterization of the underlying rate-controlling deformation mechanism is required for development of a reliable relaxation model for shot-peened materials. Results from this study, as well as the work of others, have shown that prior plastic strain affects creep rate, total creep deformation, and time to rupture. Creep tests on IN100 with room temperature prestrain exhibit a decrease in primary and secondary creep rate with increasing levels of prior plastic strain. Therefore, inclusion of the shot peening deformation (prior plastic strain) into a coupled creep-plasticity model is essential for accurate prediction of creep rate and residual stress relaxation. This research describes a methodical approach for characterizing and modeling residual stress relaxation under elevated temperature loading, near and above the monotonic yield strength of IN100. The approach includes strategic experiments to identify the rate-controlling deformation mechanism in creep of IN100, including the effects of prior plastic strain. The model incorporates the dominant creep deformation mechanism, coupling between the creep and plasticity model, and effects of prior plastic strain. Model predictions correlate well with experimental results on shot-peened dogbone specimens subject to cyclic and creep loading conditions at elevated temperature.

ACKNOWLEDGEMENTS

I would like to thank my advisor Dr. Robert A. Brockman for providing priceless advice, guidance, and encouragement throughout this endeavor. I would also like to thank my advisory committee for their helpful suggestions and feedback: Drs. R. John, A. H. Rosenberger, N. W. Klingbeil, and F. K. Bogner.

I am indebted to my many friends and colleagues who provided technical advice and support, specifically, Messrs. W. J. Porter, III, P. E. Blosser, M. J. Ruddell, D. J. Knapke, M. J. Swindeman, and Drs. N. E. Ashbaugh and K. Li.

My wife Bonni has been extremely supportive and patient. Her encouragement has enabled me to complete this dissertation. I also wish to thank my two daughters, Josie and Molly, who have patiently waited for me to finish “my school work”.

Finally, I would like to sincerely extend my thanks to the Materials and Manufacturing Directorate, United States Air Force Research Laboratory, Wright-Patterson, Air Force Base, OH for providing me the time and laboratory resources to complete my research.

LIST OF SYMBOLS

Symbol	**Definition**
$< x >$	Macauley bracket, < x > = 0 if x < 0, < x > = x if x ≥ 0
$\alpha_{ij}, \dot{\alpha}_{ij}$	total backstress, backstress rate tensors
$\alpha_{ij}^{c}, \dot{\alpha}_{ij}^{c}$	creep backstress, backstress rate tensors
$\alpha_{ij}^{p}, \dot{\alpha}_{ij}^{p}$	yield surface translation, translation rate tensors
$\alpha_{ij}^{r}, \dot{\alpha}_{ij}^{r}$	recovery backstress, backstress rate tensors
β	mixed isotropic-kinematic hardening parameter
C_1	plastic deformation recovery parameter
C_c	creep strain hardening parameter
δ_{ij}	Kronecker delta
ε_{ij}, e_{ij}	strain, deviatoric strain tensors
$\bar{\varepsilon}^{dm}, \dot{\bar{\varepsilon}}^{dm}$	effective dislocation mobility and rate
$\dot{\varepsilon}_o$	creep strain rate parameter
$\dot{\bar{\varepsilon}}^{c}$	effective creep strain rate
$\dot{\bar{\varepsilon}}^{p}$	effective plastic strain rate
$\dot{\varepsilon}_s$	secondary creep rate
E	Young's modulus, elastic modulus
G, μ	shear modulus
γ_c	creep strain softening parameter
H'	plastic modulus
κ	yield surface expansion
K	strain hardening coefficient
M	plastic strain rate dislocation mobility parameter
N	creep strain rate dislocation mobility parameter
n	strain hardening exponent
σ_{ij}, S_{ij}	stress, deviatoric stress tensors
σ_o	virgin yield strength
σ_κ	normalized stress parameter
$\bar{\sigma}$	effective stress
T	temperature in Kelvin
$T_h = T/T_m$	homologous temperature (absolute scale)
T_m	melting temperature in Kelvin

A COUPLED CREEP-PLASTICITY MODEL FOR RESIDUAL STRESS RELAXATION OF A SHOT-PEENED NICKEL-BASE SUPERALLOY

Dissertation

Submitted to

The School of Engineering of the

UNIVERSITY OF DAYTON

In Partial Fulfillment of the Requirements for

The Degree

Doctor of Philosophy in Mechanical Engineering

by

Dennis Justin Buchanan

UNIVERSITY OF DAYTON

Dayton, Ohio

May 2007

A COUPLED CREEP-PLASTICITY MODEL FOR RESIDUAL STRESS RELAXATION OF A SHOT-PEENED NICKEL-BASE SUPERALLOY

APPROVED BY:

Robert A. Brockman, Ph.D.
Advisory Committee Chairman
Professor, Civil & Environmental
Engineering and Engineering Mechanics

Fred K. Bogner, Ph.D.
Committee Member
Professor Emeritus, Civil &
Environmental Engineering and
Engineering Mechanics

Nathan W. Klingbeil, Ph.D.
Committee Member
Associate Professor,
Mechanical Engineering
Wright State University

Reji John, Ph.D.
Committee Member
Senior Materials Research Engineer
Wright-Patterson AFB,
AFRL/MLLMN

Andrew H. Rosenberger, Ph.D.
Committee Member
Senior Materials Research Engineer
Wright-Patterson AFB,
AFRL/MLLMN

Donald L. Moon, Ph.D.
Associate Dean,
Graduate Engineering Programs &
Research, School of Engineering

Joseph E. Saliba, Ph.D., P.E.
Dean, School of Engineering

© COPYRIGHT BY

DENNIS JUSTIN BUCHANAN

ALL RIGHTS RESERVED

2007

CHAPTER I

INTRODUCTION

The performance of any design is limited by the physical, mechanical, or thermal properties of the material. This is especially true of aircraft components where property-to-weight ratio is critical to performance. For example, stoichiometric temperatures [1] of gas turbine engines far exceed the upper usage temperature of combustor materials. Material engineers have turned toward designing materials to fit the performance requirements of intended applications. If fatigue crack growth or creep is the life-limiting deformation and damage mechanism, a large grain alloy is preferred. Large grain materials typically exhibit lower fatigue crack growth and creep strain rates than small grain materials. If yield strength or fatigue initiation is the limiting factor, fine grain alloys, with higher strength properties, are preferred. Heat treatment processes have been developed to produce microstructures that strike a balance of creep, crack initiation, and fatigue crack growth resistant properties. Many other microstructural features influence mechanical behavior including: gamma prime size, density and distribution, inclusions and porosity, carbides and grain-boundary structure. The understanding of microstructural deformation mechanisms and their effects on residual stress relaxation behavior is crucial to a life prediction model that incorporates compressive surface residual stresses from surface treatment processes.

Problem Description

In addition to the metallurgical advancements in chemistry, melting, and processing techniques, surface treatments such as shot peening (SP), low plasticity burnishing (LPB) and laser shock peening (LSP) have been employed to enhance damage tolerance by imparting compressive surface residual stresses at fracture-critical locations [2-6]. Compressive residual stresses retard crack initiation and growth, resulting in improved fatigue performance. Numerous studies [5-28] on steels, titanium and nickel-base superalloys have shown that residual stresses generated via surface treatment relax when subjected to elevated temperature exposure or mechanical loading. A variety of sophisticated empirical models have been developed and shown to capture trends in residual stress relaxation [12-14,17-18,28]. However, material microstructure, hardening behavior, plastic strain and the underlying physical deformation mechanisms responsible for stress relaxation are not incorporated into many of these models. The result is a relaxation model that must be recalibrated for each surface treatment process and associated control parameters. As a result, the beneficial effects of compressive surface residual stresses are often not incorporated into fatigue crack initiation or crack growth life prediction codes for fracture-critical locations on turbine engine components.

Surface treatment processes such as SP, LSP and LPB produce three important changes in the near surface layers of the material: (1) hardening of the material, i.e., raising the yield strength; (2) large biaxial compressive surface residual stresses constrained by small compensatory tensile stresses distributed through the bulk of the body, and (3) an unstable dislocation structure. The surface treatment deformation results in plastic strain, yield surface, and residual stress profiles that change as a function of depth from the surface. Most residual stress relaxation models in the literature only account for item (2), the initial state of residual stress in the structure.

Unfortunately, surface treatment produces a highly deformed and stressed dislocation structure that is easily perturbed by thermal exposure or mechanical loading. Items (1) and (3) must also be incorporated in the experiments and models so that residual stress relaxation of other surface treatment processes, such as LSP and LPB, can be included in a deformation mechanism based approach.

Objective

The objective of the proposed research is to develop a model for relaxation of shot peening residual stresses based on the underlying dominant physical deformation mechanism of the microstructure. The model will allow researchers and designers to evaluate and optimize surface treatment parameters to minimize relaxation of residual stresses subject to complex loading conditions for a variety of surface treatment processes. Furthermore, such a model will enable fatigue life prediction codes to take credit for any remaining compressive surface residual stresses.

Significance of Research

Turbine disks in the high pressure compressor and turbine sections of gas turbine engines may have processing residual stresses that reach a quarter of the material yield strength in bulk sections. In addition, surface treatments such as shot peening generate residual stresses 1.5 to 2 times the monotonic yield strength of the material. Features with stress concentrations, such as holes and fillets, will experience even higher stress states. Advances in other surface treatment processes such as LSP and LPB have produced deeper compressive residual stress with claims of less cold work (plastic strain). The present research provides a reliable model to predict relaxation of shot peened residual stresses under thermal and mechanical loading. Life prediction methodologies that seek to incorporate the beneficial effects of compressive residual stresses must include a relaxation model such as this to accurately determine the stresses and strains at the fracture-critical locations as a function of loading history. The success of this model is a direct result of identifying the dominant rate-controlling physical deformation mechanism behind stress relaxation in IN100. Completing strategic experiments and statistical analysis of the material parameters and model predictions provide the necessary feedback.

Overview

The Background and Literature Review chapter cites the relevant literature and describes the missing contribution of prestrain effects in creep-plasticity models for relaxation of residual stresses. The importance of integrating smart experiments, analytical modeling, and statistical analysis is highlighted in the Model Development chapter. Finally, the Model Application chapter demonstrates the capability of this model to predict residual stress relaxation in shot-peened dogbone specimens subject to a variety of mechanical loading conditions. The Conclusions and Recommendations chapter summarizes the entire study and describes new avenues for future research.

CHAPTER II

BACKGROUND AND LITERATURE REVIEW

Relaxation of residual stresses may be driven by both cyclic and sustained loads. Room temperature inelastic cyclic loading produces cyclic plastic deformation that changes the residual stress state with repeated cycles. At moderate temperatures and elastic loading conditions, residual stresses are stable with repeated cycles and sustained loading. Sustained elastic loading at elevated temperature produces time-dependent deformation (creep) that changes the residual stress state over time. The synergism between cyclic plasticity and creep deformation mechanisms at elevated temperature is complex. In many cases multiple deformation mechanisms may be active and contribute to the overall deformation rate. For severe loading conditions or extended long term exposure the microstructure may change, resulting in a path- and time-dependent degradation of material properties. Therefore, models that incorporate evolution models for the state of the microstructure are essential for capturing the relaxation of residual stresses at elevated temperature. Many of the physical damage and deformation mechanisms in metals have been identified and characterized for a range of temperatures, stresses and microstructural conditions for creep [31-34,43,49-52,55] and fatigue [31-32,43-44,56]. Many authors have investigated the effects of long term elevated temperature exposure [57-58] and grain size [53-55] as a function of stress and temperature. A review of creep and plasticity literature relevant to relaxation of shot-peened residual stresses follows.

Creep and Fatigue Deformation Mechanisms and Models

Creep deformation mechanisms in metals may be grouped into a number of broad categories depending on the author [31-35,40,49]. Under low stress and high temperature conditions bulk diffusion through the lattice (Nabarro-Herring Creep) dominates, while for low stress and moderate temperatures diffusion along grain boundaries (Coble Creep) becomes the dominant deformation mechanism. At higher stresses and low to moderate temperatures, less than 0.3 T_m, deformation is controlled by dislocation glide. For temperatures above 0.3 T_m, the mobility of vacancies allows dislocations to climb out of the current glide plane to one of less resistance, thereby increasing the creep rate. Finally, for stresses that reach the theoretical or ideal strength of the crystal, approximately equal to G/30, the material becomes unstable and fractures.

The different deformation mechanisms can be differentiated by ranges of stress, temperature and grain size over which they are dominant. Ashby [49] first displayed these graphically on Cartesian maps for a number of pure metals. The abscissas of these graphs are the homologous temperature (T_h) and the ordinates are the normalized tensile (σ/E) or shear stress (τ/G). In some cases the normalized grain size (d/b) may be the ordinate or third axis for a deformation mechanism cube.

The primary variables associated with creep deformation and creep rate are stress, temperature and time. Much of the early work characterizing creep behavior has been aimed at fitting empirical equations to a general form,

$$\varepsilon_c = F(\sigma, T, t) \qquad [1]$$

Furthermore, it has been typically assumed [36-39,41] that the functions for stress, temperature and time are separable into a product as

$$\varepsilon_c = F_1(\sigma)F_2(T)F_3(t) \qquad [2]$$

This approach has been acceptable when stress, temperature and material properties do not change with time. For variable stress and temperature loading conditions a rate formulation must be adopted. The creep strain rate equation is often cast in either a time hardening,

$$\dot{\varepsilon}_c = F_1(\sigma)F_2(T)F_3(t) \qquad [3]$$

or strain hardening formulation:

$$\dot{\varepsilon}_c = F_1(\sigma)F_2(T)F_4(\varepsilon_c) \qquad [4]$$

Both are state variable approaches that may be applied to complex thermomechanical loading histories. The time hardening formulation is somewhat cumbersome to implement in that the origin in time must be reset for each stress increment. The strain hardening approach has the additional advantage that time is not included as an independent variable in the model. For these reasons most creep analyses implement a strain hardening formulation.

A major element missing from the above creep models is the evolution of material microstructure with time or deformation history. It is almost always assumed that the microstructure and hence the material properties remain unchanged throughout the deformation history. Aspects of the material microstructure such as grain size, dislocation structure, inclusions, vacancies, etc. all have an impact on the deformation rate. Both the time hardening and strain hardening approaches are suitable if the creep rate is dominated by a single deformation mechanism. If multiple deformation mechanisms are active, or the dominant mechanism changes with thermal and mechanical loading history, simple time and strain hardening approaches fail to capture the loading response. Schoeck [31] presents a more general formulation for creep rate that accounts for multiple independent creep mechanisms in the form

$$\dot{\varepsilon}_c = \sum_i f_i(\sigma, T, st)e^{-U_i(\sigma,T,st)/kT} \qquad [5]$$

where

f_i = creep rate function (i.e., creep mechanism),

U_i = activation energy for creep mechanism,

σ = applied stress,

T = temperature,

st = structure of the material.

This formulation addresses the evolution of a changing microstructure as a contributing factor to the creep rate, but implies the deformation mechanisms are independent. Numerous models have been developed for the dominant creep mechanisms such as glide and climb of dislocations, and diffusion through grains and along grain boundaries. Nowick and Machlin [62] and Weertman [64-65] developed the early dislocation creep models to describe climb and glide deformation mechanisms which gave rise to many of the commonly used exponential and hyperbolic sine formulations for creep rate. Interaction or competition between deformation mechanisms can become complex. The Bailey-Orowan equation [31] formulates competing strain hardening and recovery mechanisms with steady state creep as a balance between mechanisms. The θ-projection [30] approach describes primary and tertiary creep using exponential forms with secondary or minimum creep rate as an inflection point in between. Initial approaches to represent material degradation under creep loading include the continuum damage mechanics (CDM) approaches of Kachanov [69] and Rabotnov [70] that incorporate a single damage parameter and associated evolution equation. More recently, the simple damage parameters in the CDM approach have been replaced by specific degradation models representing mechanisms such as cavity nucleation and growth, subgrain coarsening, multiplication of mobile dislocations, and thermally and environmentally driven mechanisms [71-79].

In contrast to creep deformation, which is a bulk mechanism that is active over the entire stressed volume, fatigue is a localized mechanism that is driven by nucleation sites such as inclusions, pores, material heterogeneity or stress risers associated with manufacturing and machining. Fatigue damage initiates at the surface where slip is less constrained and is almost always associated with a specific feature in the microstructure. The feature may be a pore, an inclusion or imperfection in the microstructure [56].

Cyclic hardening and softening appear to be related to the stability of the dislocation substructure [32]. Cyclic hardening occurs when the dislocation density increases, producing an increase in the material yield strength. Eventually a stabilized dislocation structure is reached and the hysteresis loops become stabilized. Cyclic softening results when the dislocation substructure rearranges into a less resistant configuration and the material decreases in strength. Characterizing the cyclic fatigue behavior and damage mechanisms of plastic deformation is an essential element to understanding the combined creep-fatigue behavior.

A number of modeling approaches have been developed to account for the combined contributions of plasticity and creep [71-73,80-84]. The trend has been to incorporate plasticity and creep into a single unified inelastic model. The unified models have evolved to include complex nonlinear hardening rules to capture the Bauschinger effect, and cyclic hardening or softening. Unfortunately, the microstructural deformation mechanisms behind creep and plastic deformation have been ignored in this approach.

The physical deformation and damage mechanisms of creep and fatigue in metallic materials have been reviewed. Models that have been developed to describe the physical mechanisms have also been reviewed. A thorough understanding of the material behavior and physical models of deformation and damage is essential for interpretation of measured creep response, as is selection of an appropriate model to describe creep-fatigue behavior under complex loading and temperature conditions.

Shot Peening and Residual Stresses

Shot peening has been employed for decades to impart compressive residual surface stresses for retardation of crack initiation and crack growth. Numerous studies have characterized the beneficial effects of compressive residual surface stresses on fatigue life for aluminum-, titanium- and nickel-base alloys [2-4,8-14]. For applications that utilize aluminum and titanium alloys, subjected to moderate temperatures and stresses, residual stresses are assumed to be stable with repeated cyclic stress-controlled loading. In contrast, nickel-base superalloys are typically selected for applications where temperatures may reach 80 percent of the melting temperature, and stresses approach or exceed the monotonic yield strength. At elevated temperatures and high stress loading conditions, inelastic deformation will alter the original residual stress depth profile. Further, changes to the microstructure resulting from shot peening, long term elevated temperature exposure, and deformation history may accelerate the relaxation rate of residual stresses. Understanding the relaxation of residual stresses is necessary to improve the ability to predict fatigue life of shot-peened components. Currently, designers do not account for the beneficial effect of shot peening, which sometimes results in grossly conservative design practices.

Thermal relaxation studies on shot peened steels [10-11,17-20], titanium alloys [5] and nickel alloys [5-6,13,23-25] have demonstrated that relaxation of residual stresses may occur at relatively low temperatures and over short durations. One of the early thermal residual stress relaxation studies of shot peened tool steels by Diesner [10] demonstrated that temperature and exposure time are the two driving parameters, and that the rate of relaxation could be captured with a Larson-Miller [85] type creep model. Childs [11], using shot peened 403 stainless steel Almen strips, observed relaxation at temperatures of 150°C, a quarter of the melting temperature, and for exposure times as short as one hour. Vöhringer and coworkers [17-20] recognized that in addition to temperature and exposure time, the state of the material microstructure is itself another parameter that affects relaxation rate of residual stresses. They used a Zener-Wert-Avrami [86] equation to model relaxation with exposure time, temperature and a fitting parameter that corresponded to the relaxation mechanism. Cao and colleagues [13,14] developed a thermal recovery model based on the decreasing half-width of x-ray diffraction peaks which they attributed to annihilation and reorganization of crystalline defects. The thermal recovery was modeled as a macroscopic recovery strain that was a function of time and temperature. Prevéy [5,23] has characterized thermal relaxation behavior for a number of materials and surface treatment techniques and has concluded that the rate of relaxation is correlated to the degree of cold working. Prevéy [23] claims that laser shock peening (LSP) and low plasticity burnishing (LPB), which are termed low cold work surface treatment processes, are more resistant to thermal relaxation of residual stresses than conventional shot peening. Thermal relaxation measurements made on superalloy material extracted from retired turbine disks were fit with multi-linear regression analysis by Gabb et al. [6]. Analysis of this data indicated that residual stress relaxation increases with temperature, exposure time, and level of initial cold work.

Mechanical and combined thermal and mechanical relaxation of shot peened residual stresses have been studied on steels [7,11,20,21], titanium alloys [26,87], and nickel alloys [8,12,14,24,28]. Research into relaxation of residual stresses subject to cyclic loading has followed a much different path than thermal relaxation. For thermal relaxation, temperature and exposure time are the primary parameters, while for fatigue the important factors are temperature, maximum and minimum applied stress, loading frequency, hold time, waveform shape and number of applied cycles. Many cyclic relaxation models correlate residual stress relaxation with either a power law or logarithmic function of applied cycles. For example, Landgraf and Chernenkoff [8] developed a power law model for hardened steels in which the exponent is a function of applied strain range. A more recent model by Zhuang and Halford [9] incorporates the level of cold work produced by different surface treatment processes such as LPB and LSP into the relaxation rate. Holzapfel et al. [20] describes residual stress relaxation as three different stages; (1) relaxation due to specimen heating, (2) relaxation during the first cycle, and (3) relaxation with the logarithm of cycle count. A similar approach by Cao et al. [14] describes thermomechanical relaxation as a two-stage process, in which the first stage is a shakedown of the initial residual stresses described by a monotonic stress strain law, and a second stage that is slower and is described by a cyclic softening related to the logarithm of the applied cycles. Another approach [7] performs the shakedown analysis using finite elements with a cyclic plasticity model that incorporates kinematic hardening, followed by a scheme to advance the state variables under constant amplitude loading. The above approaches have the advantage of being numerically efficient for large cycle counts. However, since they rely on the shakedown of residual stresses for constant amplitude loading, they are not appropriate for spectrum loading conditions in which periodic overloads in either tension or compression occur throughout the loading history.

For complex spectrum loading conditions, a full constitutive model that integrates the solution forward in time is necessary to capture the state of residual stress at each cycle. The most common formulation is the unified theory that incorporates plasticity, creep and recovery into a single viscoplastic model. Chaboche and Jung [28] and Ahmad et al. [12], using viscoplasticity models, predict residual stress relaxation in surface treated nickel-based superalloys at elevated temperature. The fundamental flaw in the unified models is the assumption that plasticity, creep and recovery can be combined into a single formulation. This approach contradicts experimental evidence that plasticity, creep and recovery are different deformation mechanisms and as such must be modeled separately, but possibly coupled.

Prevéy [5,23] argues that the rate of residual stress relaxation and amount of relaxation is directly correlated to the level of cold work in surface-treated Ti-6Al-4V and IN718. Prevéy's measurements on IN718 made via x-ray diffraction line broadening show that at the surface, LSP and LPB have less than 10 percent cold work, while shot peening cold work approaches 40 percent for similar peak compressive residual stresses [23]. However, shot peening cold work drops to nearly zero at a depth of 100 microns, while LPB becomes nearly zero at 1000 microns, and LSP exhibits approximately two to three percent to a depth of over 1400 microns. Clearly, the depth of plastic strain and not just the surface value contribute to the relaxation of residual stresses induced by surface treatments.

Investigations of the effects of prior room temperature prestrain on creep have been performed in copper [101], nickel [100,102] and aluminum [30]. Parker and Wilshire [101] show that tensile prestrain of five to 12.5 percent change both the primary and secondary creep rates, and that the secondary creep rate decreases with increasing levels of prestrain. The experiments were conducted at a temperature of 0.7 T_m, in which dislocation enhanced diffusion is the rate-controlling mechanism. They also conclude that the primary deformation mechanism is independent of the level of prestrain. Davies's et al. [100] investigated elevated temperature compressive prestrain of two to eleven percent on creep in pure nickel. In Davies study the elevated temperature compressive prestrain increases secondary creep rate by an amount which is independent of the level of prestrain. Evans and Wilshire [30], using two aluminum alloys, demonstrated that in one material secondary creep rate increases with increasing levels of prestrain while in another material secondary creep rate decreases with increasing levels of prestrain, for identical temperatures but different stress ranges. They reason that if the primary deformation mechanism is recovery or climb controlled, then increasing levels of prestrain would result in lower secondary creep rates. If the primary deformation mechanism is glide controlled, then increasing levels of prestrain would result in higher secondary creep rates. In all cases, prior prestrain does affect the subsequent creep rate. The experiments indicate that the level of prestrain, the direction (tensile or compressive) and the dominant deformation mechanism all contribute to whether creep rate increases or decreases with increasing levels of prestrain.

Summary of Literature Review

Knowledge of creep behavior and creep models have evolved from the simple time and temperature parameter approach to those that include detailed knowledge of the dominant deformation mechanisms, and constitutive equations that describe the evolution of the material microstructure.

Relaxation of shot-peened residual stresses for thermal exposure and fatigue loading, have been addressed in the literature. Empirical models work fairly well for predicting residual stress relaxation under constant temperature and constant amplitude loading conditions, but are generally not applicable under complex loading histories.

Relaxation of shot-peened residual stresses under sustained-load (creep) has not been addressed in the literature. This is an important area of research with practical application to gas turbine engines. High-speed rotating components, such as turbine disks, are subject to sustained stresses at elevated temperatures. Therefore, a model capable of predicting relaxation of shot peened residual stresses under sustained loading will be an important contribution to the literature and the fatigue life prediction community.

Different surface treatments such as shot peening, gravity peening, laser shock peening, low plasticity burnishing, and cavitation peening all produce different profiles of plastic strain and residual stresses, the result of very different deformation histories. Unified viscoplastic models treat creep and plasticity as the same mechanism, while the other approach treats creep and plasticity as two separate mechanisms that do not interact. Neither is correct. Clearly, understanding how plastic strain affects creep rate is the key to developing a model that can accurately predict residual stress relaxation for different surface treatment processes.

CHAPTER III

MODEL DEVELOPMENT

Numerous references cited in the literature review focus on experimental results, or analytical models. Few investigations effectively combine experiments and modeling into an integrated research approach. Furthermore, statistical analysis of the experimental data and model predictions, which is often absent, provides the essential feedback that guides effective research. The present experimental study section combines Scanning Electron Microscope (SEM) and Transmission Electronic Microscope (TEM) analysis to identify microstructural changes associated with the dominant deformation mechanism, baseline material characterization and prestrain-creep experiments necessary for model development, followed by analysis of these same behaviors in shot-peened samples which have highly localized stress and strain gradients. The analytical model development section describes the microstructure evolution equations for the dominant deformation mechanism and integration into the coupled creep-plasticity model. The remainder of the section describes the development of the ABAQUS user material subroutine, validation of the model under complex loading conditions, and statistical analysis of the model and associated microstructural parameters. This integration of strategic experiments and model development, with statistical analysis providing the feedback, is more efficient and reliable than the standard serial approach: experiment, model, predict, and done.

Experimental Study

Developing a model for relaxation of shot-peened residual stresses requires several experimental elements. First is the microstructural analysis of baseline and shot-peened samples. Comparison of the baseline and shot-peened microstructure identifies the observable changes associated with shot peening and the extent of deformation and damage to the microstructure. It also provides additional evidence to identify the list of possible deformation mechanisms behind relaxation of residual stresses. Baseline material characterization on virgin samples, and creep tests with plastic prestrain, provide deformation histories to support the development of the analytical model under uniform stress conditions. Finally, the material response of the shot peened samples, with localized stress and strain gradients from surface treatment, provides additional understanding of the material behavior under nonuniform states of stress.

Nickel-base superalloys are materials of choice for combustor and turbine sections of gas turbine engines. Superalloys are effective at maintaining stiffness, and resistance to fatigue, creep and corrosion up to approximately 80 percent of their melting temperature. In fact, material specifications for nickel-base superalloys in the High Pressure Compressor (HPC) and High Pressure Turbine (HPT) sections of the engine require that creep deformation be less than 0.2 percent at a specified sustained stress and temperature in the US Air Force Engine Structural Integrity Program handbook [105]. Powder metal (PM) nickel-base superalloys are replacing conventional cast and wrought superalloys for specific applications where increased performance is required. This is especially true in gas turbine engines where PM nickel-base superalloy disks are used in the high pressure turbine (HPT) section of the engine. For turbine engine disk applications PM superalloy production costs are reduced and are capable of near net-shape processing. Also, PM superalloys typically have a grain structure that is more uniform than cast and wrought products. However, PM processing is not without some problems. Inclusions, voids and stringers in the material act as initiation sites for low cycle fatigue damage. Bulk residual stresses resulting from manufacturing processes, combined with applied high stress-high temperature engine conditions, may exceed deformation limits during service. Surface treatments used to suppress fatigue crack initiation and crack growth may alter the creep rate. It becomes obvious that optimizing a specific material behavior may often reduce or degrade another property. Therefore, characterizing creep behavior of IN100 under expected operating conditions with prestrain is critical to understanding residual stress relaxation of surface treated materials and ultimately to the structural integrity of engine components.

Material Description

IN100 is a powder metal (PM) nickel-base superalloy. The nominal chemical composition of IN100 is listed in Table 1. IN100 has a face-centered cubic (FCC) structure with an average grain size of approximately 25μm. In FCC structures such as this IN100 alloy there are aluminum (Al) atoms at the crystal corners and nickel (Ni) in the center of each face of the crystal which make up the Ni_3Al structure.

Table 1. Chemical Composition of IN100 Nickel-Base Superalloy (wt.%)

Element	**Cr**	**Co**	**Ti**	**Al**	**Mo**	**V**	**C**	**Ni**
Composition	12.4	18.5	4.7	5.5	3.2	0.8	0.07	Bal

The microstructure is composed of a continuous gamma (γ) matrix, and precipitate cubical gamma prime (γ') shown in Figure 1, which was collected in a SEM. The cubical gamma prime is responsible for the excellent creep resistance of this alloy.

The gamma prime is strong and ductile which limits dislocation interaction and movement through the microstructure. Microstructural studies comparing IN100 samples thermally exposed for 300 hours at 704°C with baseline samples (no exposure) reveal no evidence of grain growth, no gamma prime coarsening, and no new phases detected. These same observations are also true for the heavily cold worked surface layers of the shot peened IN100 samples. Additional details about the baseline microstructure are described in the literature [99].

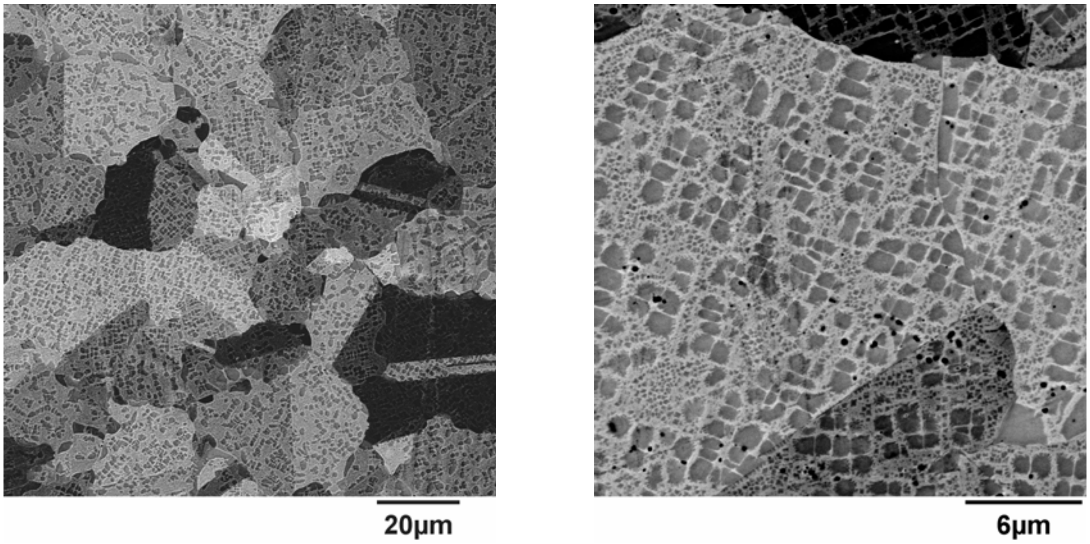

Figure 1. SEM Images of IN100 Microstructure

Observations of the dislocation structure in shot peened IN100 were completed as part of this investigation using a TEM. TEM analysis is best suited for observing dislocations when the amount of plastic strain is in the range of one to three percent. The shot peened surface has plastic strains of approximately 30 percent, and so the image details are difficult to see due to the high dislocation density. A TEM image of a foil from the shot peened surface is shown in Figure 2. The lower left corner shows open space and the edge of the TEM foil. The thickness of the foil increases in the top right corner to the point where the foil is too thick for electron transmission. A regular array of the cubical gamma prime with size ranging from one to three microns is visible at the edge of the TEM foil. The dislocations are concentrated primarily in the gamma matrix, although some dislocations appear in the gamma prime. No substructure or cell formation is visible in the shot-peened region, implying that dislocation glide and not dislocation climb is the primary deformation mechanism.

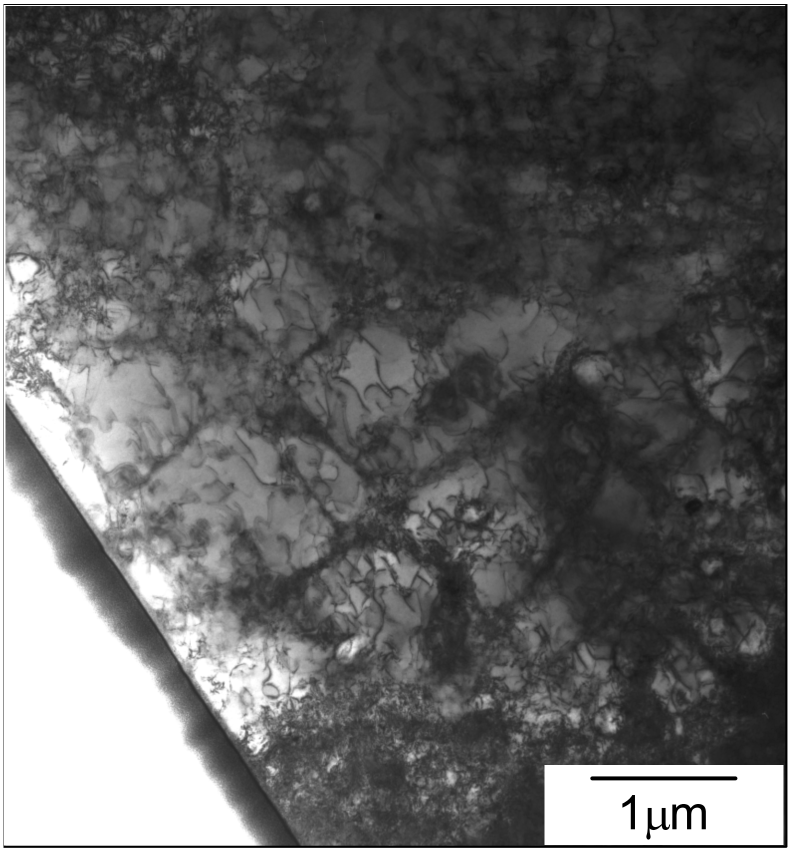

Figure 2. TEM image of shot peened IN100 microstructure.

Baseline Material Characterization

A cylindrical dogbone specimen geometry has been used for room and elevated temperature tensile, creep and cyclic tests on baseline material. The specimen geometry shown in Figure 3 follows ASTM guidelines for specimen dimensioning [92-94]. Limited availability of source material and size of the parent forging prohibits making the complete sample from IN100. The samples have been fabricated by inertia welding a 40 mm long IN100 cylinder between two IN718 cylinders. The length of the IN100 cylinder has been chosen such that the weld would be outside of the reduced section, prohibiting possible weld failures and may influence on extensometry measurements. The samples have been machined to the final dimensions shown in Figure 3. The final machining step is an eight microinch low stress grind (LSG) finish in the longitudinal direction to minimize machining residual stresses and reduce surface roughness that may promote fatigue crack initiation.

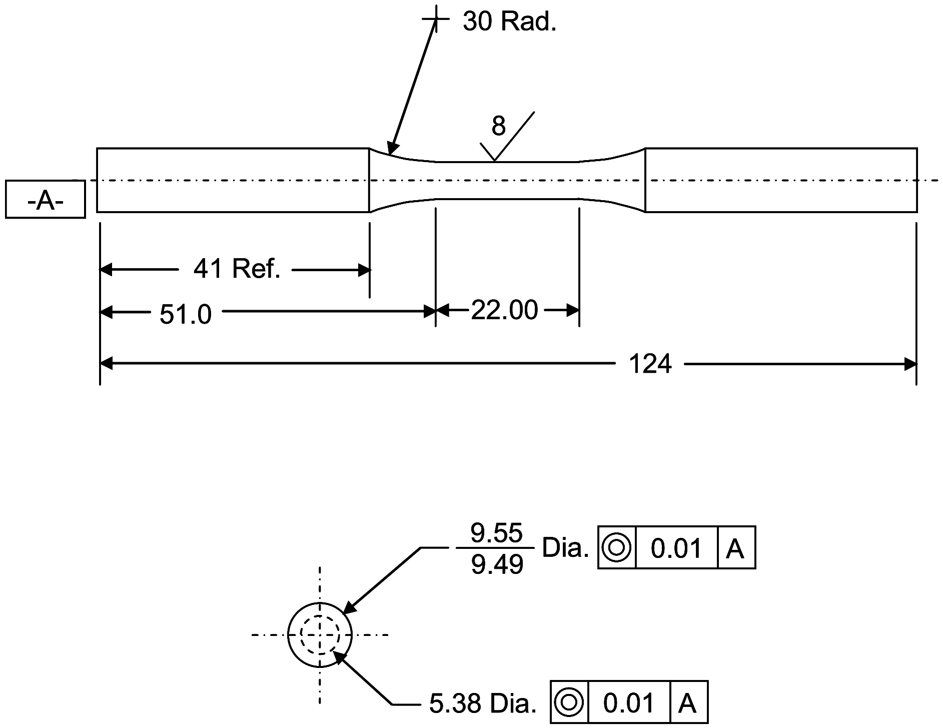

Figure 3. Drawing of Cylindrical Dogbone Specimen Geometry.

All baseline characterization of tensile, creep and cyclic properties have been performed on a standard servo-hydraulic test system. Figure 4 is a photograph highlighting the region around the test specimen shown in the center of the image. Force is applied to the specimen via water-cooled hydraulic grips shown above and below the sample. The heating system consists of two sets of four quartz lamps to provide temperature control along the length of the sample. Four thermocouples on the sample provide feedback for temperature control. Two extensometers on opposite sides of the sample provide average displacement response and indication of misalignment.

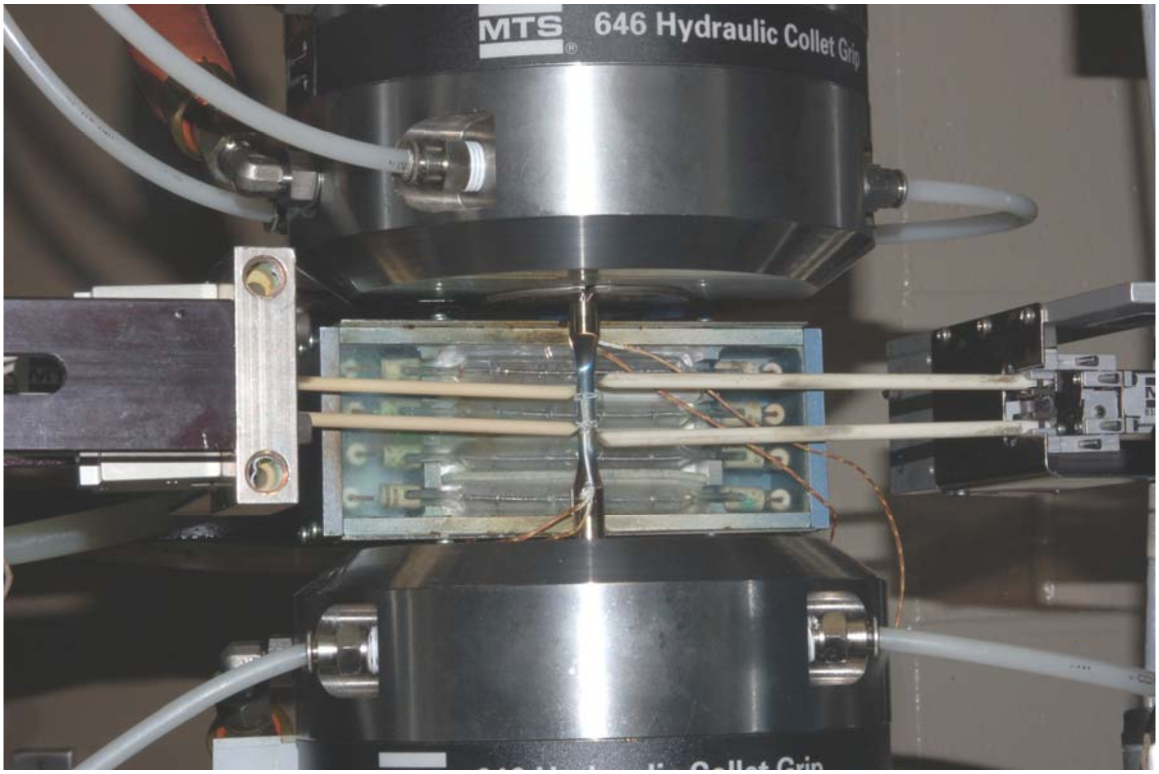

Figure 4. Servo-Hydraulic Test Machine used for Baseline Mechanical Testing.

The monotonic true stress – true stain response for IN100 at two temperatures, 23°C and 650°C, is shown in Figure 5. Extensometry measurements are made on both sides of the test specimen to verify that specimen bending, and hence stress gradients, induced in the gage section were negligible. Tensile, creep and fatigue tests are started only if the room temperature and elevated temperature modulus values agreed with expected results and the modulus values from the two opposing extensometers are in agreement with each other, indicating no bending in the gage section.

During the course of each test a low-stress (≈ 400MPa) elastic loading cycle are performed at room temperature and at elevated temperature. Fine ranges on the load cell and extensometer are used to accurately measure the elastic modulus during the elastic loading cycles. The elastic loadings are performed multiple times to determine the repeatability of modulus measurements. Creep specimens with plastic prestrain are measured before and after prestrain loading. All tensile tests are performed in displacement control with the control signal generated by a 16-bit D/A converter. The displacement rate in the elastic region ($< \sigma_y$) has been selected such that the strain rate was nominally 1.0e-3 m/m/s. A quartz-lamp heating unit with four-zone temperature control is used for all elevated temperature tests. Four K-type thermocouples are used to measure and control the temperature of the test specimen. Four-zone temperature control provides the capability to minimize the temperature gradients through the specimen thickness and along the loading axis of the specimen. Thermal profile maps on the specimen show that the specimen is uniformly heated over the entire gage section of the specimen. Applied load, temperature, displacement and extensometry data are collected during the tensile tests. All tests are conducted in laboratory air using a computer controlled servo-hydraulic test system [88]. Although the elastic modulus and ultimate tensile strength are dependent on temperature the 0.2 percent yield strength and strain to failure are similar for 23°C and 650°C as shown in Figure 5.

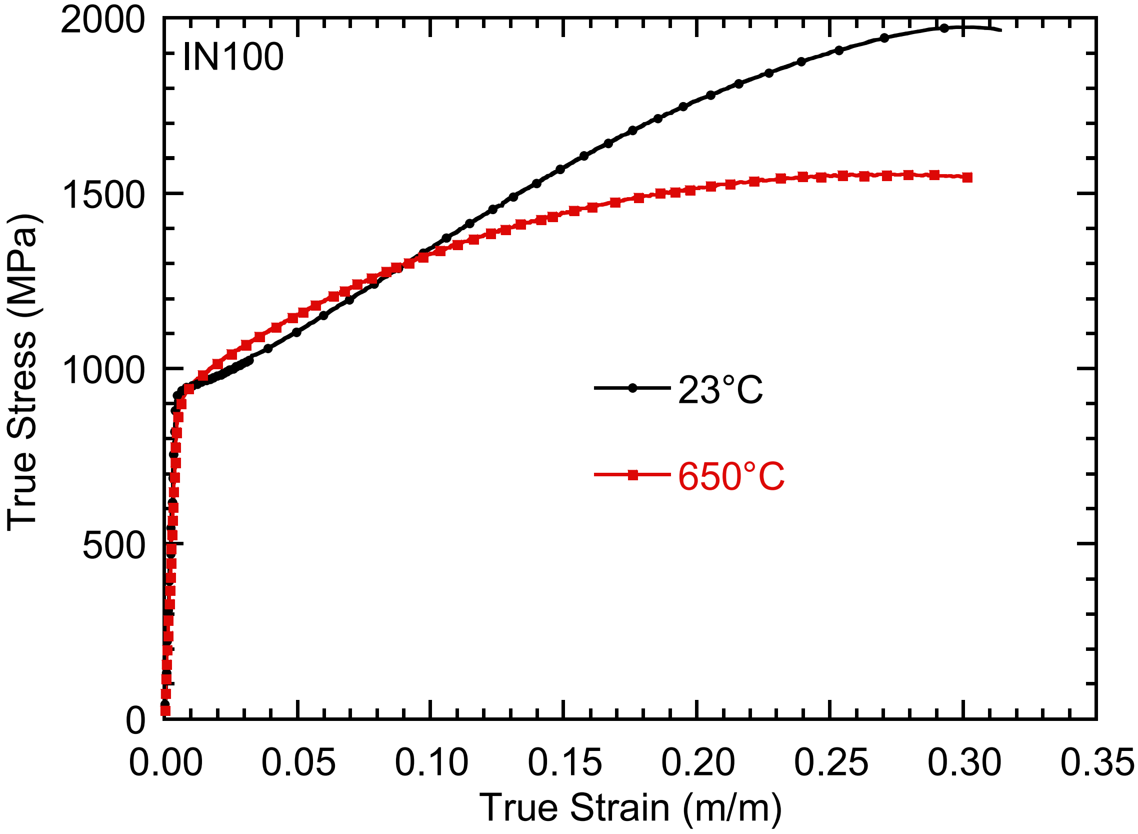

Figure 5. Monotonic True Stress-True Strain for IN100 at 23 and 650°C.

Several empirical equations have been evaluated as candidates to fit the tensile data including those attributed to Ludwik [118] and Ramberg-Osgood [119]. The function that best fits the tensile data is the Ramberg-Osgood model,

$$\varepsilon = \frac{\sigma}{E} + \left(\frac{\langle \sigma - \sigma_o \rangle}{K} \right)^{\frac{1}{n}} \qquad [6]$$

where

ε = total strain,

σ = applied stress,

σ_o = yield strength,

E = elastic modulus,

K = strain hardening coefficient,

n = strain hardening exponent.

The unknown parameters in the above equation are E, K, σ_o, and n. These parameters are determined by performing a least squares fit on the tensile data shown in Figure 5. Least squares analysis is intended to determine the best fit parameters to the model equation. Typically all parameters are determined simultaneously to achieve the best fit. Holding some parameters constant and allowing others to be fit is often discouraged in the literature since it may not determine the best set of parameters to minimize the squares of the residuals. Equation 6 has two distinct regions: an elastic region that is defined by the first term only; and an elastic-plastic region with contributions from both terms of the equation. The least squares fits are completed in two steps. The first step determines the elastic modulus by fitting a straight line to the 400 MPa checkout data. The checkout data has finer resolution and more points than the elastic portion of the tensile data and therefore is a better set of data to determine the elastic modulus. Figure 6 shows the true stress-true strain data points, least squares fit, and 95 percent confidence limits on the predicted elastic strain for IN100 at 23°C. The least squares analysis to determine the modulus has been completed using two different methods. The first approach uses Microsoft® Excel's [107] built-in regression analysis to determine the elastic modulus and associated 95% confidence limits. The second approach uses two IMSL [106] routines, RNLIN and RCOVB, to perform the regression analysis and determine the confidence limits, respectively. The 95 percent confidence limits on the predicted strain are computed following the prediction analysis method detailed in Wolberg [110]. The prediction analysis calculations are implemented in Microsoft® Excel and have been verified using data and analysis from Neter et al., [111].

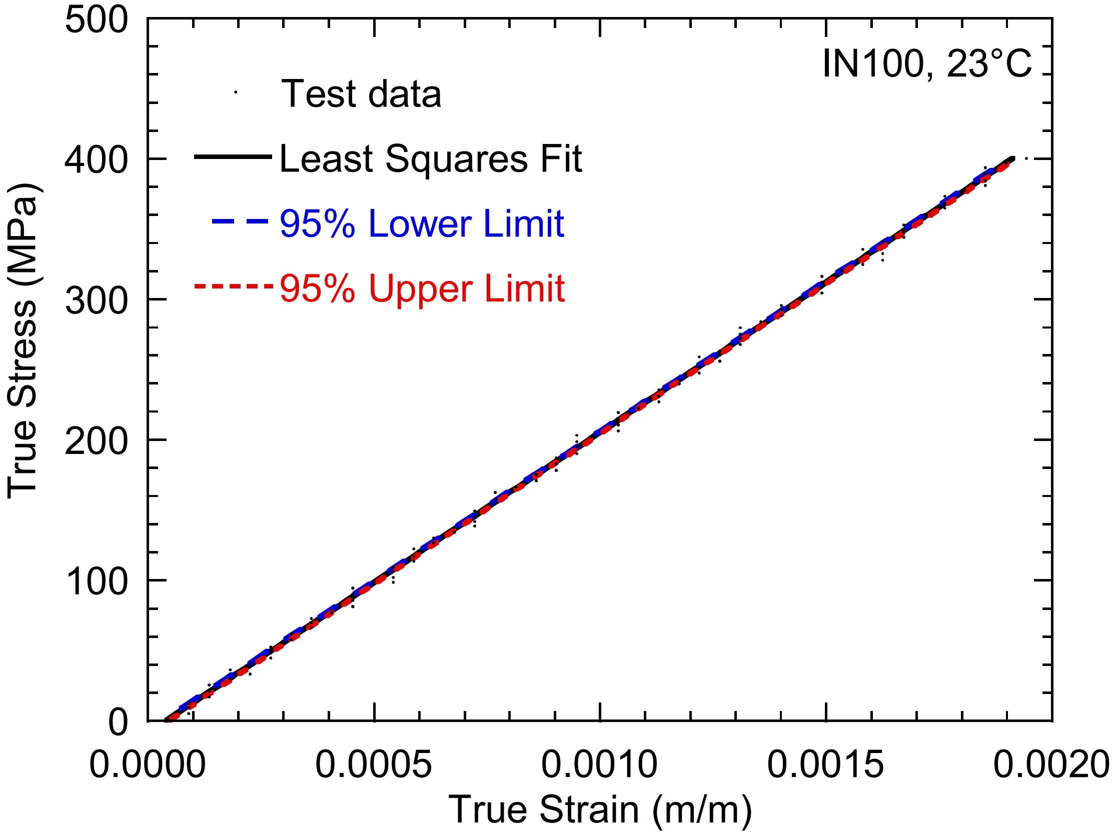

Figure 6. Elastic Modulus of True Stress-True Strain for IN100 at 23°C.

Determination of the parameters for the plastic strain component follows a procedure similar to that described above for the elastic component, with the exception that the elastic modulus is held constant during the fit. Figure 7 shows the true stress-true plastic strain data points, least squares fit, and 95 percent confidence limits on the predicted plastic strain for IN100 at 23°C. The parameters for the complete true stress-true strain curve fit to Equation 6 at 23°C are summarized in Table 2. The table includes the least squares fit value, upper and lower 95 percent confidence limits, and percent uncertainty for each parameter. The elastic modulus has the least amount of uncertainty of all the parameters. The plastic parameters have uncertainty that is three to ten times greater than the elastic modulus.

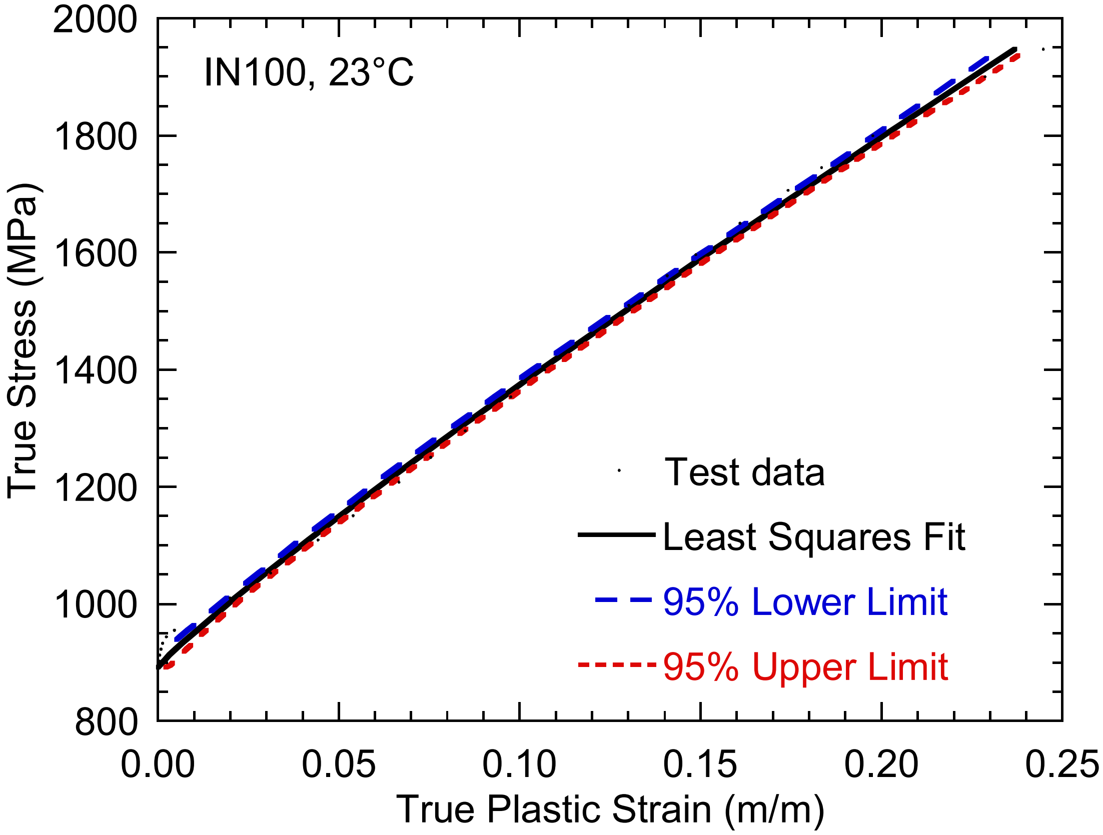

Figure 7. Plastic Region of True Stress-True Plastic Strain for IN100 23°C.

Figure 8 shows the true stress-true strain data points, least squares fit, and 95 percent confidence limits on the predicted elastic strain for IN100 at 650°C. The least squares fits are completed in two steps using the same procedure as for the 23°C data. The linear elastic responses at 23°C and 650°C are very similar and only differ in the value of the elastic modulus.

Table 2. Parameters for Fit to IN100 Tensile Data at 23°C.

Parameter (a)	Least Squares Value	95% Upper Limit	95% Lower Limit	% Uncertainty of Parameter (σ_a / a)
E (MPa)	213,668	215,188	212,148	0.36
σ_o (MPa)	890.9	914.9	866.9	1.30
K (MPa)	3894	4195	3593	3.74
n	0.906	0.963	0.849	3.05

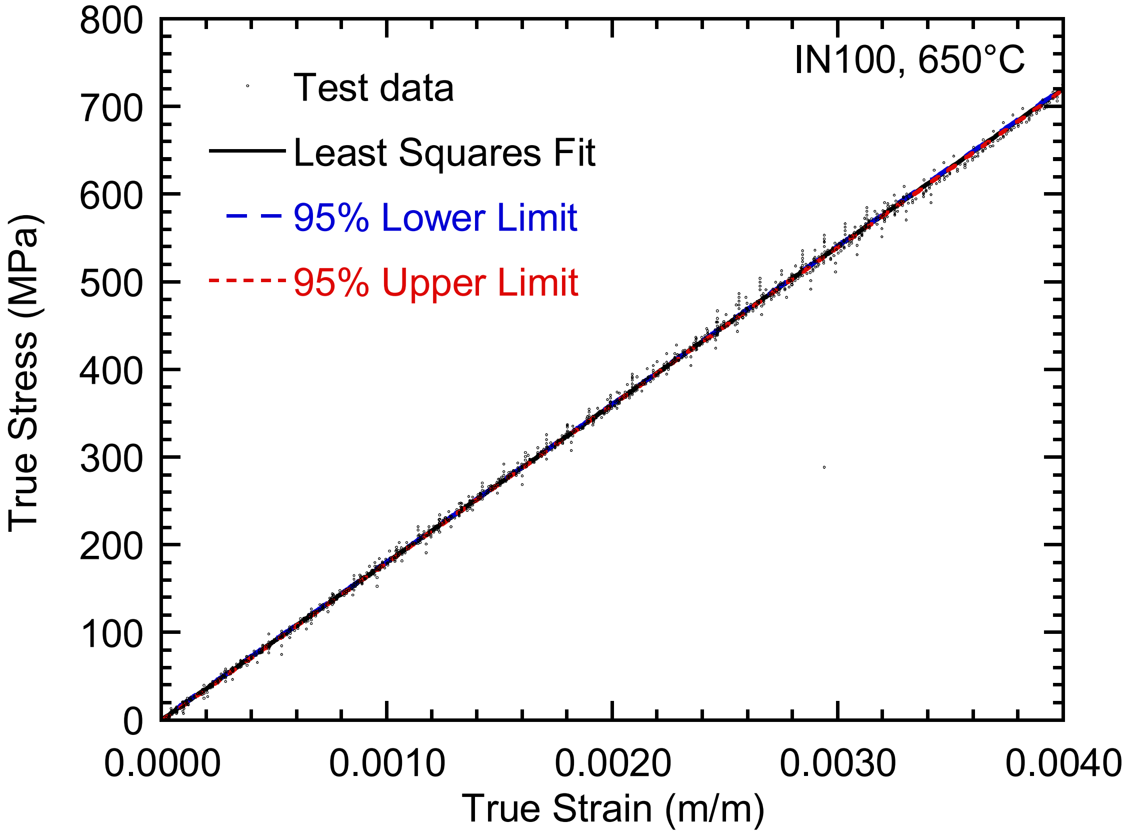

Figure 8. Elastic Modulus of True Stress-True Strain Curves for IN100 650°C.

Figure 9 shows the true stress-true plastic strain data points, least squares fit, and 95 percent confidence limits on the predicted plastic strain for IN100 at 650°C. The parameters for the complete true stress-true strain curve fit to Equation 6 at 650°C are summarized in Table 3.

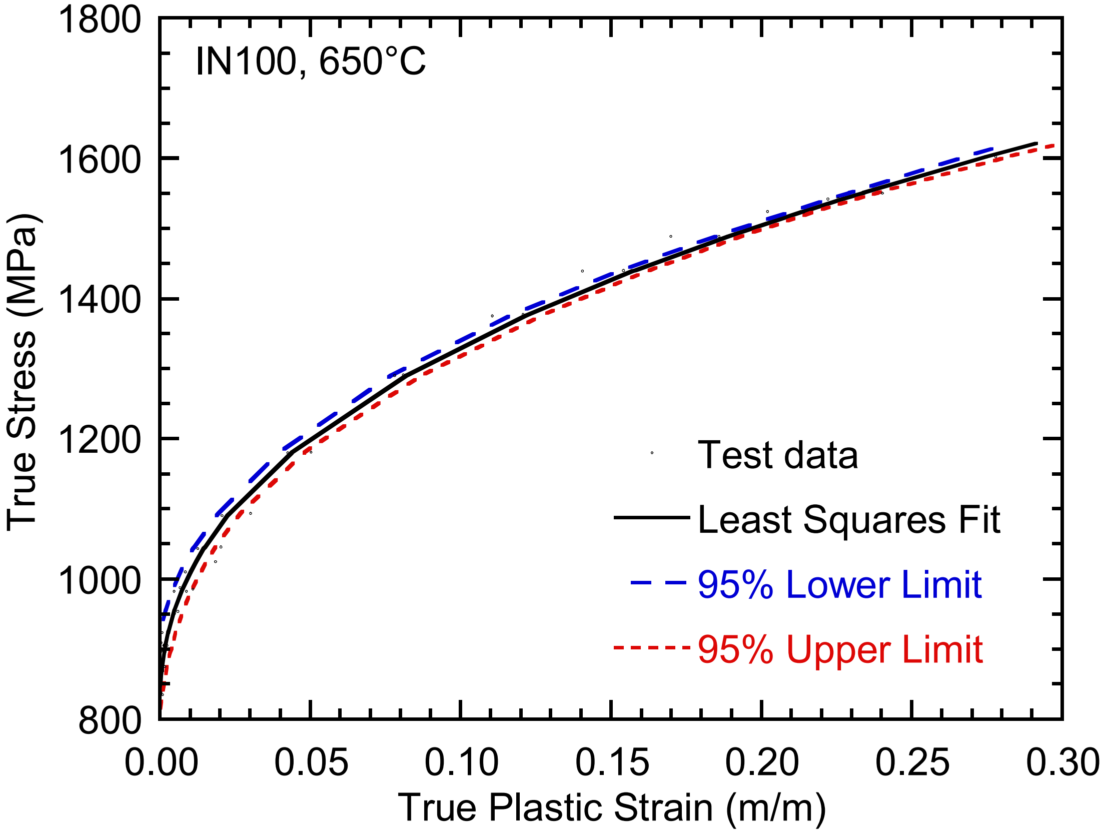

Figure 9. Plastic Region of True Stress-True Plastic Strain Curves for IN100 650°C.

Table 3. Parameters for Fit to IN100 Tensile Data at 650°C.

Parameter (a)	Least Squares Value	95% Upper Limit	95% Lower Limit	% Uncertainty of Parameter (σ_a / a)
E (MPa)	180,002	180,486	179,517	0.14
σ_o (MPa)	799.6	905.6	693.6	6.61
K (MPa)	1355	1418	1292	2.31
n	0.406	0.489	0.323	10.16

Several conclusions can be made by comparing the 23°C and 650°C parameters in Tables 2 and 3, respectively. First, as expected, the elastic modulus (E) decreases, approximately 16 percent, with increasing temperature, and in both cases the elastic modulus has the least amount of uncertainty of all parameters. Similarly, the yield strength (σ_o) also decreases, approximately 10 percent, with increasing temperature. These are relatively small decreases in the parameters and are hardly noticeable in the true stress-true strain plot of Figure 5. However, the strain hardening coefficient (K) and strain hardening exponent (n) exhibit much larger decreases, 65 percent and 55 percent respectively, with increasing temperature. The decrease in the strain hardening coefficient is indicative of an overall decrease in slope of the hardening curve. This may be observed in Figure 5 which shows a decrease in the ultimate tensile strength at 650°C. Finally, the strain hardening exponent controls the nonlinearity of the hardening curve. In Table 2 the value of $n = 0.906$, which is close to unity and therefore the shape of the hardening curve in Figure 6 is nearly linear. In contrast, $n = 0.406$ in Table 3, at 650°C, and the hardening curve in Figure 9 displays a nonlinear shape. Finally, the uncertainty of the strain hardening exponent in Table 3 is much larger than any other value. When the uncertainty of a parameter becomes large this may be an indicator that the chosen function may not fit the data or the parameter itself has little impact on the dependent variable. In this particular case, the chosen function, Equation 6, has more difficulty capturing the nonlinear hardening behavior at 650°C.

Cyclic stress-strain tests have been performed to characterize cyclic hardening behavior and provide necessary data for the coupled creep-plasticity model. All tests follow the ASTM Standard for strain-controlled fatigue testing (E606) [94]. Tests are conducted under strain control, using fully reversed ($R = -1$) loading conditions with a triangular waveform, and at a constant strain rate of 10^{-3} /s. Figure 10 shows the monotonic stress-strain response and three hysteresis loops of a strain-controlled test cycled between strain limits of ±1% at 23°C. This material exhibits cycle-dependent hardening behavior as shown by the increase in stress with increasing cycle count for fixed strain limits. The hysteresis loops stabilize after approximately 50 cycles. The data also exhibit the classic difference between monotonic and cyclic stress-strain response. The monontonic curve has a distinct change between elastic and inelastic regions characterized by an almost bilinear shape, while the cyclic curves display a much smaller linear region and a gradual continuous change in slope in the inelastic region.

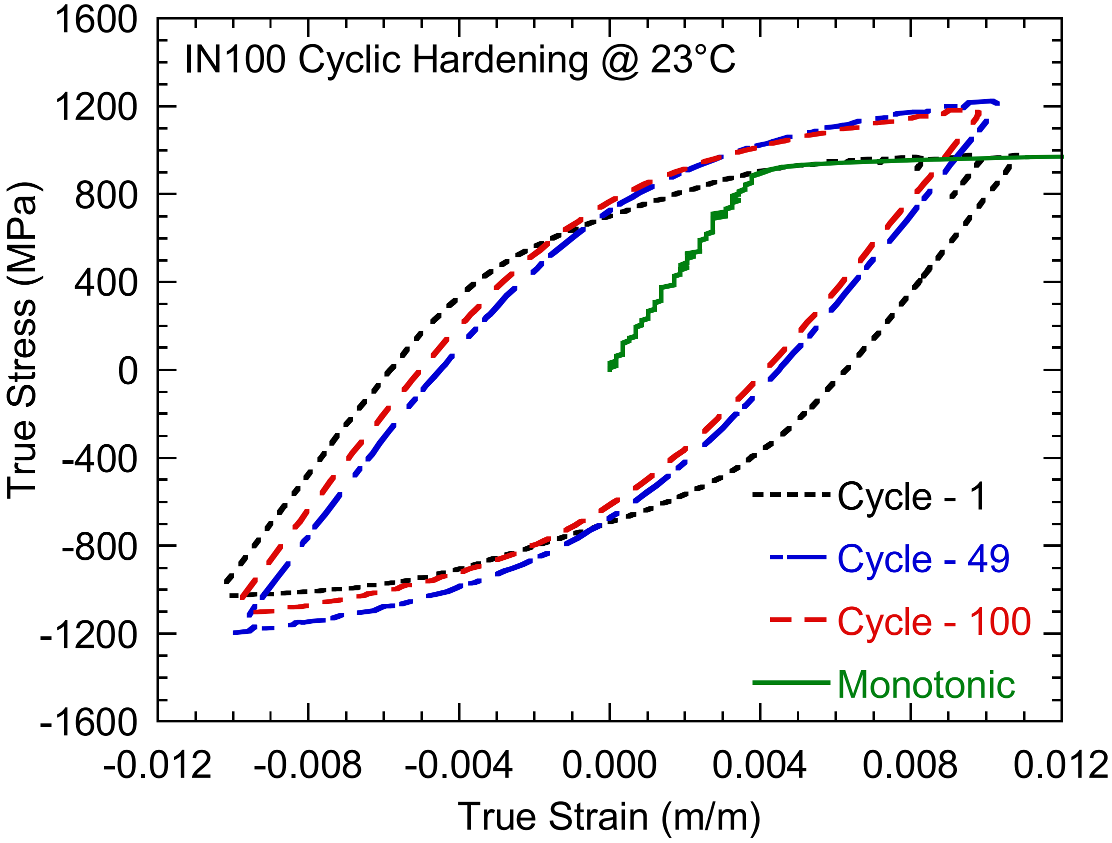

Figure 10. Cyclic True Stress-True Strain Curves for IN100 at 23°C.

Stabilized cyclic stress-strain loops for IN100 under fully reversed (R = -1) loading conditions at 23°C and 650°C are shown in Fig. 11. In contrast to the cycle-dependent hardening observed at 23°C, the 650°C exhibits cyclic-stable behavior on the first cycle. Both are cycled under strain control (±1 percent) with a triangular waveform and at a strain rate of 10^{-3} /s. The loops have nearly identical peak stresses and differ only in the width of the hysteresis loop which results from the difference in modulus between the two temperatures.

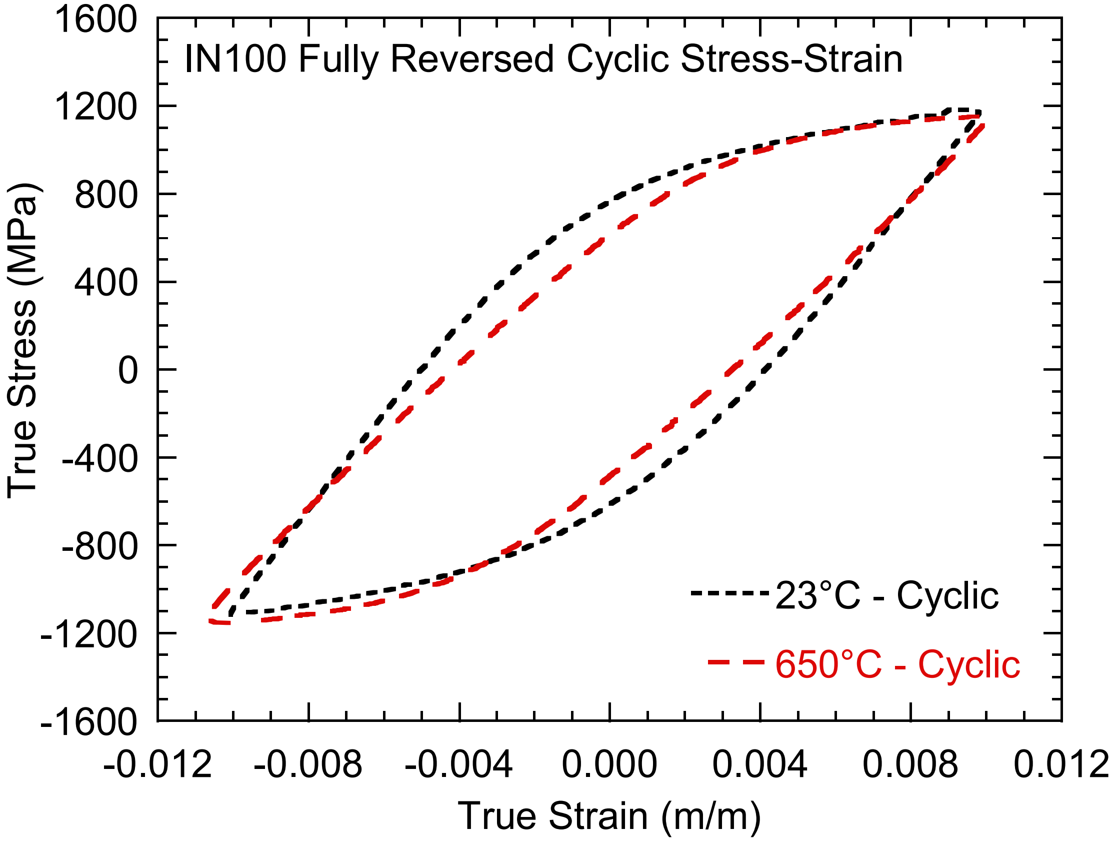

Figure 11. Comparison of Cyclic True Stress-True Strain for IN100 at 23°C and 650°C.

Traditionally creep data for constant temperatures above 0.4 T_m and constant stress conditions are often shown in a plot similar to Figure 12. The abscissa is time, which starts after the sample has reached the target stress. The ordinates on the left and right sides respectively, are total strain and strain rate. The solid black line represents total strain and the dotted blue line strain rate. The plot has three regions identified as primary, secondary, and tertiary. The creep rate in the primary region decreases until a minimum or steady-state strain rate is reached in the secondary region. The secondary region is defined by a constant or minimum creep rate. Finally, the tertiary region is defined by increasing strain rate until failure. What is not shown in this type of plot is the material response prior to reaching the desired creep stress. In most materials the response is elastic, and only the initial loading strain is plotted on the graph as the first point. However, nickel-base superalloys, and specifically IN100, have been developed to resist creep deformation at temperatures of 0.8 T_m, and stresses near and above the yield strength. Under these conditions, plastic yielding during loading will affect the creep rate and deformation response. Furthermore, if the material is subject to prior plastic strain at room temperature, elevated temperature yielding may be mitigated.

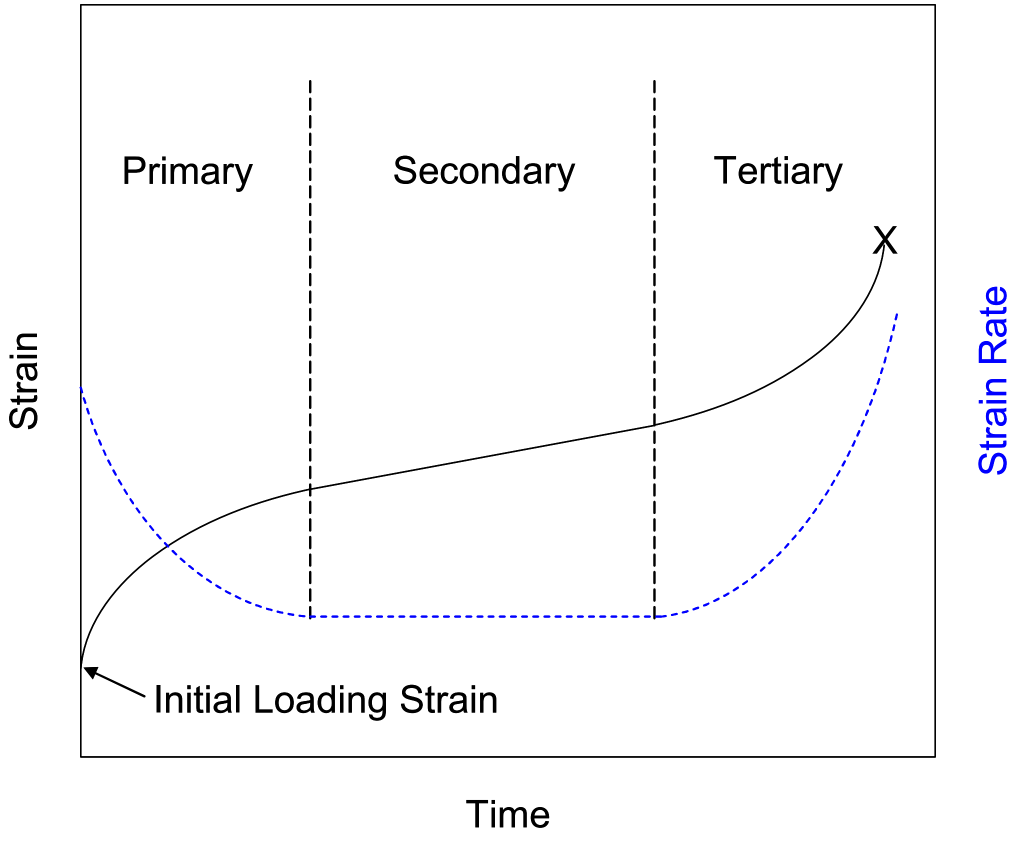

Figure 12. Traditional Creep Strain and Creep Rate versus Time Curves.

Figure 13 is a plot of total strain versus time for three creep tests conducted at stress levels of 800, 900 and 1000 MPa and a temperature of 650°C. Creep tests at 800 and 900 MPa exhibit similar response with less than 0.5 percent accumulated creep strain, whereas the 1000 MPa test involved significantly more deformation, approximately seven percent, and a much shorter rupture time.

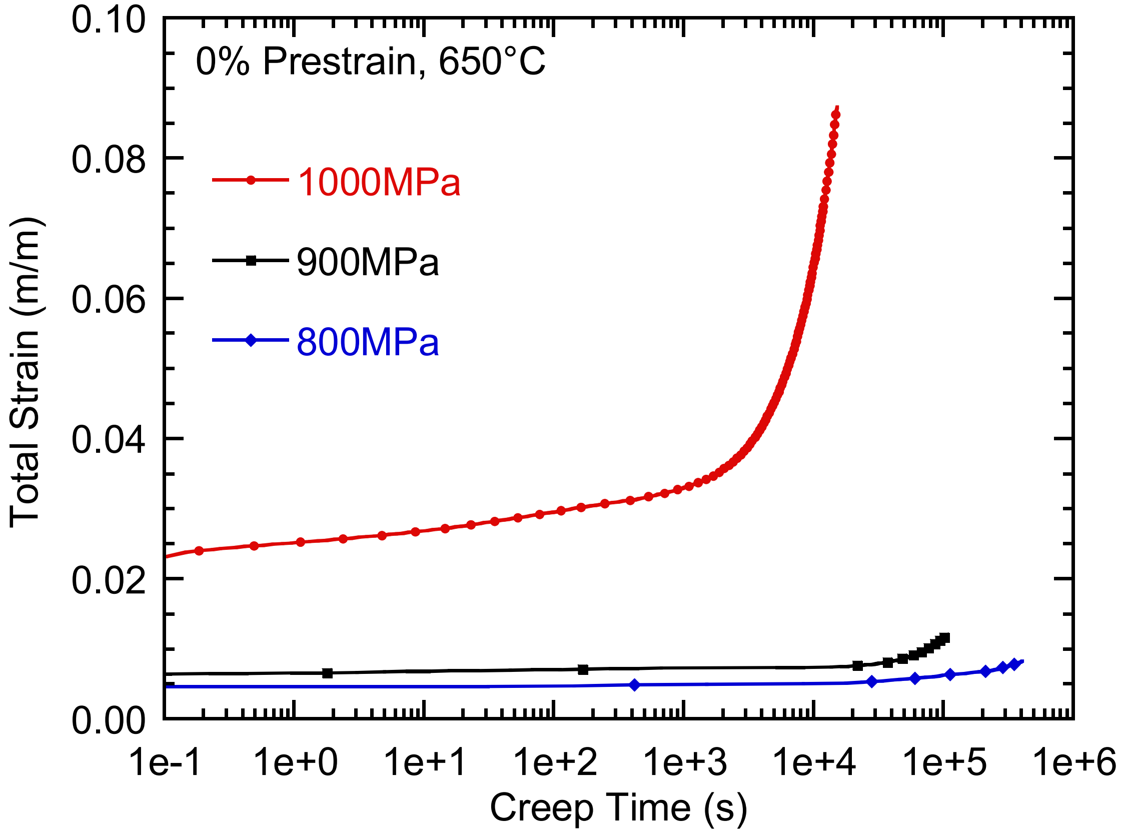

Figure 13. Total Strain versus Time Curves for IN100 at 650°C.

A plot of creep rate versus time with the same test data as in Figure 13 is shown in Figure 14. Both the initial creep rate and minimum creep rate increase with increasing stress level. Furthermore, the time to achieve minimum creep rate decreases with increasing stress level.

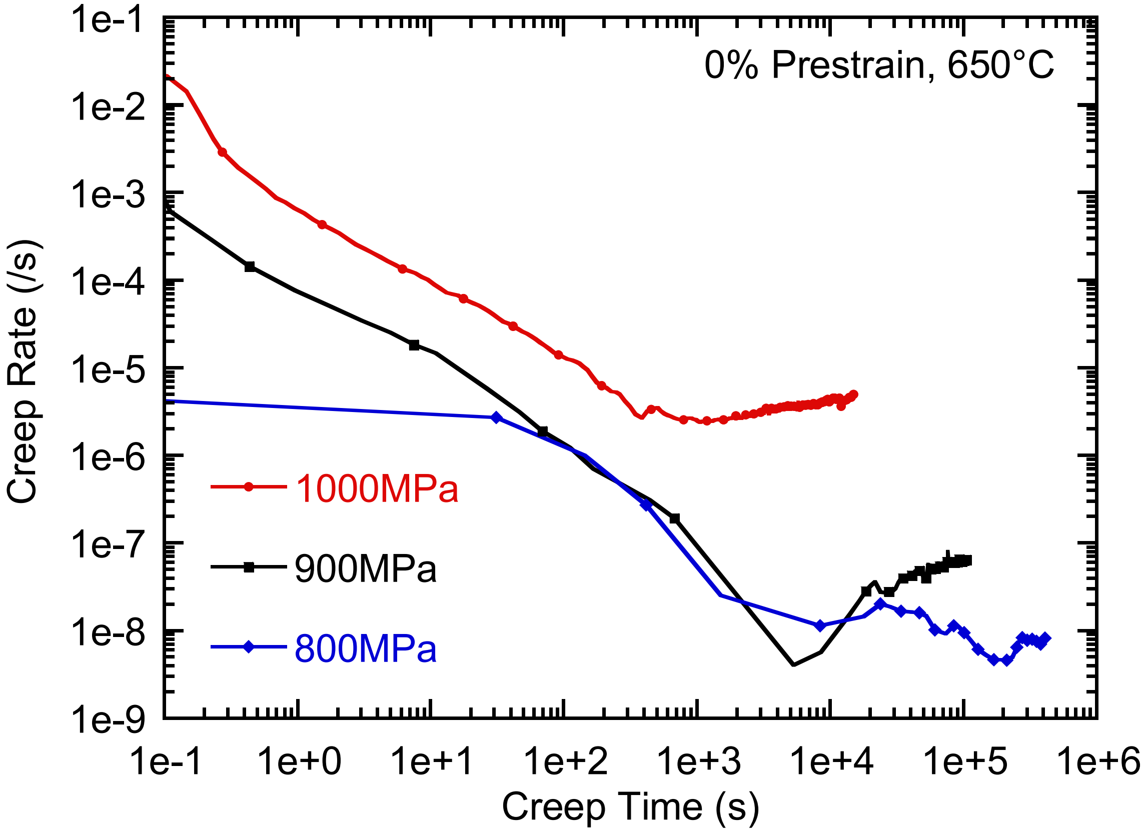

Figure 14. Creep Rate versus Time Curves for IN100 at 650°C.

The initial loading strain shown in Figure 13, and initial creep rate shown in Figure 14 indicate that yielding may occur during loading. Furthermore, the creep model that will be employed in the analysis is based on strain hardening, so a figure that provides total strain on the abscissa will provide more insight into the creep deformation behavior.

A plot of total strain rate versus total strain that includes the initial loading response is shown in Figure 15, using the same data that appear in Figures 13 and 14. All tests have been performed in load control at a loading rate of 175 MPa/s, selected to achieve a strain rate in the elastic regime of 10^{-3} /s. The creep test at 800 MPa exhibits elastic loading to the test stress followed by a dramatic drop of five decades in strain rate with very little accumulated strain beyond initial loading. Both the 900 and 1000 MPa creep tests experience yielding before reaching the target stress as indicated by the increase in strain rate. The change in deformation response is significant even for small plastic strains.

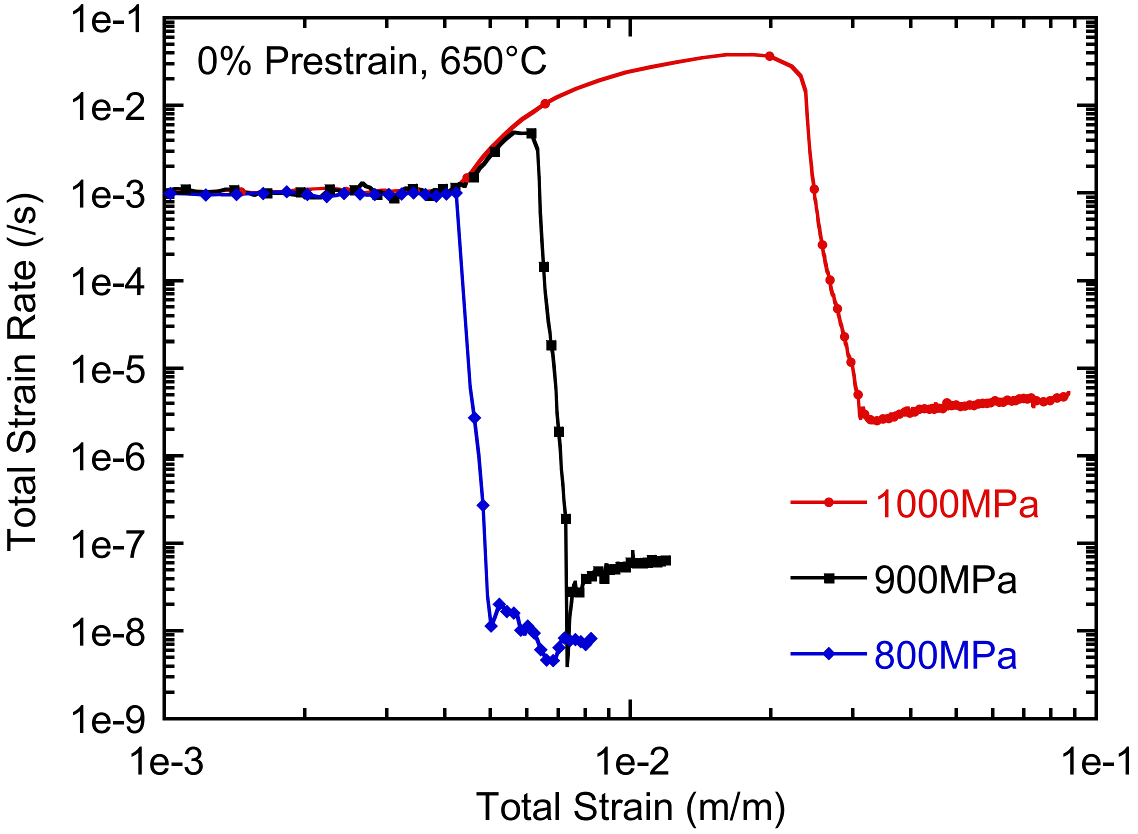

Figure 15. Total Strain Rate versus Total Strain Curves for Virgin IN100 at 650°C.

Table 4 is the test matrix for the baseline creep tests that indicates the range of room temperature plastic prestrain conditions and creep stress levels that are included in this study. Preliminary testing concluded that small plastic prestrains produce the most significant changes in the creep response. Therefore plastic prestrains have been limited to less than five percent. The choice for temperature and stress levels also has been based on preliminary testing, as well as anticipated service conditions in turbine engine applications.

Table 4. Creep Test Matrix for IN100 at 650°C.

σ_{max} (MPa)	Plastic Prestrain (%) @ 23°C			
	-1	**0**	**1**	**5**
1000	X	X	X	X
900	X	X	X	X
800	X	X		X

The effect of room temperature plastic prestrain on creep deformation behavior is shown in Figure 16 for an applied stress of 1000 MPa and temperature of 650°C. The zero percent prestrain case is the baseline that has been discussed in previous plots. The one percent prestrain case exhibits delayed yielding resulting from an increase in the yield surface during prestrain loading. The minus one percent prestrain loading exhibits a lower tensile yield resulting from the Bauschinger effect and supports the need to include a plasticity model with kinematic hardening. Also, the increase in strain rate is more gradual for the compressive prestrain, which is consistent with the more gradual hardening curve described in the previous paragraphs on cyclic hardening. Only for the five percent prestrain test is yielding mitigated upon loading to 1000 MPa. The data also show that any prestrain, tensile or compressive, results in a decrease in the minimum strain rate. The open diamond symbols represent the initial loading strain, and clearly reflect the complex deformation that occurs prior to reaching the target stress for creep.

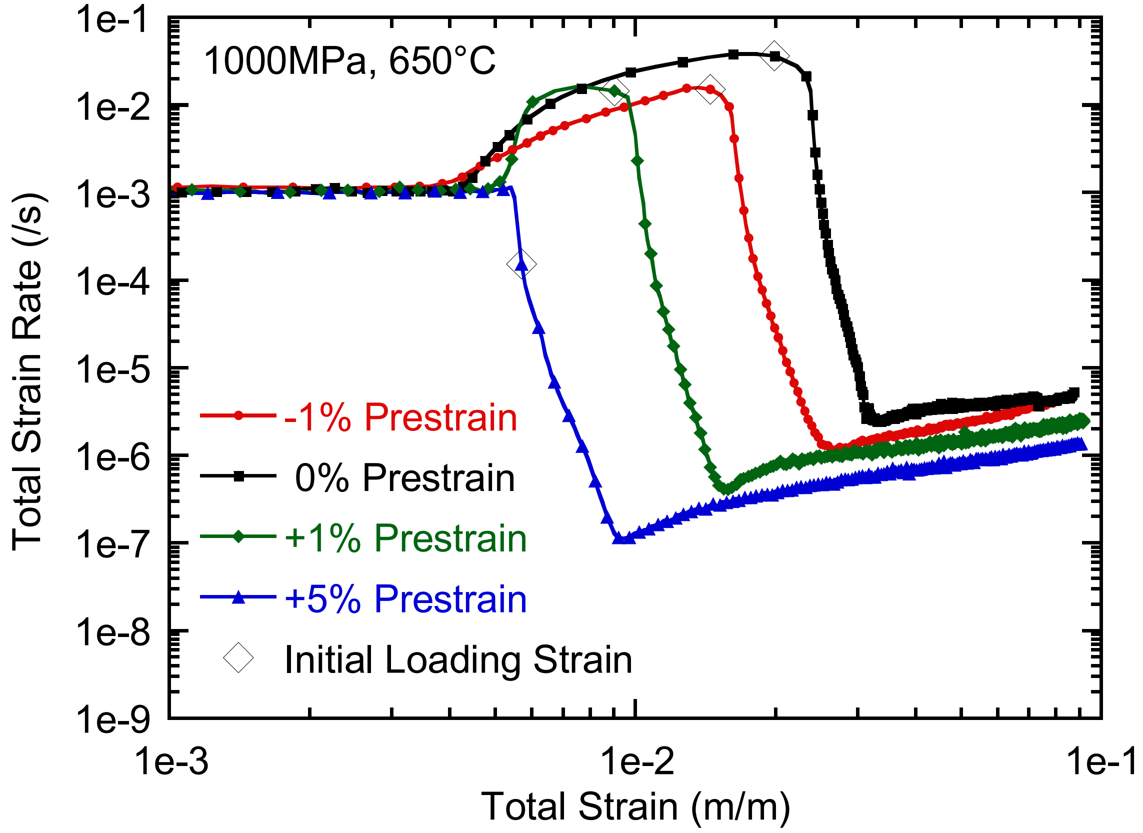

Figure 16. Total Strain Rate versus Total Strain for IN100 at 1000 MPa and 650°C with Different Levels of Prestrain.

A similar plot displaying the effect of room temperature plastic prestrain on creep behavior at 900 MPa is shown in Figure 17. Again, the minus one percent prestrain loading exhibits a lower tensile yield resulting from the Bauschinger effect. Also, the increase in strain rate is more gradual for the compressive prestrain, which is consistent with a more gradual hardening curve that is often seen with reversed yielding. At 900 MPa both the one percent and five percent prestrain tests do not yield before reaching the target stress. In this case the compressive prestrain increases the minimum creep rate. This is contrary to observations made at 1000 MPa where any prestrain, tensile or compressive, lowers the minimum creep rate.

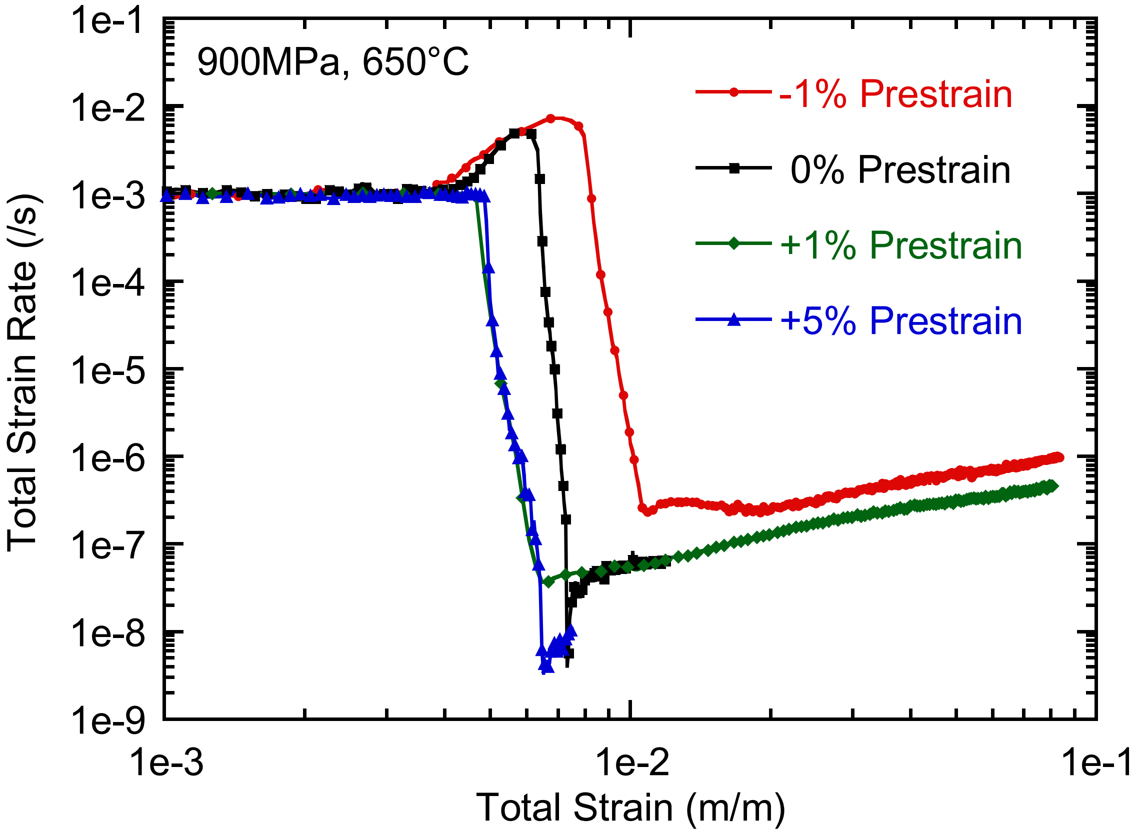

Figure 17. Total Strain Rate versus Total Strain for IN100 at 900 MPa and 650°C with Different Levels of Prestrain.

At 800 MPa the effect of room temperature plastic prestrain on creep behavior is negligible as shown in Figure 18. All tests exhibit a similar minimum creep rate regardless of prestrain level. In this case, only the minus one percent prestrain loading exhibits any yielding during loading since 800 MPa is below the virgin yield strength. The one percent prestrain test has not been completed at this stress level, based on the results of the first three tests. These results also indicate no need to investigate creep response at stress levels below 800 MPa.

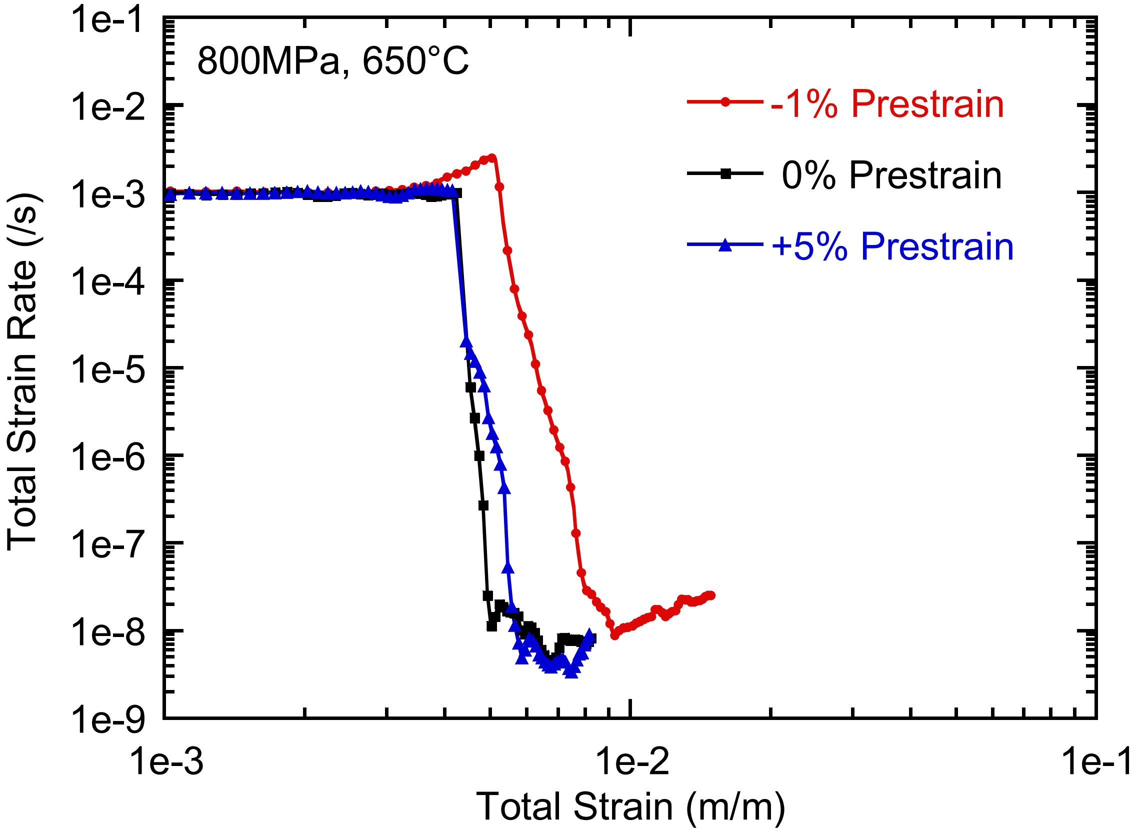

Figure 18. Total Strain Rate versus Total Strain for IN100 at 800 MPa and 650°C with Different Levels of Prestrain.

An additional check on the creep response may be made by plotting the data as a function of stress for a common prestrain loading condition as displayed in Figures 19 through Figure 21. For each level of prestrain the minimum creep rate increases with increasing stress as expected. The minimum or secondary creep rate for all stress and prestrain levels are summarized in Figure 22 as plots of minimum creep rate versus applied stress, and listed in Table 5. Power law fits to the data are shown as dotted lines, to emphasize that a power law model based on stress alone will not capture strain rate response accurately. Prior plastic prestrain must be included in the model for application to residual stress relaxation of shot peened IN100. Analysis of the creep data and model appear later, in the material model development chapter.

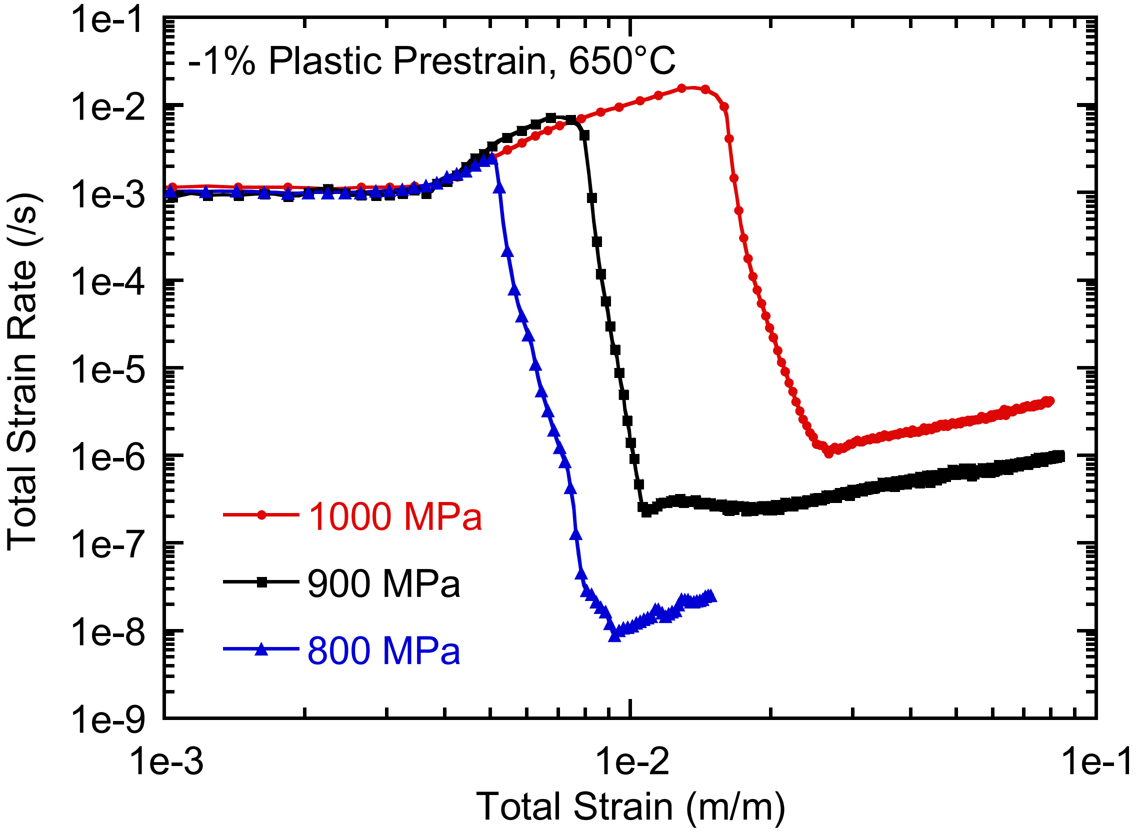

Figure 19. Total Strain Rate versus Total Strain for IN100 at -1% 23°C Plastic Prestrain and 650°C Creep.

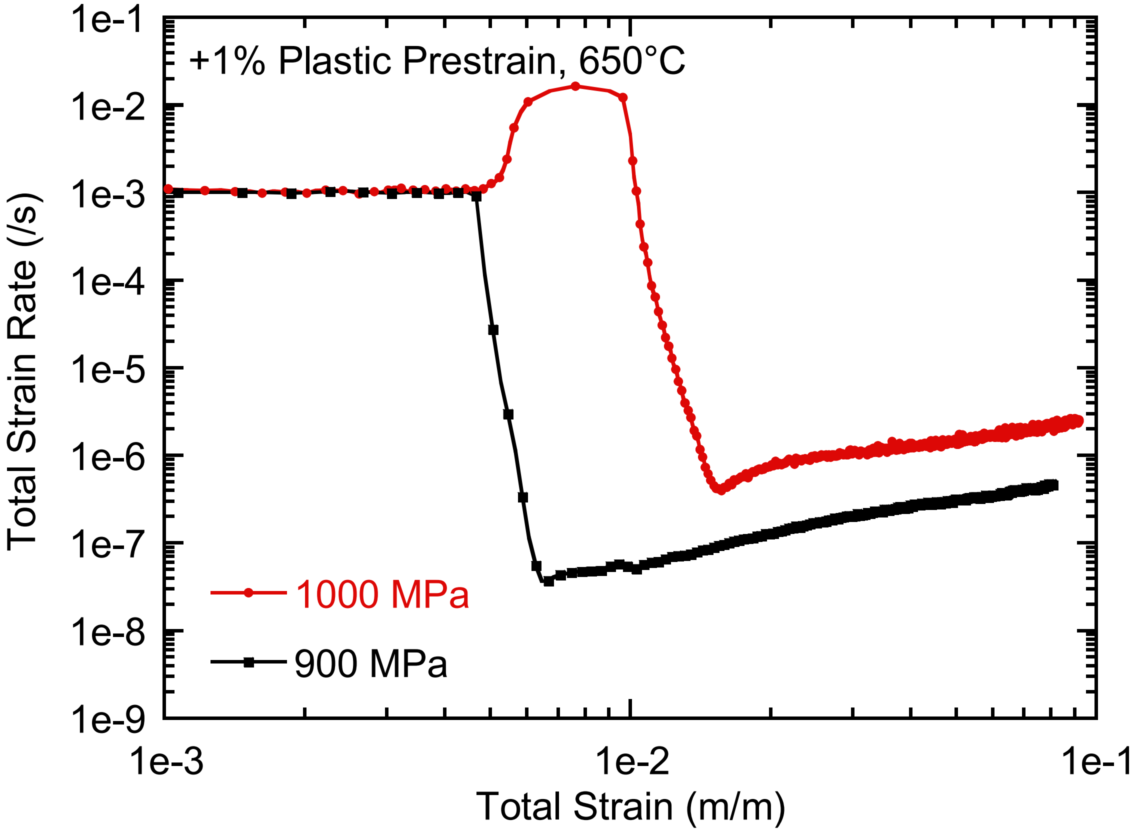

Figure 20. Total Strain Rate versus Total Strain for IN100 at +1% 23°C Plastic Prestrain and 650°C Creep.

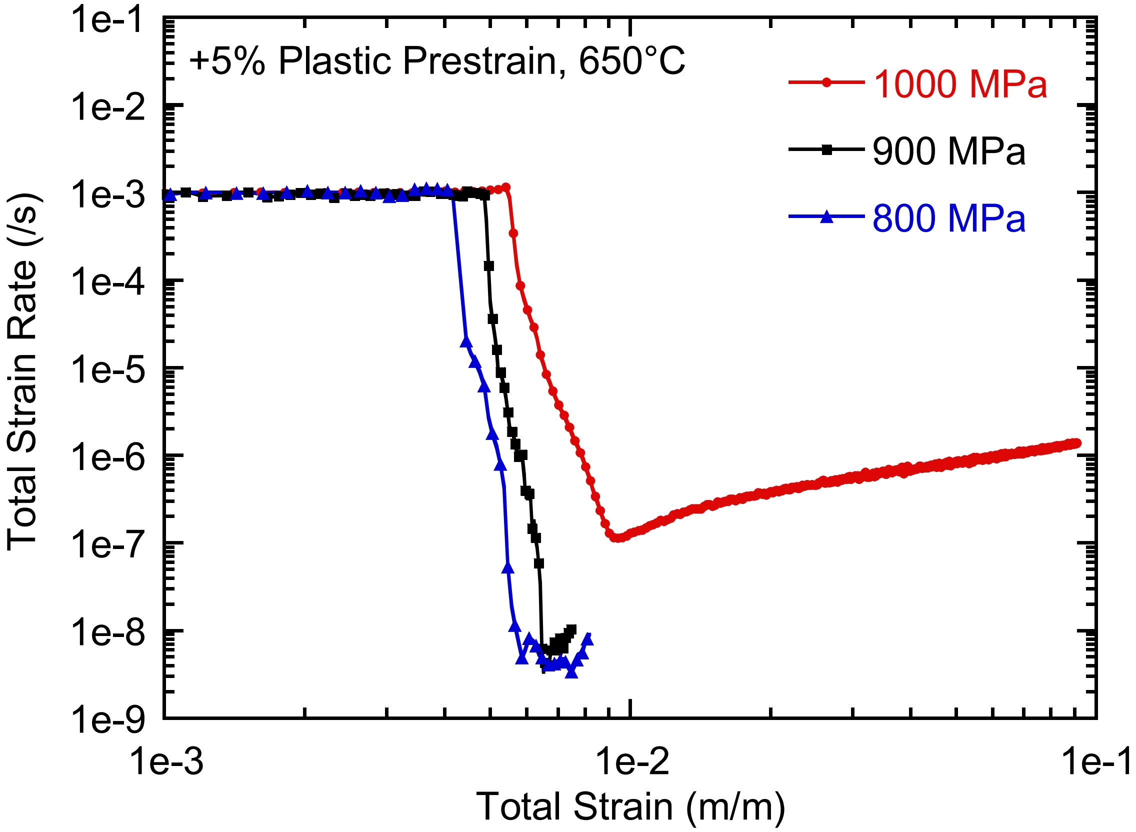

Figure 21. Total Strain Rate versus Total Strain for IN100 at +5% 23°C Plastic Prestrain and 650°C Creep.

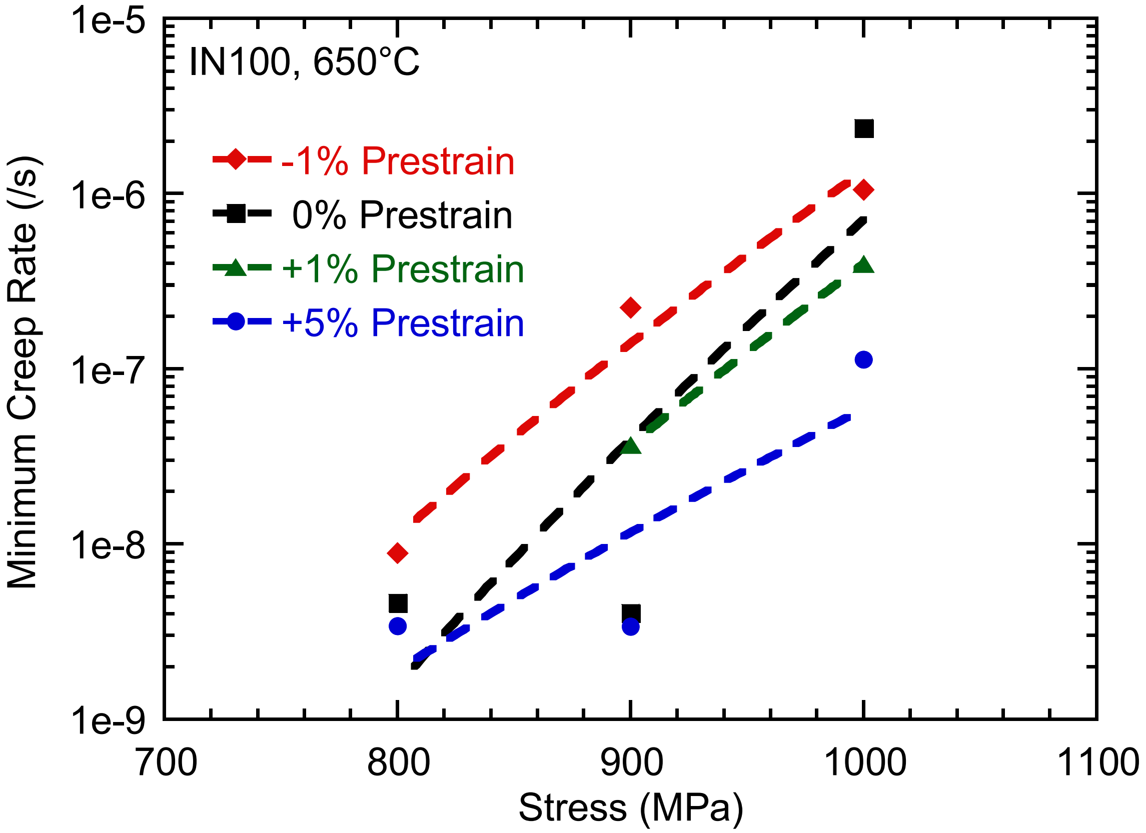

Figure 22. Minimum Creep Rate versus Stress for IN100 at 650°C.

Table 5. Minimum Creep Rates for IN100 at 650°C.

σ_{max} (MPa)	**Plastic Prestrain (%) @ 23°C**			
	-1	**0**	**1**	**5**
1000	1.05E-06	2.37E-06	3.98E-07	1.13E-07
900	2.24E-07	4.03E-09	3.66E-08	3.38E-09
800	8.90E-09	4.60E-09	-	3.40E-09

Residual Stress Specimen Geometry and Shot Peening

This section continues discussion of the material characterization as described in the proceding section, but now includes the effects of localized stress gradients from shot peening, superimposed with the uniform applied loading stress. This starts by measuring the baseline residual stress and cold work (plastic strain) depth profiles in several shot peened samples using x-ray diffraction. A review of previous work on the effects of thermal exposure on residual stress relaxation provides a comparison for relaxation under mechanical loading. Finally, analysis of the deformation behavior of shot-peened specimens, under various loading histories, is analyzed.

Characterization of the initial residual stress and plastic strain depth profiles is necessary for accurate prediction of the evolution of stresses and plastic strains under applied thermal and mechanical loading. The accuracy of stress predictions depends on accuracy of the initial conditions, specifically residual stresses and plastic strains. There are numerous variables that affect the residual stress and plastic strain depth profile. Elastic and inelastic material properties of the material itself have a pronounced effect on the resulting residual stresses and plastic strains. For example, machining and surface finishing processes, such as grinding and polishing, performed prior to shot peening all impart residual stresses into the component. The shot peening process itself has many variables that contribute to the variability of imparted residual stresses, including shot size, hardness, coverage and angle, just to mention a few.

For many standardized mechanical tests such as tensile, creep, and fatigue, specimen geometry is specified in the testing standard to avoid the pitfalls of specimen design [92-94]. No standard test geometry exists for characterizing residual stress depth profiles or relaxation behavior of surface treatment processes. The Almen strip, used as a control when shot peening, only provides a qualitative measure of shot peening intensity. For this study the design of specimen geometry is based on the mechanics of the shot peening process, mechanical testing matrix, x-ray diffraction (XRD) measurement procedure and planned modeling of relaxation behavior.

Identifying the steps involved in specimen machining, shot peening, mechanical testing, XRD and electropolishing, and analysis of the experiments is necessary to develop an integrated research plan. After identifying limiting factors such as material availability, size of test matrix, and experimental and analytical requirements, a rectangular cross section, dogbone geometry has been chosen as shown in Figure 23. A large flat shot peened surface is desired to maximize the size of the irradiated region during XRD. A cylindrical geometry of equal cross sectional area would provide a much smaller surface area for XRD measurement, add complexity in measuring stresses on curves surfaces, and make electropolishing and measuring uniform layer removal for depth profiles more difficult. For the flat dogbone geometry an irradiated x-ray region of 3 x 5 mm with nominal grain size of 25 μm provides approximately 24,000 interrogated grains over which to determine an average residual stress. A specimen width of 10 mm in the gage section provides a 3.5 mm border around the uniformly stressed region for residual stresses to decay to zero at the free surface. A specimen thickness of two mm was selected based on guidance from the shot peening vendor and the capacity of the hydraulic grip hardware. The resulting cross section area of 20 mm^2 limits the maximum applied stress to 1250 MPa on a 25 kN hydraulic grip system. Applied stresses of 1100 MPa and above will cause the residual stress profile to flip producing tensile residual stresses on the surface of this specimen. The parent material is a disk-shaped forging with an outer and inner radius difference of approximately 130 mm. This dimension limits the maximum specimen length that may be extracted with a radial orientation. The total length of the dogbone specimen is 125 mm. To accommodate extensometry measurements with a 13 mm gage length extensometer and ensure a uniform applied axial loading stress over the XRD irradiated region requires a 20 mm long uniform gage section [92-94]. Additional considerations for specimen dimensions have been based on the XRD experimental techniques [95-97], stress corrections for electropolishing [89], and test matrix conditions.

Based on residual stress depth profiles on a similar superalloy, IN718 [5,23] and typical shot peening specifications for turbine engine components [2,4], an Almen intensity of 6A has been selected.

XRD measurements are interpreted based on the diffraction of radiation reflected from the surface and to a depth of approximately 10 μm for this material. Since the technique measures an average throughout a volume it is important to have a uniform stress field in the plane of the material. Nonlinear gradients in the plane of the stress field will not be captured and can produce erroneous values of measured residual stress. Using the assumption that the residual stress is equally biaxial and only varies as a function of the depth, corrections for volume averaging can be made for electropolishing and for subsequent depth measurements [89].

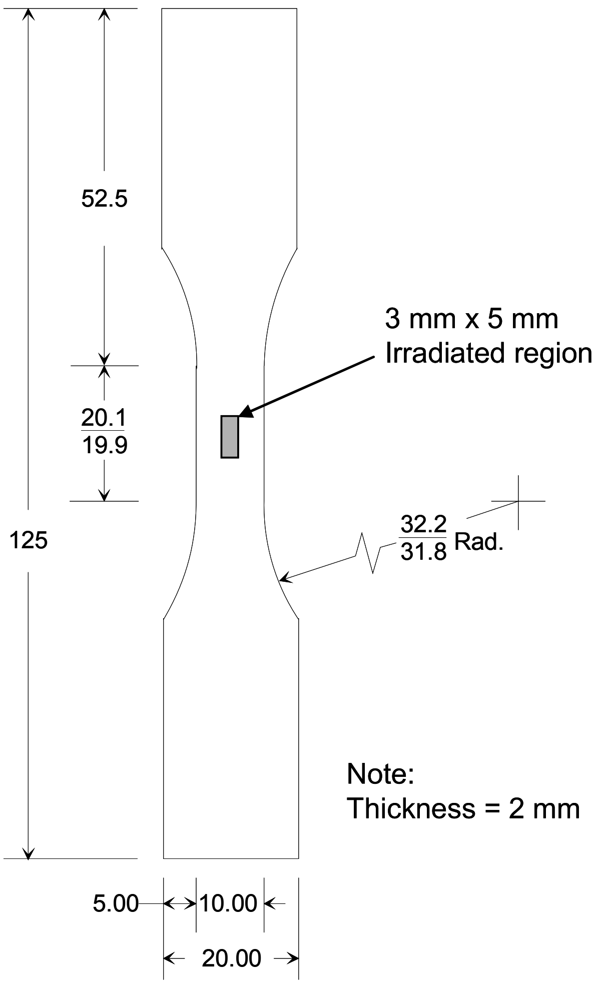

Figure 23. Drawing of Shot Peened IN100 Flat Dogbone Geometry
(All dimensions in mm).

In an effort to minimize variation in shot peening from specimen to specimen, all specimens have been shot peened as a single batch. The dogbone specimens are shot peened to an Almen intensity of 6A-0+2 using a MI-170-R (SAE 170 max. cast steel shot, regular) shot with 125 percent coverage. PEENSCAN® has been applied prior to shot peening to verify complete coverage and uniformity over the entire surface [98].

Obvious changes to the microstructure on all samples near the shot peened surface have been observed. Material deformation, cavities and even embedded shot fragments have been observed on the surface of the samples. Figure 24 is a backscatter SEM micrograph of a polished cross section of IN100. The left side of the image is the shot peened surface of the sample. The left 50 μm area shows a distinct change in microstructure resulting from the shot peening-induced deformation. The right side shows the interior, with a typical representation of the microstructure and individual grains. Superimposed over the microstructure are representative residual stress and percent cold work (plastic strain) depth profiles. All x-ray diffraction measurements have been performed by Lambda Research, Inc. of Cincinnati, OH.

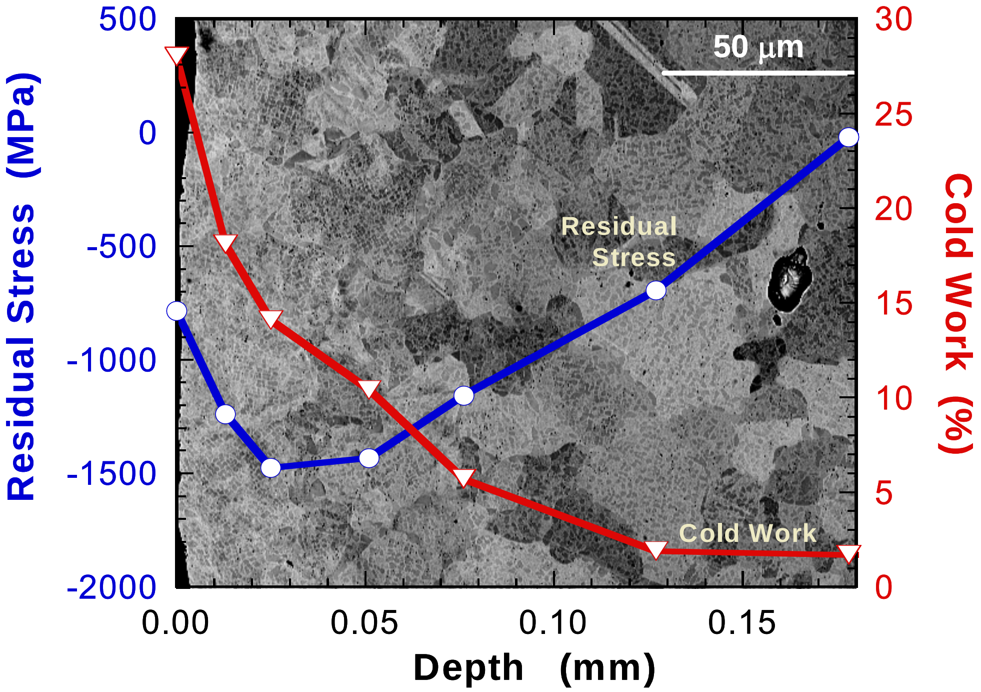

Figure 24. Composite of Baseline Residual Stress and Cold Work Depth Profiles Overlaid on Shot Peened Microstructure.

Relaxation Experiments and Analysis

The x-ray elastic constant E/(1+ν) and the cold work calibration have been experimentally measured on the same batch of material as the test samples for the residual stress relaxation study. The x-ray elastic constant has been measured on the crystallographic direction normal to the (311) plane of the FCC lattice. Determination of the elastic constant has been completed using a thin rectangular beam under four-point bending in accordance with ASTM Test Method for Determining the Effective Elastic Parameter for X-Ray Diffraction Measurements of Residual Stress (E1426) [96].

An empirical equation, based on a relationship developed by Prevéy [16], has been used to relate the peak width at the half height of the diffraction peak to the percent cold work. This empirical relationship has been established by XRD measurements on cylindrical samples deformed in compression to a range of known cold work levels. For this residual stress relaxation study, the cold work has been determined using the width of the (311) diffraction peak at half-height and the empirically measured relationship. X-ray diffraction measurements for residual stress have been completed in accordance with SAE J784a [97] using the diffraction radiation from the (311) planes.

The residual stress and cold work measurements are made at the surface and at nominal depths of 12, 25, 50, 75, 125, 175, 250 and 350 microns. Measurements are made in both the axial loading and transverse directions of the sample at the center of the gage section as shown in Figure 23. Stress corrections for layer removal are completed in accordance with the Moore and Evans [89] elasticity solution for flat plates.

Six baseline residual stress depth profiles with no thermal exposure have been measured on 4 mm thick specimens as part of a thermal relaxation study [25], Figure 25. Five depth profiles have been measured on four different plates (A2, B2, C1, C2) by Lambda Research Inc. and a sixth on plate A2 has been measured elsewhere. The surface residual stresses, compensatory tensile residual stresses and overall response for all six samples are similar. One sample, (01-851, plate C2) exhibits much less subsurface compressive residual stress than the other five. The peak compressive residual stress always occurs within 50 microns of the surface, consistent with the changes in the microstructure as shown in Figure 24.

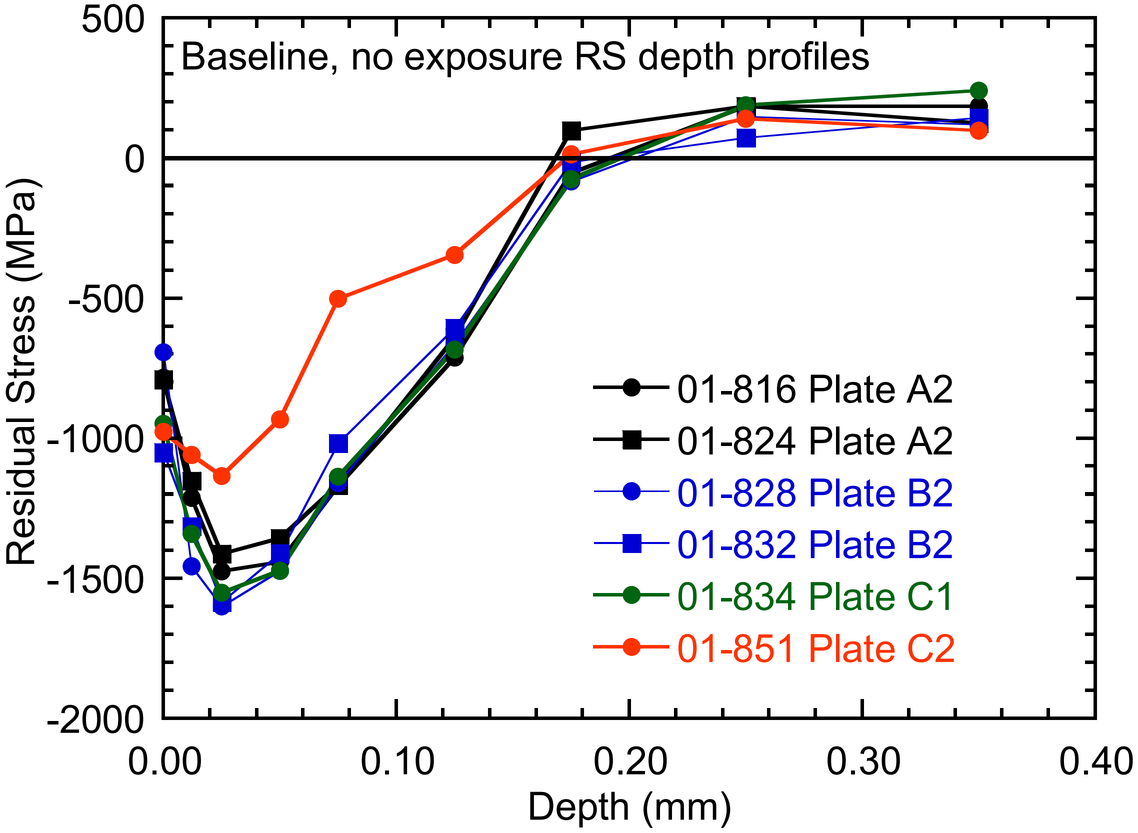

Figure 25. Variability in Baseline Residual Stress Depth Profiles in IN100 for Specimens.

Figure 26 is a statistical analysis of the residual stress depth profiles from Figure 25. The solid circles are the residual stress data points, and the black solid line is a least squares curvefit to the data using

$$\sigma_{RS}(x) = \left[(\sigma_s - \sigma_{\text{int}}) + C_1 x\right]\exp(-C_2 x) + \sigma_{\text{int}} \qquad [7]$$

where (σ_s) is the surface residual stress, (σ_{int}) is the compensatory tensile residual stress and (C_1,C_2) are fitting parameters [108].

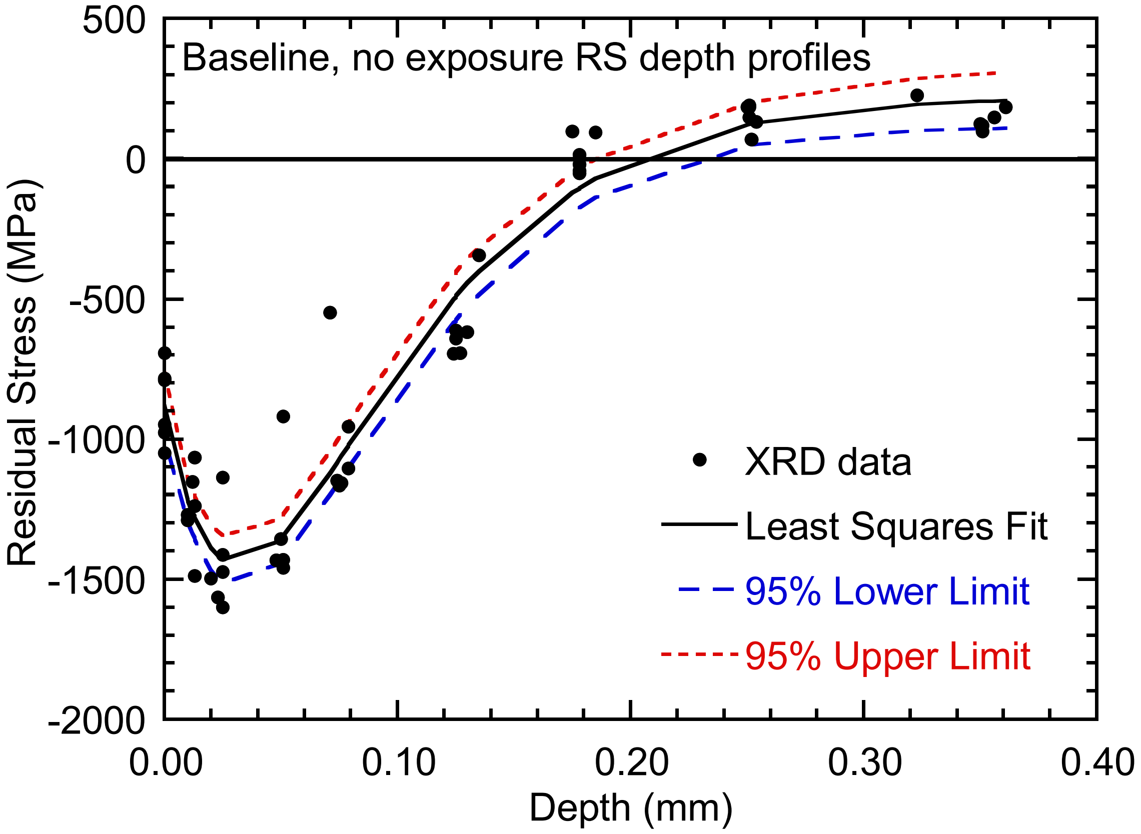

Figure 26. Confidence Limits on Baseline Residual Stress Depth Profiles in IN100.

The dotted lines are the 95 percent upper and lower confidence limits on the residual stress depth profile. Most of the data points from specimen 01-851 fall far outside the confidence limits, and hence it is reasonable to conclude that this particular sample had an incomplete surface treatment as compared to the others. The difference between the upper and lower confidence limits is a maximum at the surface and minimum where the profile changes from compression to tension. This is consistent with results from the literature that report that largest scatter in residual stress depth profiles occur at the free surface. The difference is also large at the end of the depth profile in the tensile region. At this location the difference is approximately equal to the mean value. The least squares fit parameters and corresponding confidence limits are listed in Table 6.

The large value of uncertainty for the compensatory tensile stress parameter, 25.9 percent, indicates it has less of an impact on the shape of the depth profile compared to other parameters. In fact, the uncertainty of the compensatory tensile stress is much larger than the surface residual stress even though the range is greatest at the surface and more of the data points fall outside of the confidence limits at the surface.

Table 6. Parameters for Fit of Residual Stress Depth Profile for IN100.

Parameter (a)	Least Squares Value	95% Upper Limit	95% Lower Limit	% Uncertainty of Parameter (σ_a / a)
σ_s	-879.0	-759.4	-998.5	6.77
σ_{int}	205.7	312.6	98.8	25.9
C_1	-67028	-54523	-79532	9.29
C_2	20.89	23.50	18.27	6.23

Thermal residual stress relaxation data in the literature [12-14,16,25] have shown both temperature and exposure time have a significant effect on relaxation of residual stresses and cold work (plastic strain). The stress relaxation rates are also a function of material properties, dominant deformation mechanism and initial conditions of residual stress and cold work depth profiles. A previous study [25] characterized thermal relaxation of IN100 using a parallelepiped geometry shown in Figure 27. The test matrix covers a large range of temperatures and exposure times, listed in Table 7. The X's in the table correspond to the number of tests completed at that specific set of conditions. Exposure times and temperatures have been selected on the basis of similar studies in the literature [14,16], and expected turbine engine operating conditions for this alloy. Another consideration for selecting these temperatures is based on their homologous temperatures. For temperatures 427, 538, 650, and 704°C the homologous temperatures (T_h) are 0.44, 0.51, 0.58, and 0.61, respectively. These temperatures span the homologous temperature (T_h = 0.5) that is typically associated with active creep deformation while still below the (T_h = 0.8) value that is often considered an upper limit usage temperature for nickel-base superalloys.

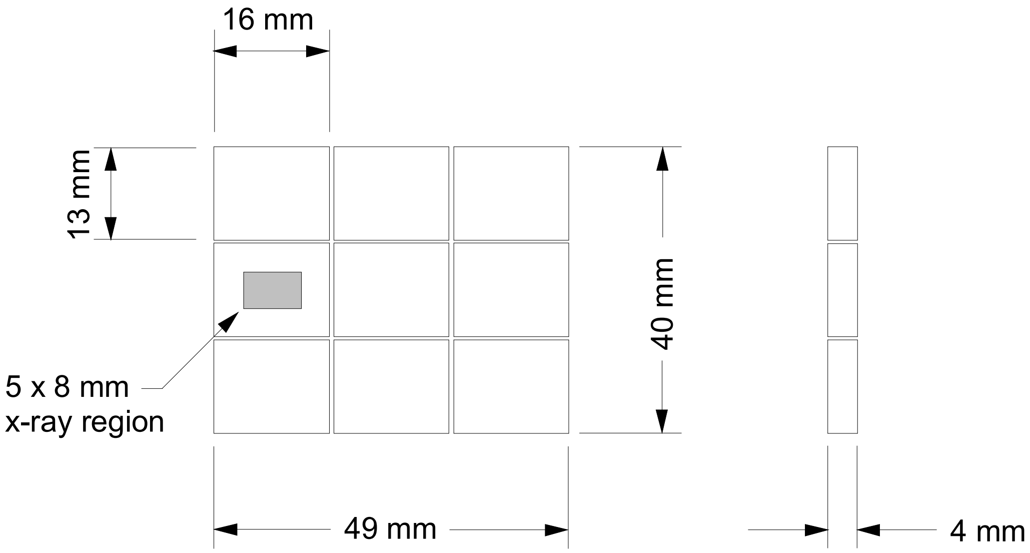

Figure 27. Schematic of Geometry and Cutout Plan for Shot Peened IN100 Thermal Relaxation Specimens and XRD Analysis.

Table 7. Thermal Relaxation Test Matrix for IN100.

Plate #	B2	C1	C1	C2	A2
	Temperature				
Exposure Time (hours)	800°F	1000°F	1200°F	1200°F	1300°F
	427°C	538°C	650°C	650°C	704°C
0.0	x, x	x		x	x, x
0.5	x	x	x	x	x
1.0	x	x	x		x
3.0					x
10.0	x	x	x	x	x
100.0	x			x	x
300.0	x	x	x	x	x

The residual stress and cold work depth profiles from plate C1 (Table 7), thermally exposed to 650°C for up to 300 hours, are shown in Figures 28 and 29, respectively. A compressive surface residual stress of 250-400 MPa remains at the surface for all exposures. Stress relaxation is greatest at the free surface. The stress relaxation is less for the peak compressive stress. However, after 300 hours of exposure to 650°C, residual stress retention is approximately 65 percent. There is also a shift of the peak compressive stress from 25 μm to approximately 75 μm. Below the free surface the residual stress profile does not follow the expected relaxation trend with increased exposure time. In particular at a depth of 50 to 130 μm the 300 hour exposure has a larger compressive residual stress than the 10 hour exposure. In contrast, there is a clear trend of decreasing cold work with increasing exposure time, as shown in Figure 29. The cold work profiles show a large change at the surface, and to a depth of approximately 175 μm, with increased exposure. This depth is coincident with the location where the stresses are below the monotonic yield strength of the material.

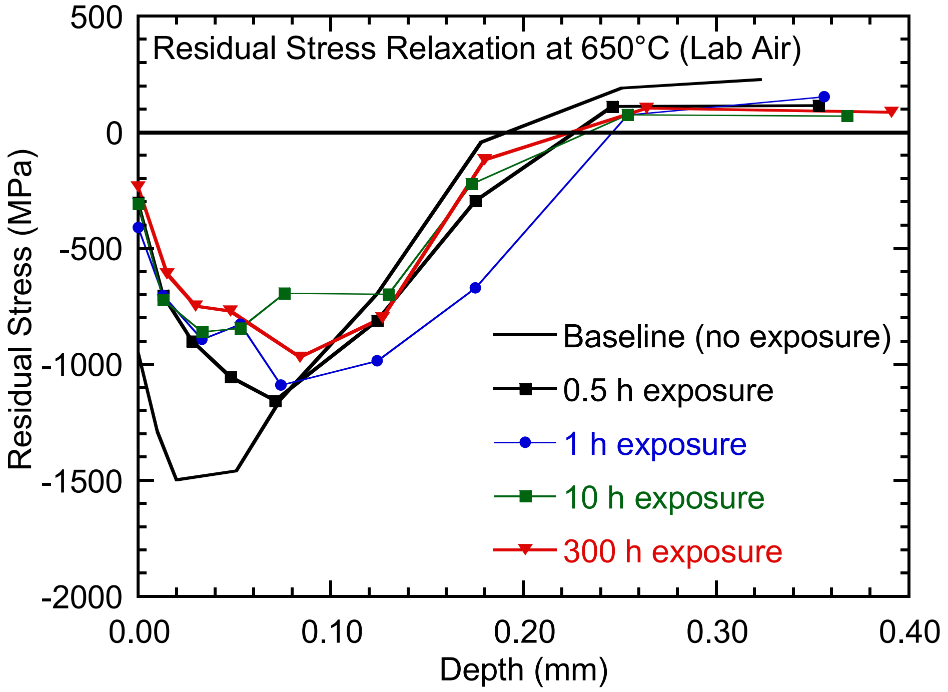

Figure 28. Thermal Relaxation of Shot Peened Residual Stress Depth Profile in IN100 at 650°C Taken from Plate C1 as Shown in Table 7.

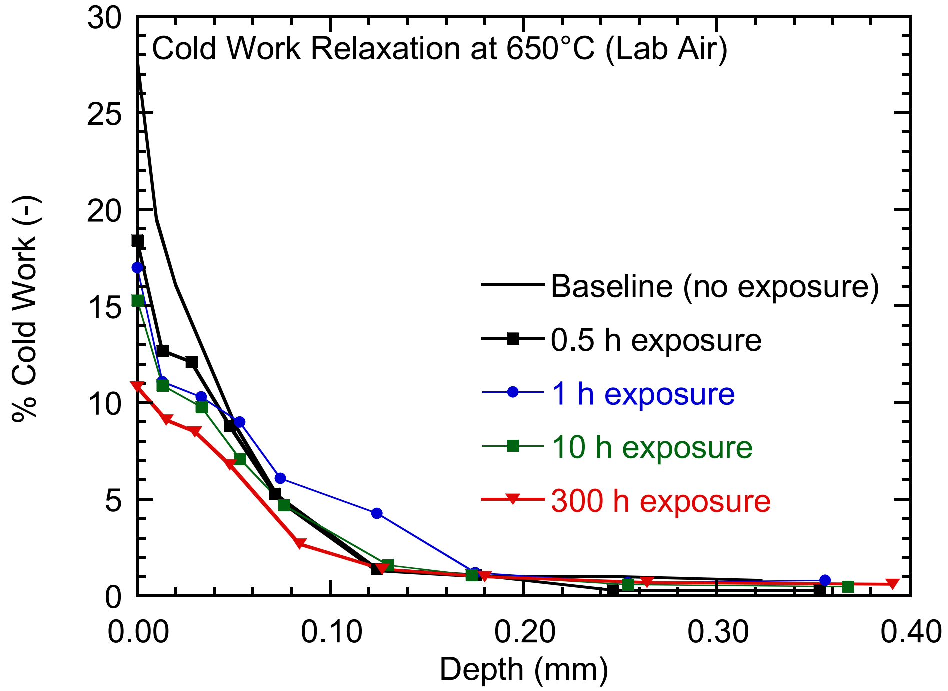

Figure 29. Thermal Relaxation of Cold Work Depth Profile in IN100 at 650°C Taken from Plate C1 as Shown in Table 7.

Applied mechanical loading at elevated temperature may accelerate the rate of residual stress relaxation. Table 8 is the test matrix for the shot peened dogbone specimens subjected to mechanical loading at 650°C. Exposure times for mechanical tests in Table 8 have been selected to match thermal exposure times in Table 7. Fatigue tests have been conducted at a stress ratio ($R = \sigma_{min}/\sigma_{max}$) of R = 0.05 and 20 cycles per minute (20 CPM) with a triangular waveform. Fatigue tests with 0.1, 0.5, and 10 hr exposures translate to one, 600, and 12,000 applied cycles, respectively. Creep tests have been performed at the same loading rate as fatigue, and sustained the applied load for the entire exposure time. The objective for these tests is to characterize the effect of loading waveform (tensile, fatigue, or creep), exposure time (or cycles) and plastic strain on residual stress relaxation in IN100 at 650°C. The experimental measured retained residual stress depth profiles, and model predictions for relaxation, appear in the Model Validation chapter.

Table 8. Thermal-Mechanical Relaxation Test Matrix for IN100.

Cycling Parameters			**Thermal Exposure or Creep-Fatigue Time (Hr)**			
			0.1	**0.5**	**10**	**100**
CPM	**Hertz (/s)**	**Period (s)**	**Number of Applied Cycles (R = 0.05)**			
20	**0.333**	**3.0**	**1**	**600**	**12,000**	**120,000**
		Stress (MPa)				
		-300				**Creep**
		600				**Creep**
		800			**Creep**	
		900	**Single Cycle**	**Fatigue, Creep**	**Fatigue, Creep**	

All mechanical tests on shot peened dogbone specimens include dual extensometry measurements to verify specimen alignment (negligible bending), modulus determination, initial loading and final unloading stress-strain traces. Extensometry data collected during fatigue tests display yielding during initial loading and accumulation of inelastic strain during fatigue, as shown in Figure 30. The single cycle test results in approximately 0.25 percent permanent strain as shown by the point where the unloading curve reaches zero stress. The 600 cycle test exhibits a lower yield point and slightly more strain during loading, approximately 0.3 percent, with an accumulation of an additional 0.05 percent permanent strain during fatigue.

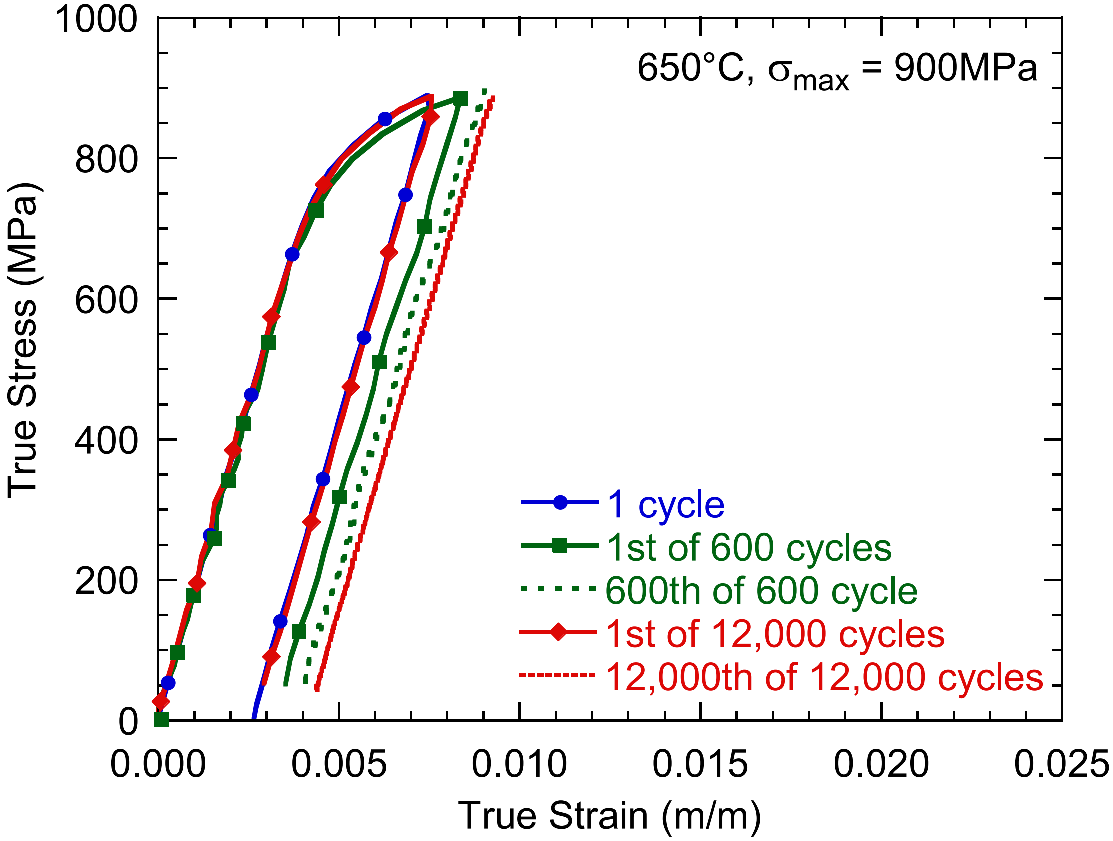

Figure 30. Stress-strain Response of Shot Peened Dogbone Specimen Subject to Fatigue Loading (σ_{max} = 900MPa, R = 0.05) in IN100 at 650°C.

The 12,000 cycle test exhibits an identical load-unload trace to the single cycle test, with an accumulation of an additional 0.15 percent permanent strain during fatigue. As expected, the accumulation of permanent strain increases with increasing cycle count. Overall the accumulation of inelastic strains associated with fatigue cycling (≤ 0.15 percent) is smaller than the 0.25 percent that occurs during the initial loading cycle. Therefore, the most significant change in residual stresses is expected to occur during the initial loading cycle.

Extensometry data collected during creep tests display yielding during initial loading and accumulation of plastic strain during creep, as shown in Figure 31. The single cycle data provides a baseline comparison for evaluating the accumulated permanent strain associated with sustained loads. During the creep tests unloading occurs only at the completion of the test, and therefore unloading data is not shown. However, the initial loading stress-strain response for both the 30 min and 10 hr creep test are identical to the single cycle test, and therefore the accumulated plastic strain associated with creep loading is assumed to be identical, or approximately 0.25 percent. The unloading stress-strain trace of the 30 min creep test shows an accumulation of additional permanent strain of 0.16 percent. Recall that the 600 cycle fatigue test, which has the same exposure time of 30 min, exhibits only 0.05 percent additional permanent strain. For the same maximum applied stress and exposure time of 30 min, creep loading results in more permanent strain than fatigue loading. The 10 hr creep test exhibits significantly more accumulated plastic strain, approximately 0.5 percent, twice the initial loading plastic strain of 0.25 percent. Furthermore the 12,000 cycle fatigue test with the same exposure time and maximum stress as the 10 hr creep test exhibits significantly less accumulated permanent strain. For applied stresses above monotonic yield, sustained load (creep) results in more permanent deformation than fatigue, for the same maximum applied stresses and exposure time.

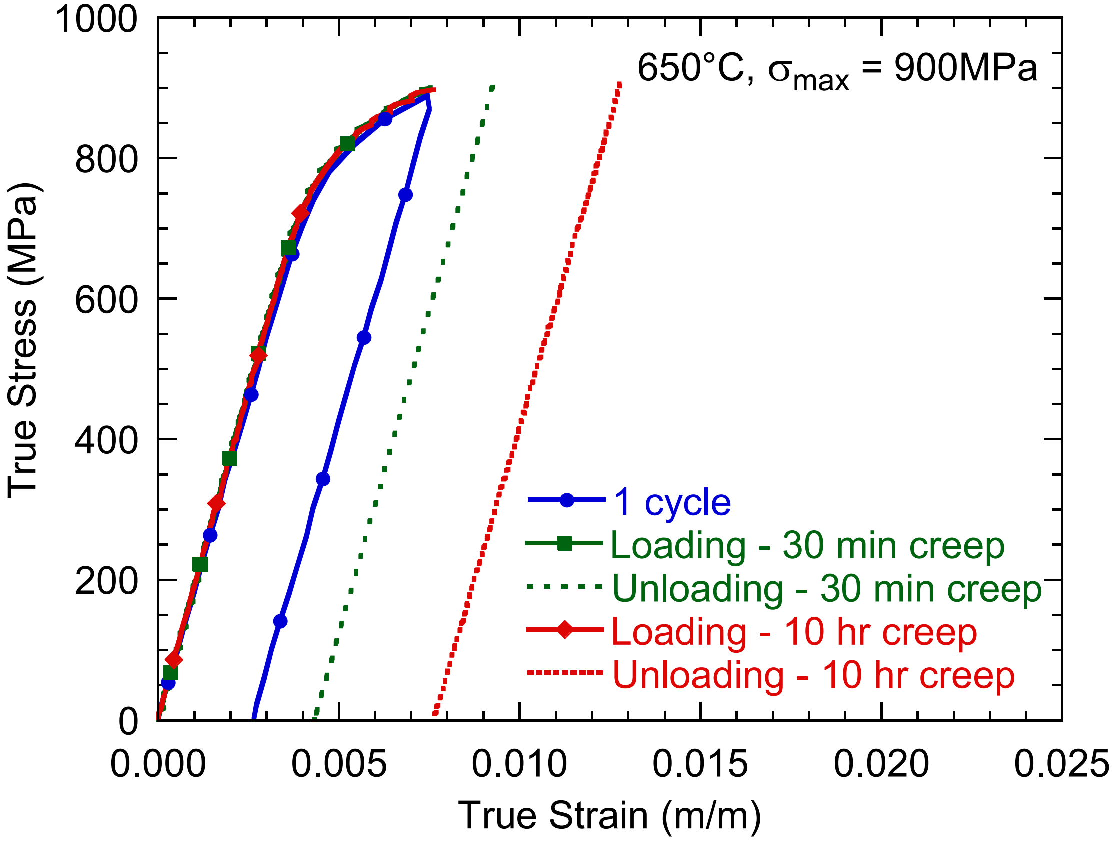

Figure 31. Stress-strain Response of Shot Peened Dogbone Specimen Subject to Creep Loading (σ_{max} = 900 MPa) in IN100 at 650°C.

Applied stresses above yield result in plastic strain on initial loading, and both fatigue and creep tests exhibit an additional accumulation of permanent strain after initial loading. More relevant and interesting is the time dependent material response for applied stresses below yield. To promote measurable results for the elastic applied stresses, in particular 600 MPa tension and 300 MPa compression, the exposure time was increased from ten to 100 hrs. In both cases, under sustained loading for 100 hrs, permanent strain results after unloading. Under a compressive load of 300 MPa, 0.1 percent permanent compressive strain remains, while for a tensile load of 600 MPa, 0.25 percent permanent tensile strain remains.

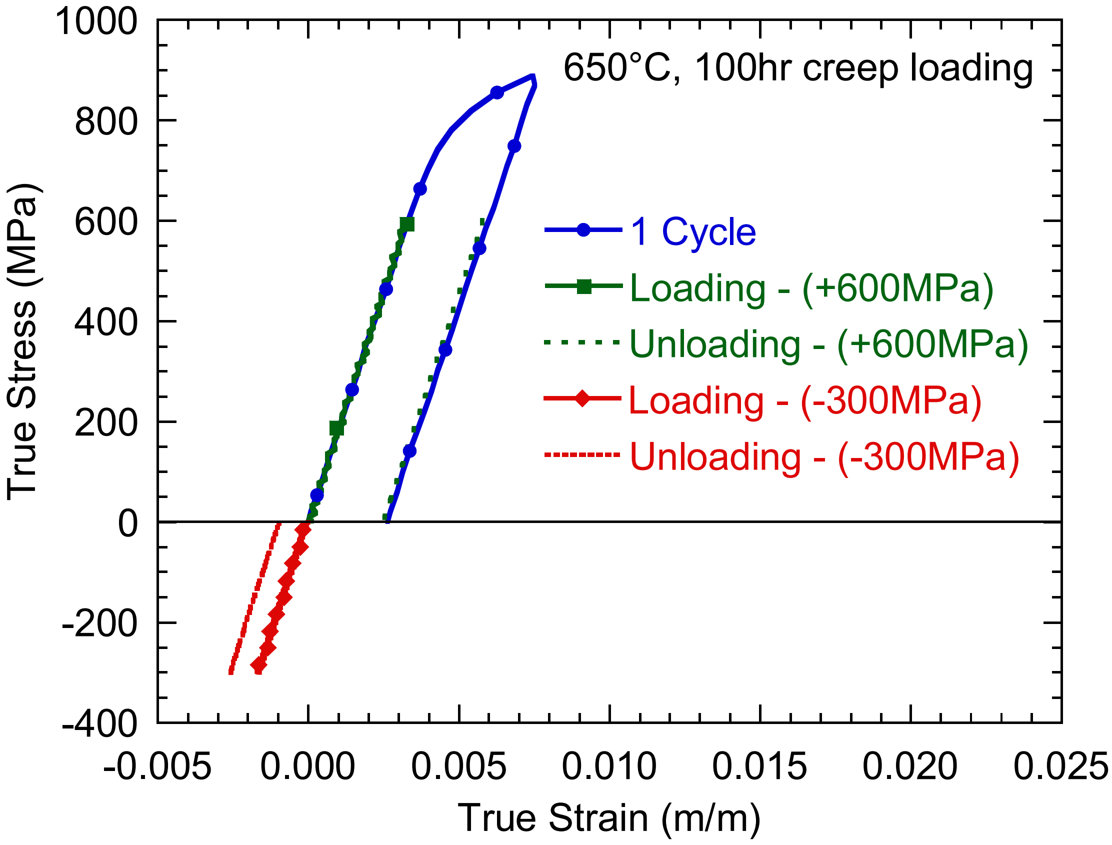

Figure 32. Stress-strain Response of Shot Peened Dogbone Specimen Subject to 100hr Creep in Tension (σ_{max} = 600MPa) and Compression (σ_{min} = -300MPa) in IN100 at 650°C.

Up to this point the discussion has been focused on the effects of mechanically applied stresses on relaxation of shot-peened residual stresses. It is also important to consider how residual stresses affect mechanical behavior. The compressive surface residual stress must be balanced by a compensatory tensile residual stress in the core of the sample as shown in Figure 26. The compensatory tensile residual stress is listed in Table 6 as σ_{int} = 205.7 MPa. Figure 33 is a plot of the true stress versus true strain loading response for a unpeened cylindrical dogbone and shot peened flat dogbone specimens creep tested at 900 MPa and 650°C. The two specimens exhibit the same elastic modulus during loading. However, the stress level when inelastic response begins is lower in the sample with residual stress. The lower yield in the shot peened sample results in additional plastic strain during loading.

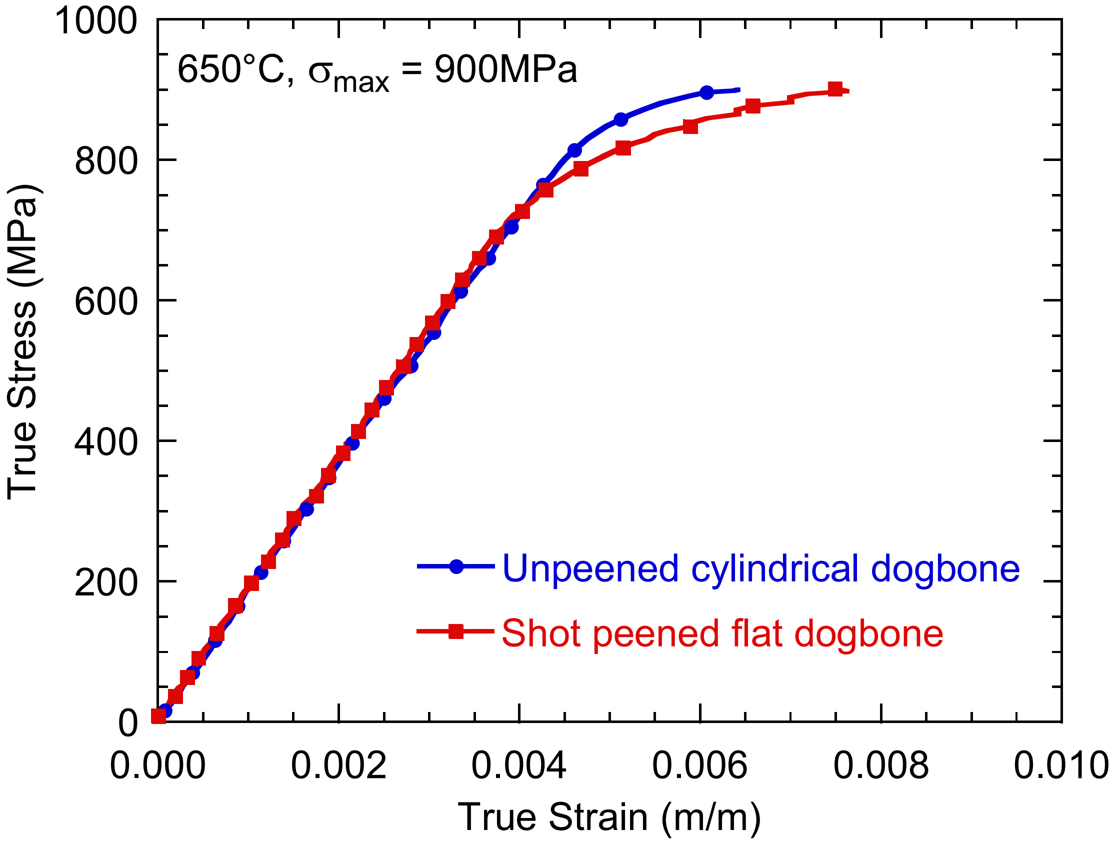

Figure 33. Effect of Shot Peened Residual Stresses on Loading Stress-Strain Response in IN100 at 900 MPa and 650°C.

The difference is not limited to just the loading behavior but also affects the creep response, as shown in Figure 34 in the total strain versus time plot. In addition to the increased strain during loading the shot-peened sample has a higher creep rate, as shown by the growing difference in total strain between the two curves.

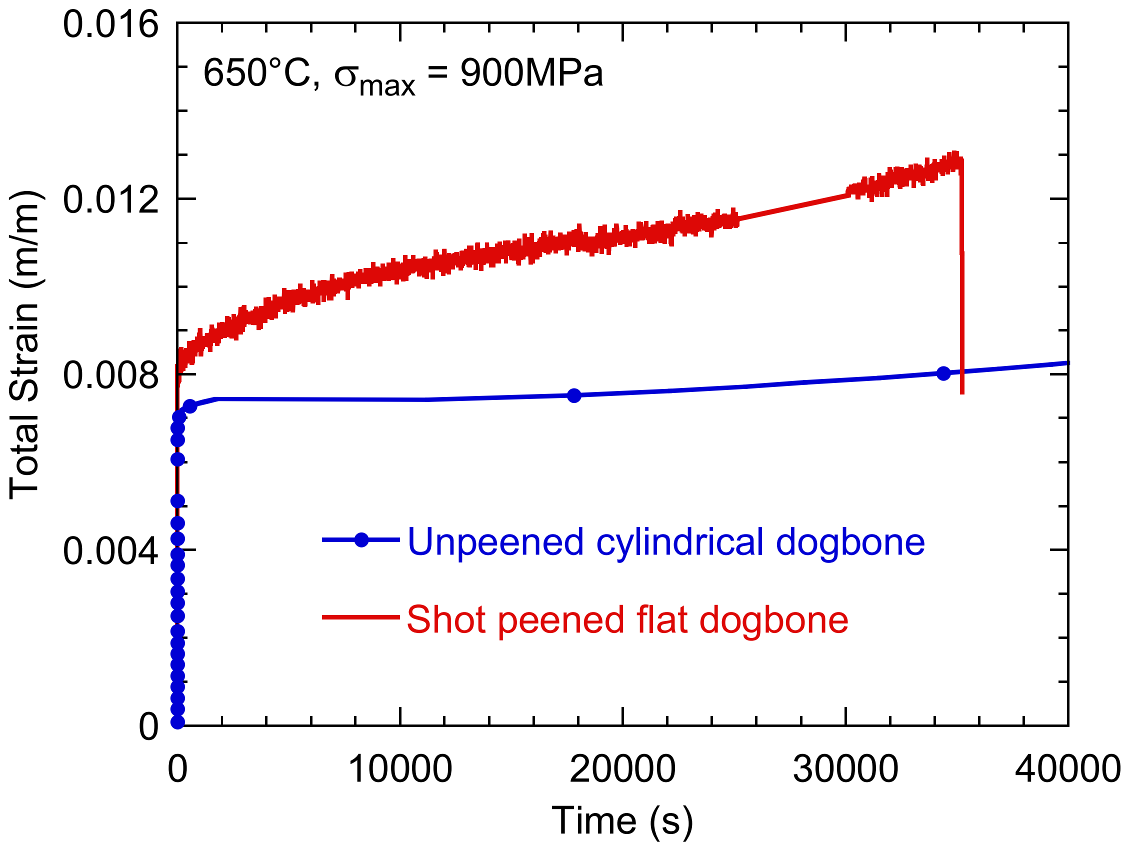

Figure 34. Effect of Residual Stress on Strain versus Time Response in IN100 at 900 MPa and 650°C in Shot Peened and Virgin Samples.

The creep test with applied stress above yield (σ = +900 MPa, t = 10 hr) in Figure 31 exhibits a significant accumulation of permanent strain, while creep tests conducted below yield (σ = +600 MPa, -300 MPa, t = 100 hr) in Figure 32 accumulate permanent strain less than that acquired during the single cycle of loading at 900 MPa. An indication of the maximum applied stress for creep loading that will result in a retained residual stress similar to thermal relaxation alone is the stress level when inelastic response occurs as shown in Figure 33, approximately σ = 750-800 MPa. An additional creep test on a shot peened flat dogbone sample has been performed at an applied stress of 800 MPa for 10 hr. Extensometry measurements during loading and unloading for the 800 and 900 MPa creep tests are shown in Figure 35. The 800 MPa creep test exhibits minor yielding during loading, and accumulated plastic strain similar to the single cycle load-unload test at 900 MPa. The resulting total strain versus time response is shown in Figure 36 with the two unpeened creep curves for comparison. The 800 MPa unpeened sample exhibits very little accumulation in strain beyond the initial loading strain. The 900 MPa unpeened sample experiences yielding during loading, resulting in a higher initial strain, and afterward displays only limited accumulation of strain during creep. In contrast, the 800 MPa peened sample exhibits a slightly higher initial loading strain than the 800 MPa unpeened sample, primarily due to the residual stress. Further, the 800 MPa peened sample displays a continual increase in creep strain under sustained load and approaches the 900MPa unpeened total strain.

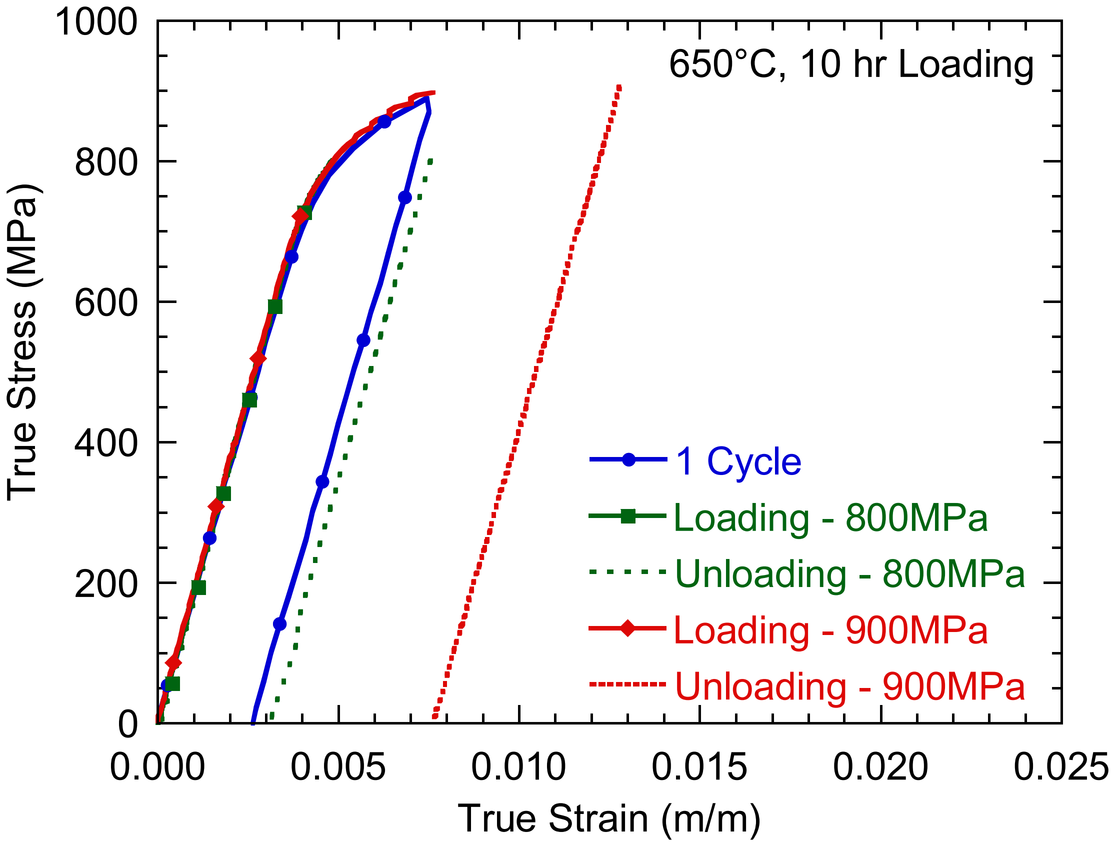

Figure 35. Stress-strain Response of Shot Peened Dogbone Specimen Subject to 10 hr Creep in Tension (σ_{max} = 800 MPa, 900 MPa) in IN100 at 650°C.

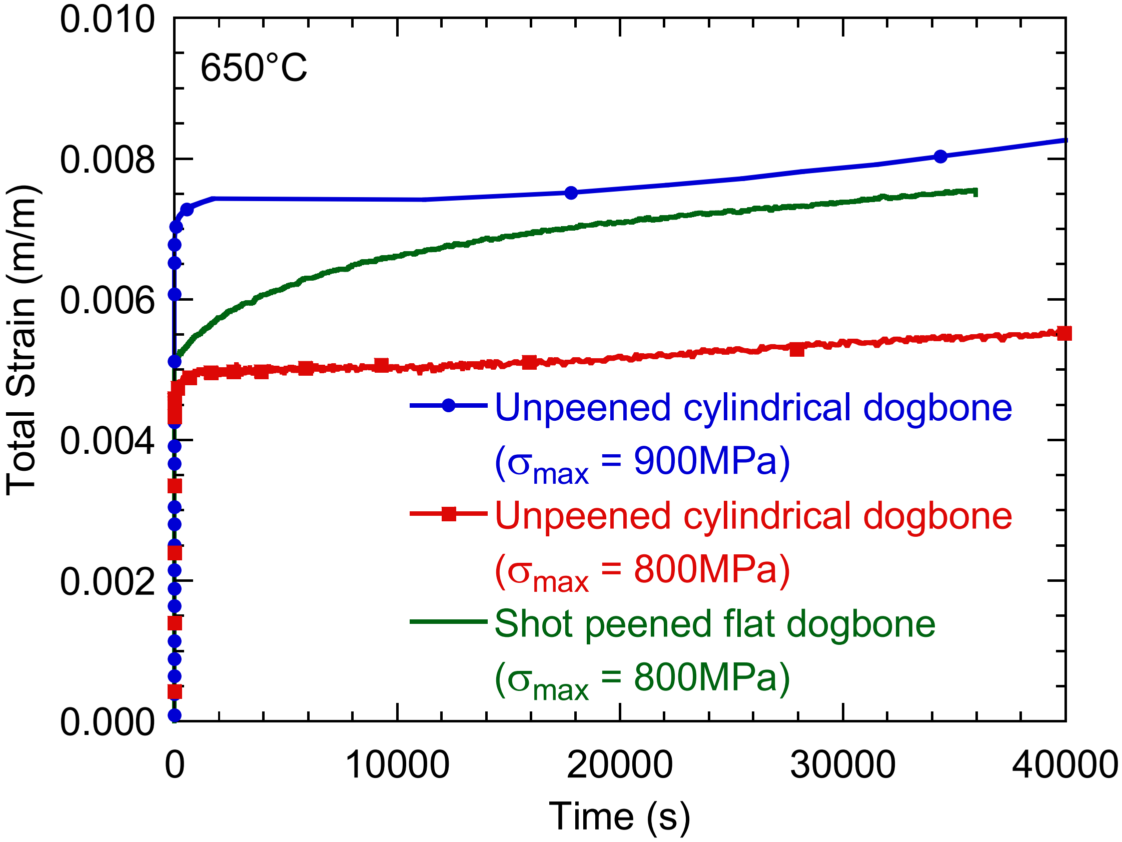

Figure 36. Effect of Residual Stress on Strain versus Time Response in IN100 at 800 MPa & 900 MPa and 650°C in Shot Peened and Virgin Samples.

Analytical Model Development

The constitutive model developed in this study is based on a rate-independent plasticity model, and a strain hardening creep model that is coupled to the plasticity model through the plastic strain rate and yield surface size. The plasticity model is based on the von Mises effective stress with a nonlinear mixed isotropic-kinematic hardening rule as described by Dodds [90]. The creep model follows the physics-based modeling of dominant deformation mechanisms similar to the approaches of Ashby, Dyson, McLean and others [40,49,76-79]. Based on the SEM and TEM observations of the shot peened and thermally exposed microstructure, it has been argued that the microstructure remains stable over the range of temperatures and exposure times in this study. Therefore a microstructural model dominated by a single deformation mechanism is sufficient to model residual stress relaxation behavior. The elastic-plastic-creep model is cast in an implicit integration form suitable as a standard user material subroutine (UMAT) for implementation into ABAQUS/Standard. Details of the physical deformation mechanism, constitutive equations and solution procedure follow.

Coupled Plasticity-Creep Model

Identification of the primary creep deformation mechanism is required before development of a model may begin. One approach to determining the dominant mechanism is to fit the minimum creep rate versus stress data to a power law equation and evaluate the exponent of stress (n). Bulk diffusion through the grain (Nabarro-Herring Creep) and diffusion along grain boundaries (Coble Creep) may be characterized by minimum creep rates that are directly proportional to stress raised to an exponent $n = 1$. Dislocation mechanisms such as climb and glide typically have a power law exponent that is higher and with a range of $n = 3\text{-}5$. The creep rate data from this study exhibit an exponent of $n \approx 6$, and therefore dislocation motion is the primary deformation mechanism for the range of conditions evaluated. Furthermore the applied stresses of 800-1000 MPa which are at and above yield, and moderate temperature of 650°C ($T_h = 0.58$) suggest that dislocation glide is dominant over dislocation climb which is a lower-stress, higher-temperature mechanism. Therefore a creep model with dislocation glide as the dominant deformation mechanism is chosen for this alloy and range of operating conditions.

Many of the viscoplastic models in the literature follow similar arguments about microstructural behavior in the development of the constitutive equation. However, unified models [12,71,72,80-84] that decompose the total strain rate into elastic and inelastic components as shown by

$$\dot{e}_{ij} = \dot{e}_{ij}^{e} + \dot{e}_{ij}^{in} \qquad [8]$$

imply that plastic and creep deformation are one and the same mechanism. Decomposing inelastic behavior into two rate terms enables independent creep and plasticity deformation mechanisms to be incorporated as shown by

$$\dot{e}_{ij} = \dot{e}_{ij}^{e} + \dot{e}_{ij}^{p} + \dot{e}_{ij}^{c} \qquad [9]$$

This approach implies that creep and plasticity are distinct mechanisms. In fact, they are not independent, but are coupled through a backstress tensor and dislocation mobility model which allows the creep strain rate to be dependent on plastic strain rate, plastic strain and the yield surface.

The development of the creep model follows the microstructurally based deformation mechanism approach of Dyson, McLean and colleagues [76-79]. The basic model is adapted to incorporate the effects of prior plastic strain and coupling to the plasticity model. The 1D effective creep strain rate relation, based on glide of dislocations as the dominant deformation mechanism, is defined such that it is identical to the axial component under uniaxial loading,

$$\dot{\bar{\varepsilon}}^{c} = \dot{\varepsilon}_{o}\left(1+\bar{\varepsilon}^{dm}\right) sinh\left(\frac{\bar{\sigma}}{\sigma_{\kappa}\kappa}\right) \qquad [10]$$

where

$\dot{\bar{\varepsilon}}^{c}$ = effective creep strain rate,

$\dot{\varepsilon}_{o}$ = creep strain rate parameter,

$\bar{\varepsilon}^{dm}$ = effective mobile dislocation density,

$\bar{\sigma}$ = effective stress,

σ_{κ} = normalized stress parameter (nondimensional),

κ = size of yield surface.

The microstructural evolution equation for multiplication of mobile dislocations has been modified to incorporate the effect of plastic strain rate as follows:

$$\dot{\bar{\varepsilon}}^{dm} = M\dot{\bar{\varepsilon}}^{p} + N\dot{\bar{\varepsilon}}^{c} \qquad [11]$$

Parameters M and N are coefficients that determine the contributions of plastic strain rate and creep rate toward the increase in dislocation mobility, respectively. In the absence of plastic strain, Equation 11 reduces to the damage rate equation described by McLean and Dyson [76].

The backstress rate ($\dot{\alpha}_{ij}$) is decomposed into components representing yield surface translation ($\dot{\alpha}_{ij}^{p}$), creep backstress ($\dot{\alpha}_{ij}^{c}$), and creep recovery ($\dot{\alpha}_{ij}^{r}$),

$$\dot{\alpha}_{ij} = \dot{\alpha}_{ij}^{p} + \dot{\alpha}_{ij}^{c} - \dot{\alpha}_{ij}^{r} \qquad [12]$$

The creep backstress evolution equation is adapted from the nonlinear kinematic hardening rule developed by Armstrong and Frederick [113] for plasticity,

$$\dot{\alpha}_{ij}^{c} = \frac{2}{3} C_c \dot{\varepsilon}_{ij}^{c} - \gamma_c \alpha_{ij}^{c} \dot{\bar{\varepsilon}}^{c} \qquad [13]$$

with parameters for strain hardening (C_c) and strain softening (γ_c). The recovery evolution model,

$$\dot{\alpha}_{ij}^{r} = C_1 \alpha_{ij}^{p} \dot{\bar{\varepsilon}}^{p} \qquad [14]$$

is strictly a function of plastic material behavior and is analogous to the strain softening term in Equation 13. Plastic hardening rules follow the approach in Dodds [90] in the form:

$$\dot{\alpha}_{ij}^{p} = \frac{2}{3} H'(1-\beta) \dot{\varepsilon}_{ij}^{p} \qquad [15]$$

$$\dot{\kappa} = \beta H'\left(\varepsilon^{p}\right) \dot{\bar{\varepsilon}}^{p} \qquad [16]$$

This formulation incorporates the Bauschinger effect with a mixed nonlinear isotropic-kinematic model where β defines the portion of isotropic hardening and H' is the plastic modulus. Pure isotropic hardening occurs when β = 1 and pure kinematic hardening when β = 0.

As usual, it is assumed that hydrostatic stresses have negligible effect on yield behavior and that during plastic flow the material is incompressible. This assumption is also taken to be valid for creep deformation [114-116]. Therefore all constitutive equations have been based on deviatoric forms of the stress and strain tensors as shown below.

$$s_{ij} = \sigma_{ij} - \frac{\sigma_{kk}}{3}\delta_{ij} \quad ; \quad e_{ij} = \varepsilon_{ij} - \frac{\varepsilon_{kk}}{3}\delta_{ij} \qquad [17]$$

The elastic relationship between stress and strain, shown below in deviatoric form, is the basis for integrating the stresses to the end of the time step.

$$\dot{e}_{ij}^{e} = \frac{\dot{s}_{ij}}{2G} \quad or \quad \dot{s}_{ij} = 2G\dot{e}_{ij}^{e} \qquad [18]$$

Combining the elasticity equation with the additive strain rate, Equation 9, provides an equation for the dependent stresses in terms of the independent strain rates as,

$$\dot{s}_{ij} = 2G\left(\dot{e}_{ij} - \dot{e}_{ij}^{p} - \dot{e}_{ij}^{c}\right) \qquad [19]$$

We adopt Prandtl-Reuss flow equations for both plasticity and creep rate, identifying $\dot{\lambda}_p$ and $\dot{\lambda}_c$ as positive scalar quantities representing the different deformation histories,

$$\dot{\varepsilon}_{ij}^{p} = \dot{\lambda}_p\left(s_{ij} - \alpha_{ij}^{p}\right) \quad ; \quad \dot{\varepsilon}_{ij}^{c} = \dot{\lambda}_c\left[s_{ij} - \left(\alpha_{ij}^{p} + \alpha_{ij}^{c} - \alpha_{ij}^{r}\right)\right] \qquad [20]$$

The effective plastic strain rate, effective creep rate and von Mises effective stress are defined respectively as,

$$\dot{\bar{\varepsilon}}^{p} = \sqrt{\frac{2}{3}\dot{e}_{ij}^{p}\,\dot{e}_{ij}^{p}} \;;\quad \dot{\bar{\varepsilon}}^{c} = \sqrt{\frac{2}{3}\dot{e}_{ij}^{c}\,\dot{e}_{ij}^{c}} \;;\quad \bar{\sigma} = \sqrt{\frac{3}{2}\left(s_{ij} - \alpha_{ij}\right)\left(s_{ij} - \alpha_{ij}\right)} \qquad [21]$$

The nonlinear stress-strain equation that relates the effective plastic strain to the von Mises effective stress is best described by an equation attributed to Ludwik [118] as shown by,

$$\overline{\sigma} = \sigma_o + K\left(\overline{\varepsilon}^{\,p}\right)^n \qquad [22]$$

where σ_o is the virgin yield strength, K is the strain hardening coefficient, and n is the strain hardening exponent.

Integration of the solution forward in time starts by estimating the creep strain increment for the current material point based on the stress state and state variables at the beginning of the step. The predicted creep strain increment is subtracted from the supplied total strain increment to produce an elastic-plastic strain increment. An elastic-plastic solution follows to calculate an effective plastic strain increment and the stresses at the end of the time step, based on the predicted elastic-plastic strain increment. Then a corrected creep strain increment is calculated based on stresses calculated at the midpoint of the step. The corrected creep strain increment is used to calculate an improved prediction for state variables at the end of the step. The correction procedure is repeated until the difference between the predicted and corrected stresses at the end of the step reaches a specified tolerance limit. If more than a specified number of corrections are needed to achieve the tolerance, a request to cut the time step is returned to ABAQUS. The solution for the elastic-plastic portion of the model follows the work of Braisted and Brockman [117] on a rate-dependent implicit model for Ti-6Al-4V. The solution was adapted to a rate-independent nonlinear isotropic-kinematic hardening model described by Dodds [90]. A flowchart for the UMAT is shown in Figure 37.

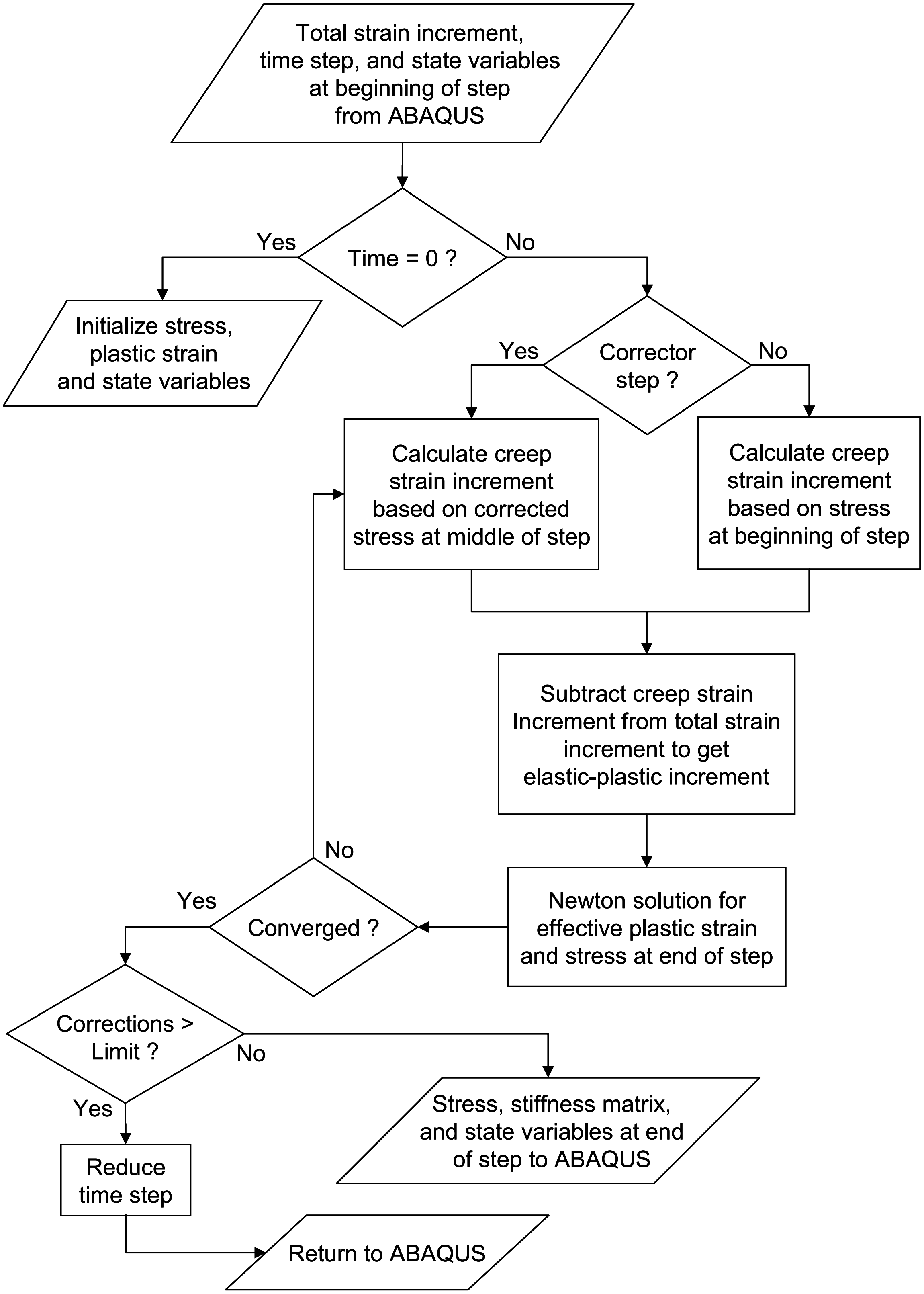
Total strain increment,
time step, and state variables
at beginning of step
from ABAQUS
Time = 0 ?
Yes
No
Initialize stress,
plastic strain
and state variables
Corrector
step ?
Yes
No
Calculate creep
strain increment
based on corrected
stress at middle of step
Calculate creep
strain increment
based on stress
at beginning of step
Subtract creep strain
Increment from total strain
increment to get
elastic-plastic increment
Newton solution for
effective plastic strain
and stress at end of step
Converged ?
No
Yes
Corrections >
Limit ?
No
Yes
Stress, stiffness matrix,
and state variables at end
of step to ABAQUS
Reduce
time step
Return to ABAQUS

Figure 37. Flowchart of Coupled Creep-Plasticity Model User Material Subroutine.

Model Validation and Prediction Analysis

The coupled creep-plasticity model described in the previous section has been calibrated using creep data with prior plastic strain as described in the experimental study section. A one dimensional model of the constitutive equation has been developed as an expedient method to determine the constitutive parameters and associated confidence limits. The parameters deduced from tensile, creep and cyclic tests fit to the one dimensional form of the coupled creep-plasticity model have been implemented into the computational material model.

The coupled creep-plasticity model is composed of elastic, plastic and creep models that are separate but not independent as described by Equation 9. However, experiments provide just one measurable dependent variable, total strain. Furthermore, since the three models (elastic, plastic, creep) are activated by stress level, not all provide contributions to the total strain or strain rate at every point in the loading history. For example, during loading especially at low stresses, the total strain is elastic only, with no contribution from plasticity or creep. At higher stresses, prior to yield, creep strain will develop and add to the elastic strain. When the yield stress is reached, plastic strain will develop and add to the elastic and creep strain. As yielding continues, plastic and creep strains increase quickly, while the elastic strain rate starts to decrease. Finally when the target stress is reached, elastic and plastic strain accumulation stops and total strain is driven by creep strain only.

The discontinuous contributions of elastic, plastic and creep strains to the total strain provides difficulty for curve fitting schemes that determine the parameters for the three models simultaneously. For example, the initial elastic loading response is controlled by the elastic model only, yet the curve fitting schemes modify all parameters simultaneously to optimize the fit. An additional difficulty is the coupling of the creep model to the plastic model. A small change in plastic response may produce a significant change in creep response. The third and final difficulty comes from the experimental data itself. Although each test has an identical prescribed loading rate of 175 MPa/s the stress-strain response for each specimen exhibits some variability from nominal behavior. The variability in modulus, yield point, and hardening all contribute to differences in plastic strain at peak stress from the model. As a result the model does not capture the individual response of each specimen. This result is that a small change in plastic strain produces a large change in creep response.

A more robust and straightforward approach is to first determine parameters for the rate-independent models (elastic and plastic) and then fix those values to determine the parameters for the rate-dependent model (creep). This is the approach followed in the present study, and why analysis of the elastic and plastic response has been discussed in the experimental chapter.

Predictions for creep tests at different stresses and prestrains along with the experimental data described earlier are shown in Figures 38-48. Overall, the coupled creep-plasticity model captures the effects of prior plastic strain and plastic strain during loading on the creep response. In some cases, the model captures the correct shape while exhibiting an offset from the experimentally measured total strain. For example, the model prediction in Figure 38 exhibits the correct shape, but under predicts the peak strain rate and displays a shift to the left from the data, in the creep dominated region. This difference between the model and the data is a result of this particular specimen displaying slightly higher hardening than observed in nominal behavior. Since the hardening was higher, the accumulated plastic strain after yielding was lower. This results in the model predictions being shifted to the left from the data. Table 9 summarizes all the parameters in the model and their respective confidence intervals. It is important to note that the confidence intervals for the elastic and plastic parameters in Table 9 are different than those reported in Table 3. The confidence interval is based on both the experimental data and the model. The parameters and confidence intervals, in Table 3 and Equation 6, relate stress to total strain (elastic and plastic). In contrast, Table 9 and the coupled creep-plasticity model relate total strain rate as a function of stress, time and all the state variables. In summary, the parameters are the same for different models, while the confidence intervals for the parameters are dependent on the model. It is for this very reason that the extra effort to determine the confidence interval on the parameters and model predictions must be completed. The confidence intervals provide feedback on the choice of the model as well as the contribution of the parameters in the model. The parameters in Table 9 indicate that σ_o, M, and N have extremely large uncertainties. This indicates a large change in the parameter is required to have a small change in the solution, or the parameter is only important for a small fraction of the total data set. In particular, σ_o has a large uncertainty for both reasons mentioned above. First, a large change in σ_o produces a tiny change in plastic strain in this material and for the range of stresses studied. Second, the value of σ_o is different for room temperature, elevated temperature monotonic loading, and elevated temperature cyclic loading. The elevated temperature monotonic value, which is the value reported in Table 9, only applies to the three test cases of zero percent prestrain. Therefore σ_o is not well represented in this total data set. The large uncertainty in σ_o drives the uncertainty in M because of the coupling between the creep and plastic models. If σ_o is held constant in the uncertainty analysis, the percent uncertainty of M drops to 0.13, confirming the coupling. The creep strain rate parameter N has little contribution to the entire data set. Only for the case of zero plastic strain and elastic loading (σ = 800 MPa) will the N parameter provide any contribution to the dislocation mobility. In all other cases, the plastic strain rate parameter M, is the dominant term for dislocation mobility.

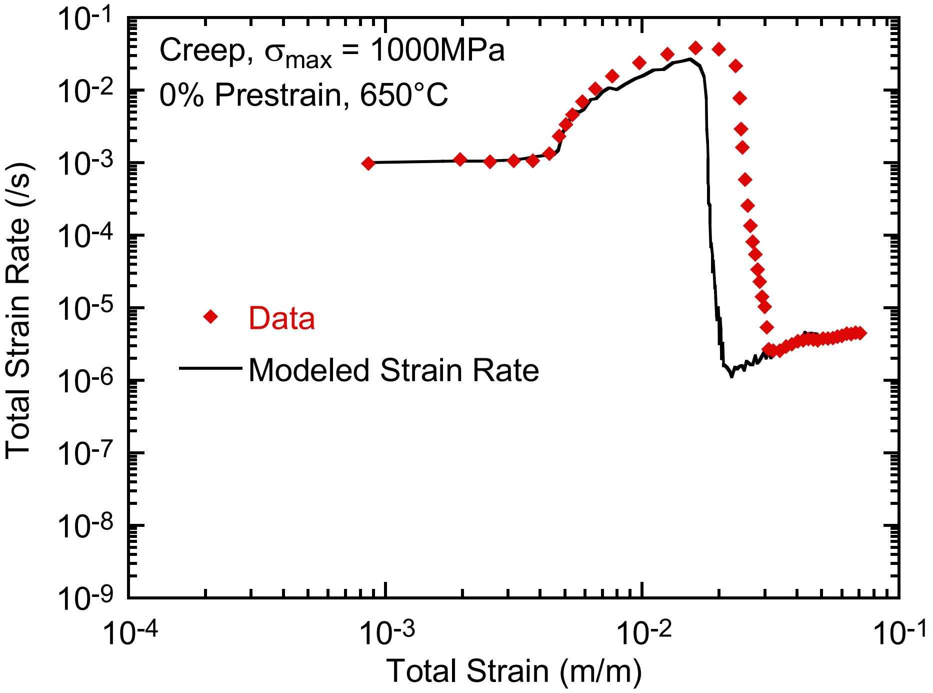

Figure 38. Total Strain Rate versus Total Strain for IN100 at σ_{max} = 1000 MPa, 0% RT Prestrain, and 650°C.

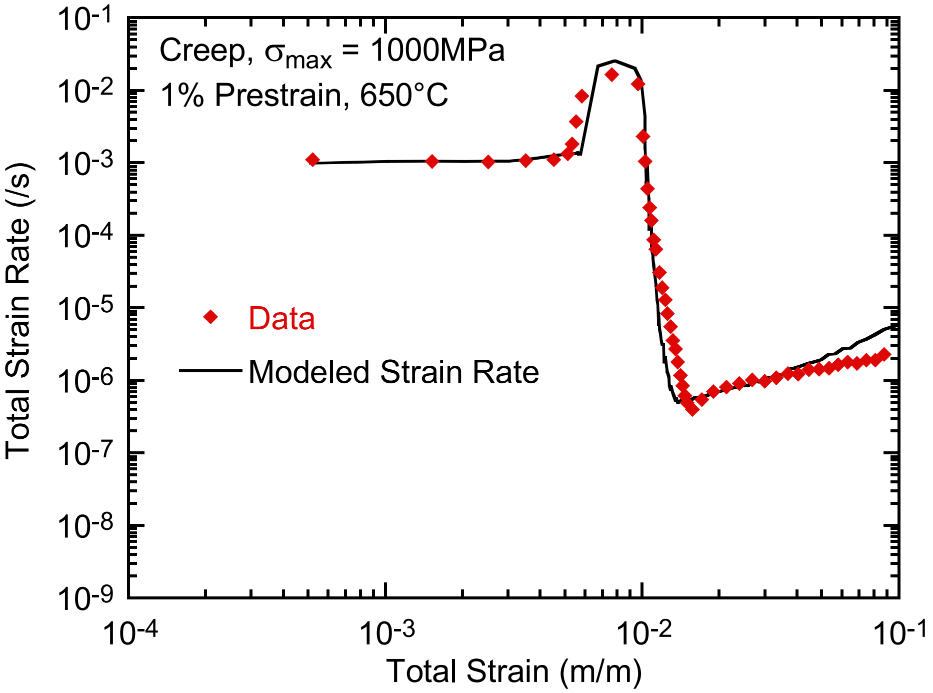

Figure 39. Total Strain Rate versus Total Strain for IN100 at σ_{max} = 1000 MPa, 1% RT Prestrain, and 650°C.

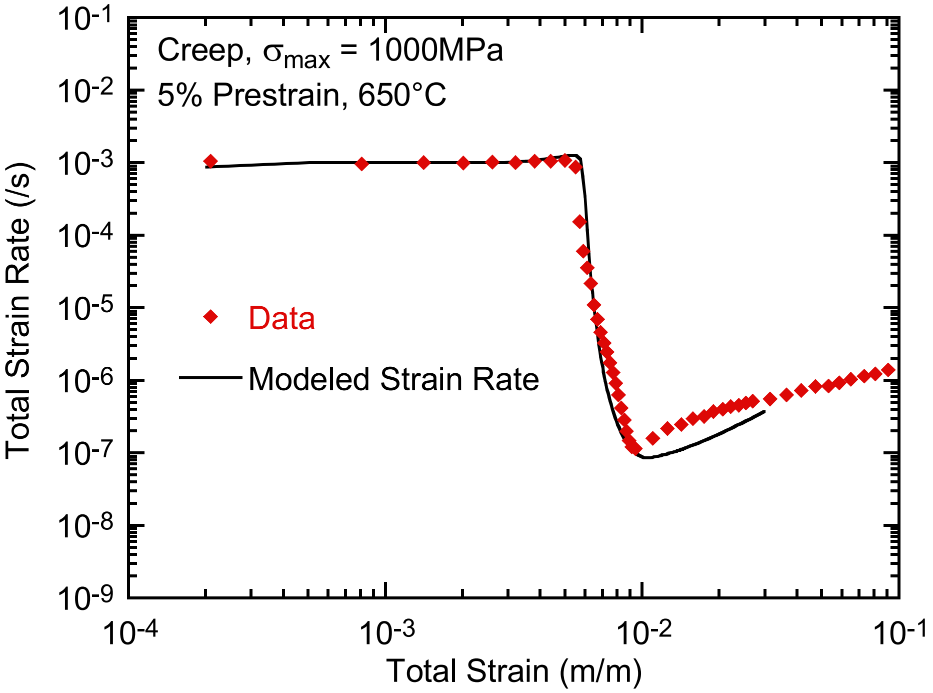

Figure 40. Total Strain Rate versus Total Strain for IN100 at σ_{max} = 1000 MPa, 5% RT Prestrain, and 650°C.

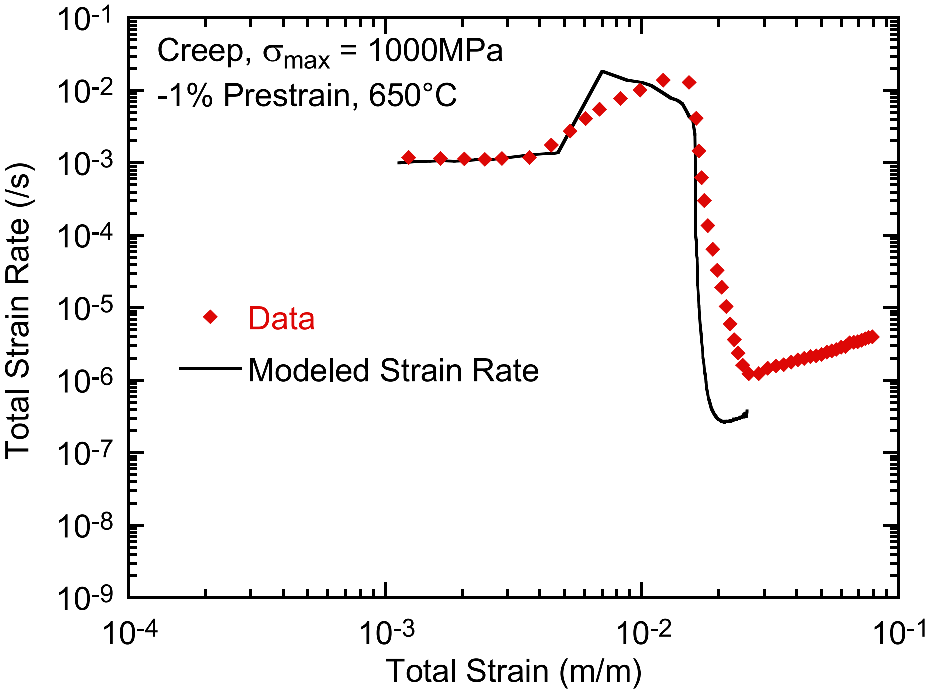

Figure 41. Total Strain Rate versus Total Strain for IN100 at σ_{max} = 1000 MPa, -1% RT Prestrain, and 650°C.

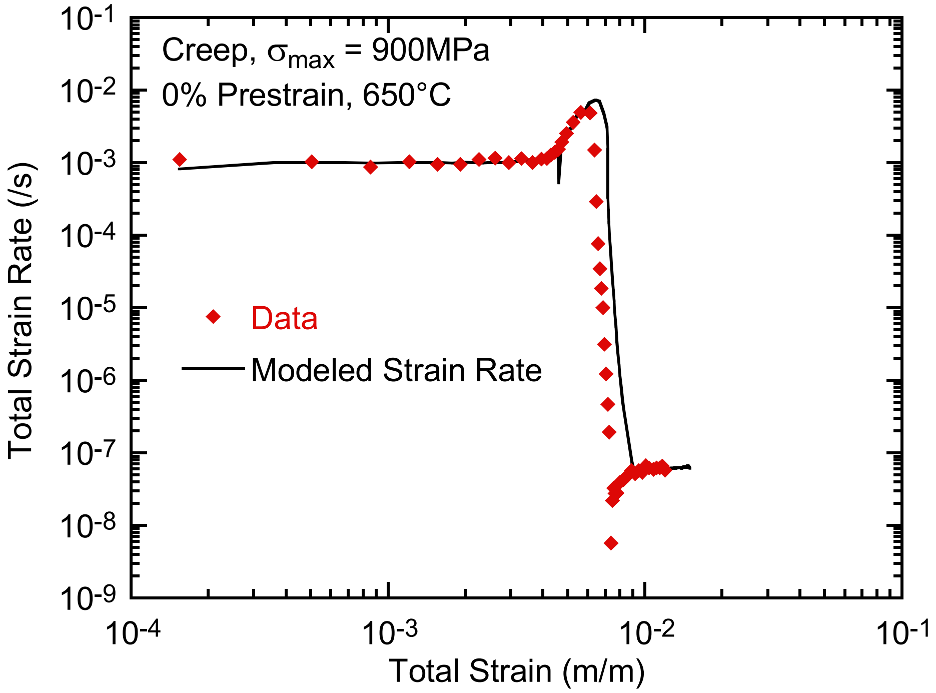

Figure 42. Total Strain Rate versus Total Strain for IN100 at σ_{max} = 900 MPa, 0% RT RT Prestrain, and 650°C.

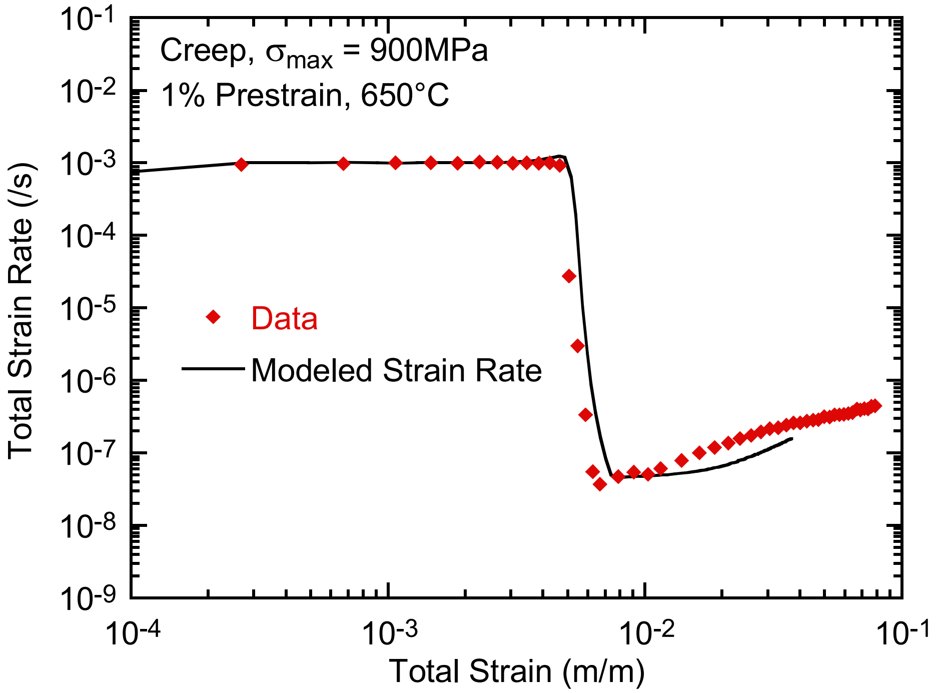

Figure 43. Total Strain Rate versus Total Strain for IN100 at σ_{max} = 900 MPa, 1% RT Prestrain, and 650°C.

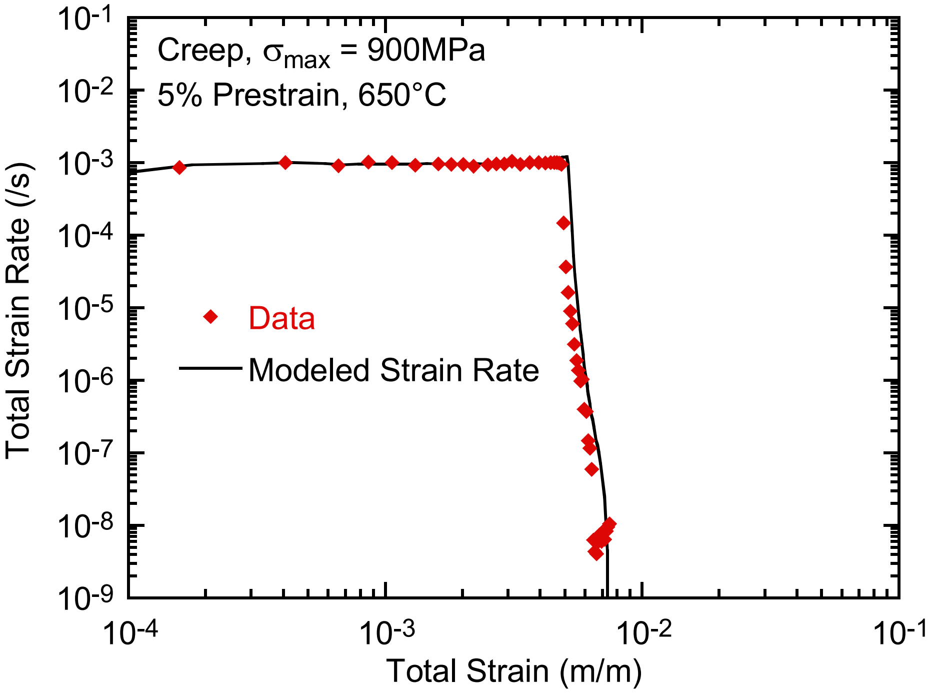

Figure 44. Total Strain Rate versus Total Strain for IN100 at σ_{max} = 900 MPa, 5% RT Prestrain, and 650°C.

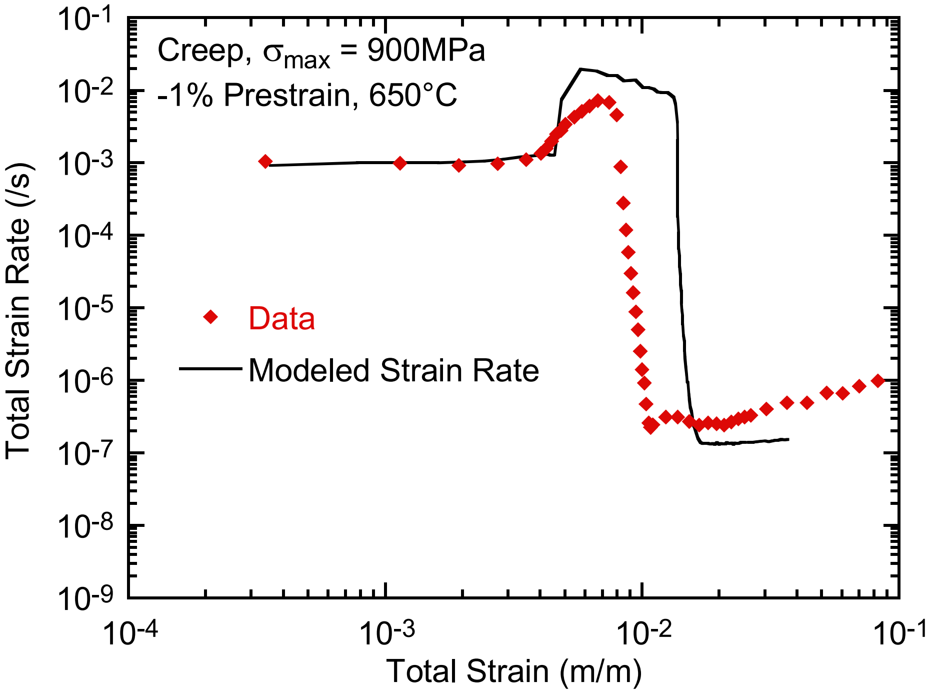

Figure 45. Total Strain Rate versus Total Strain for IN100 at σ_{max} = 900 MPa, -1% RT Prestrain, and 650°C.

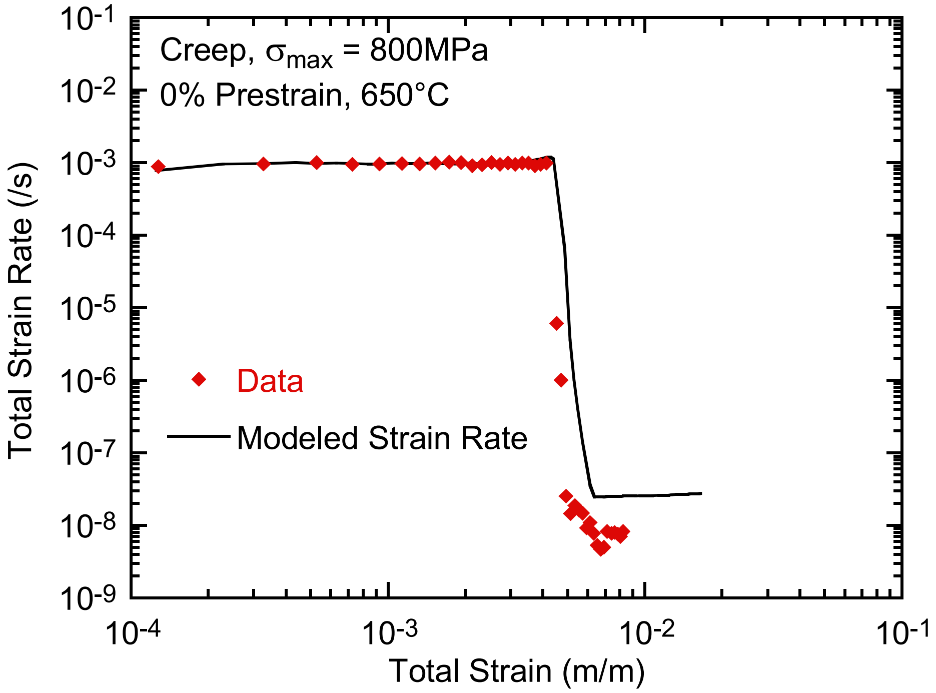

Figure 46. Total Strain Rate versus Total Strain for IN100 at σ_{max} = 800 MPa, 0% RT Prestrain, and 650°C.

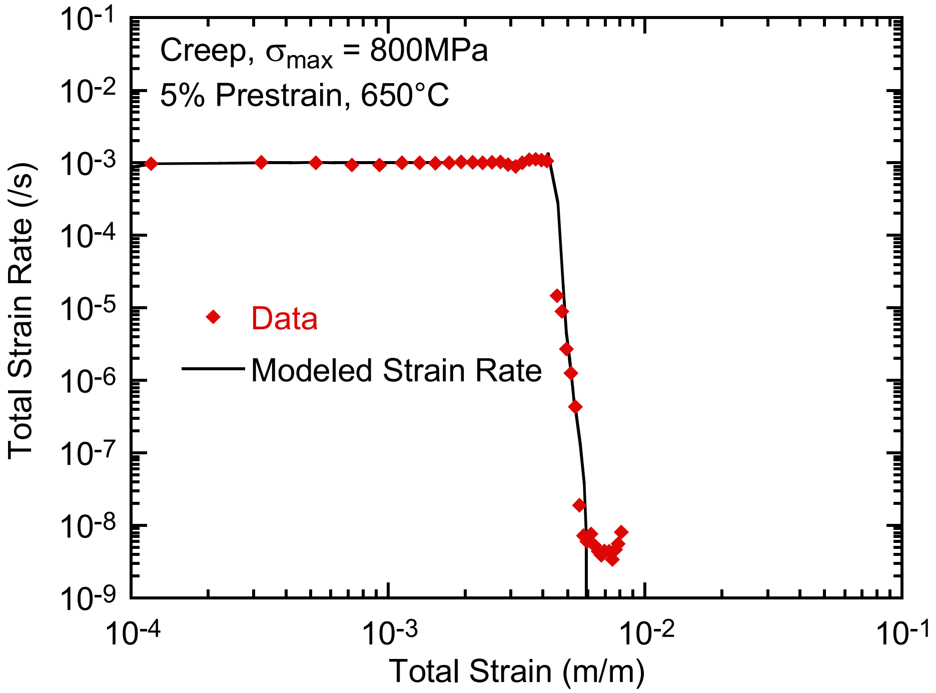

Figure 47. Total Strain Rate versus Total Strain for IN100 at σ_{max} = 800 MPa, 5% RT Prestrain, and 650°C.

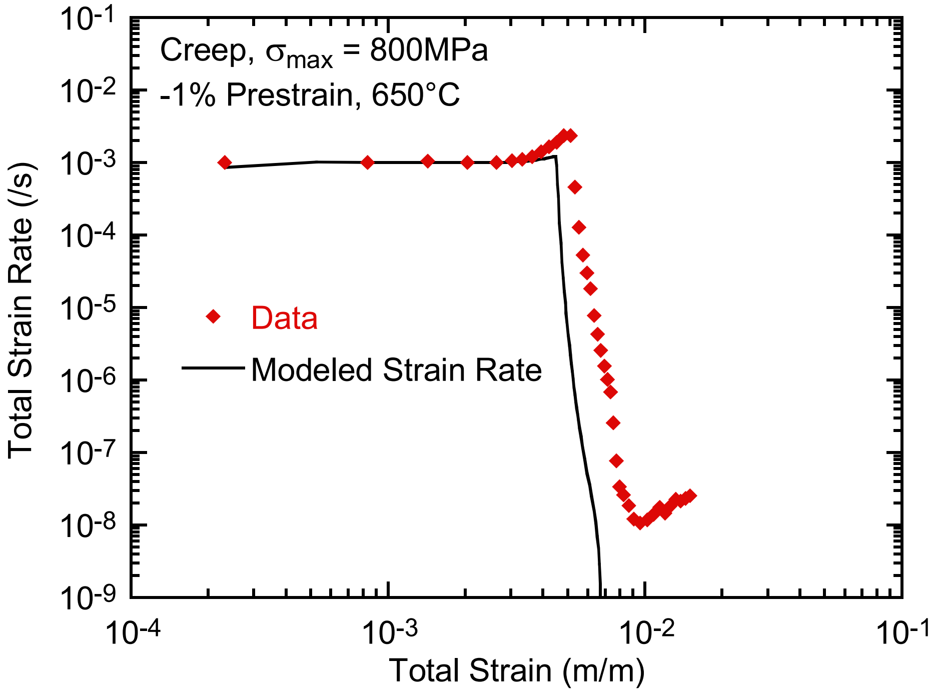

Figure 48. Total Strain Rate versus Total Strain for IN100 at σ_{max} = 800 MPa, -1% RT Prestrain, and 650°C.

Table 9. Parameters in Coupled Creep-Plasticity Model for IN100 Creep Data at 650°C.

Parameter (a)	Parameter Estimate	95% Upper Limit	95% Lower Limit	% Uncertainty of Parameter (σ_a / a)
M (-)	525.0	3.22E+06	-3.22E+06	3.13E+05
C_1 (-)	80.0	80.2	79.8	0.13
ε_o (/s)	3.50E-09	3.58E-09	3.42E-09	1.11
C_c (MPa)	7.68E+05	7.84E+05	7.52E+05	1.08
γ_c (-)	980	998	962	0.91
β (-)	0.450	0.457	0.443	0.79
σ_κ (-)	0.070	0.071	0.069	0.98
E (MPa)	1.80E+05	2.19E+05	1.41E+05	11.14
K (MPa)	1355	1399	1311	1.68
n (-)	0.406	0.413	0.399	0.85
N (-)	12.0	3.68E+04	-3.68E+04	1.57E+05
σ_o (MPa)	799.6	6.17E+12	-6.17E+12	3.94E+11

CHAPTER IV

MODEL APPLICATION

The proposed coupled creep-plasticity model has been shown to be capable of reproducing material responses over complex loading histories in which inelastic prestrain affects the subsequent creep behavior rather dramatically. This chapter considers the analysis of relaxation of shot peened residual stresses in IN100 subjected to mechanical loading. Model predictions corresponding to residual stress relaxation of shot peened dogbone specimens described in the experimental study chapter are presented to demonstrate the effectiveness of the proposed coupled model for problems involving sharp spatial gradients, such as those encountered in shot-peened components.

Finite Element Model of Relaxation Specimen

The flat dogbone specimen geometry described in the experimental study has been designed with both experimental and analytical considerations in mind. The large flat surface of the dogbone sample provides a uniform state of stress in the plane of the sample over an area sufficient for averaging XRD measurements as a function of depth into the sample. The steep gradient and shallow depth of the residual stress profile of shot peening requires an element thickness of approximately five microns at the surface to accurately represent the stress distribution. Therefore a relatively simple and small geometry is desirable, given the required element size.

Figure 49 is an illustration of the dogbone specimen, an enlarged view of the gage section, and a core of the gage section that represents the geometry of the finite element model. The actual model exploits symmetry so only a half-thickness geometry is chosen for the analysis. The dimensions of the finite element geometry are 100 μm x 100 μm x 1 mm. Uniform displacement boundary conditions are enforced on the surface of the model. This is a reasonable assumption given that the tractions applied to the specimen grip section are far from the gage section. Also, the shot-peened layer is a small fraction of the depth (approximately one tenth), and therefore will provide negligible resistance to the bulk of the thickness deforming uniformly.

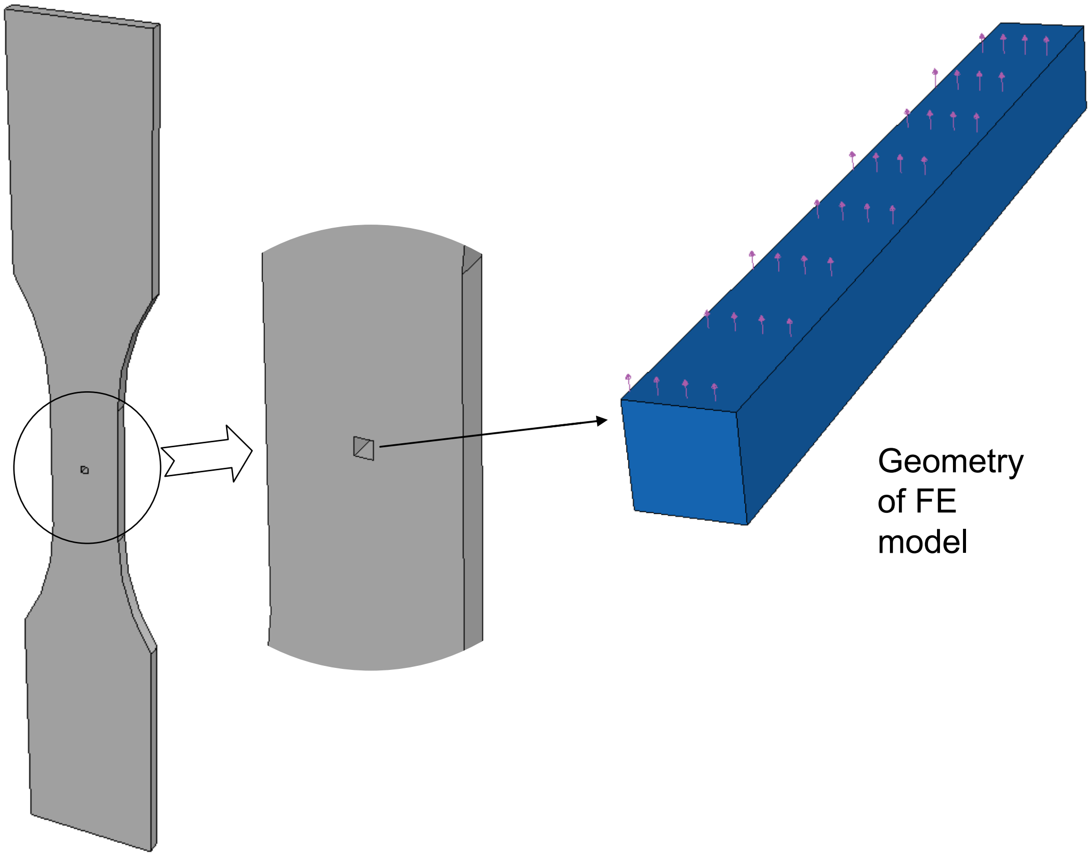

Figure 49. Schematic of Dogbone Specimen, Gage Section and Finite Element Geometry.

The finite element representation of the geometry is shown in Figure 50. The width and thickness of the geometry are divided into three elements to maintain a reasonable aspect ratio for the thin elements near the surface. The thickness of elements increases into the depth as the shot peening stress gradient decreases away from the surface. The mechanical loading is simulated by applying a uniform pressure on the surface in the 2-direction. This geometry and the finite element model provide suitable boundary conditions and sufficient mesh refinement to capture the residual stresses. It is also reasonably small so that the cyclic loading waveform of the test specimens can be simulated in detail.

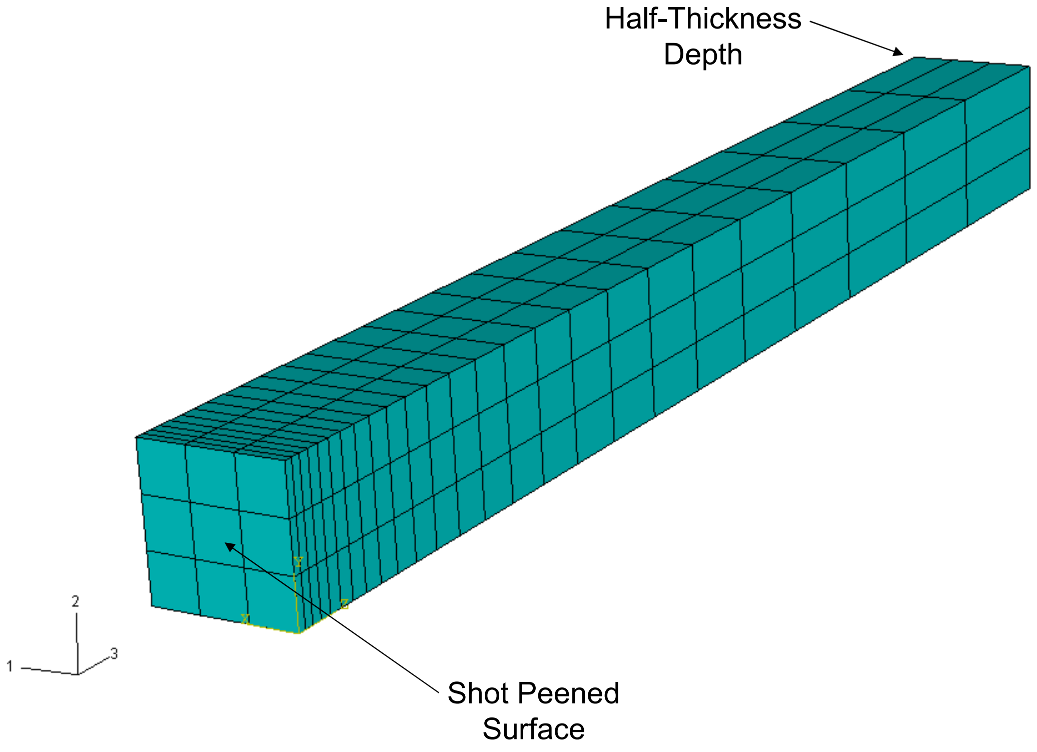

Figure 50. Finite Element Model of Center of Gage Section used for Relaxation of Residual Stresses in Dogbone Specimens.

Model Predictions for Residual Stress Relaxation

Predictions for retained residual stresses subject to load-unload, fatigue and creep are described below. The figures include experimental XRD measured residual stress profiles on shot-peened dogbone specimens, and the baseline no-exposure residual stress profile described by Equation 7, and parameters in Table 6. Residual stress depth profiles in the loading direction (axial) and transverse to the loading direction (trans) have been experimentally measured using XRD and predicted using the coupled creep plasticity model. The transverse residual stress profile provides a complementary residual stress profile for comparison with axial results and provides a second comparison with predictions. Unfortunately, axial and transverse residual stresses are not independent, but coupled together through the constant volume assumption of plasticity and creep, i.e., ($\Delta\varepsilon_{kk}^{p} = \Delta\varepsilon_{ii}^{c} = 0$).

Predictions for retained residual stresses for a single mechanical loading cycle are shown in Figure 51. The maximum applied stress of 900 MPa results in yielding as shown by the stress-strain trace in Figure 30. Two specimens, tested at these conditions, are averaged and shown as a solid line representing the mean response with error bars displaying the range of the XRD measurements for both the axial and transverse residual stress profiles. The range in the XRD measurements is greatest in the region where the residual stress profile has the largest value of compressive residual stress. This is expected since the errors in depth measurement, and stress correction for material removal, are greatest in the shallow depth region. Surprisingly, the range of XRD measurements at the surface is small for both the axial and transverse orientations.

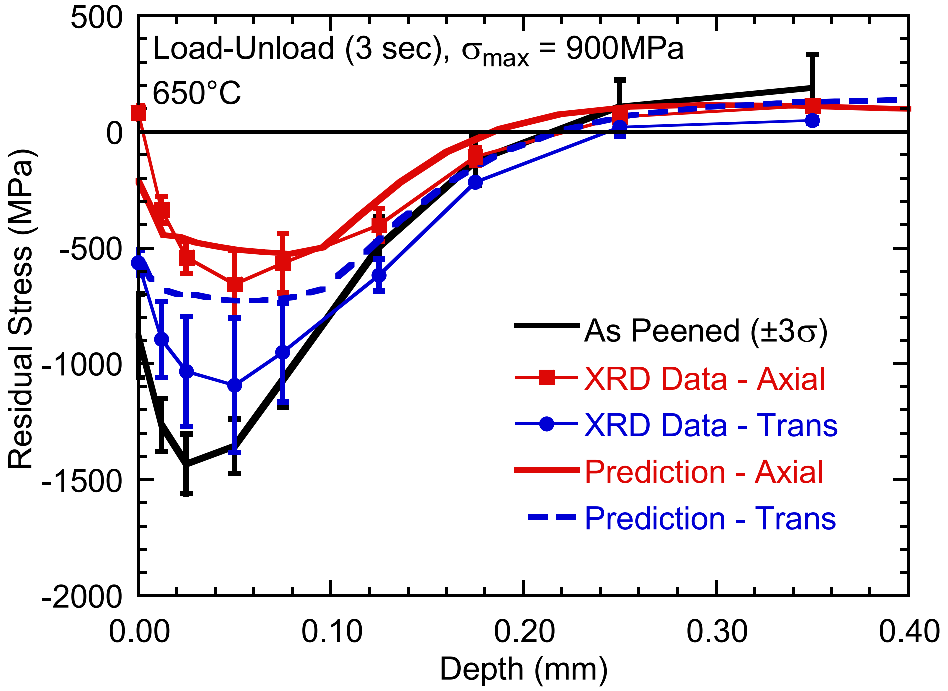

Figure 51. Prediction for Retained Residual Stresses in Shot Peened Dogbone Specimen from Single Load-Unload Cycle in IN100 at 900 MPa and 650°C.

The axial residual stress profile displays more relaxation than the transverse orientation as anticipated. The predictions for axial and transverse profiles, shown as the thick lines without symbols, capture the residual stress relaxation trends. Surprisingly, the data display a small tensile surface residual stress in the axial orientation. It has been demonstrated in the literature [120] that gross plastic straining of the entire cross section can reverse the residual stress profile, such that tensile residual stresses occur on the surface and compression in the center.

Predictions for retained residual stresses under fatigue loading of 600 cycles (30 min) are shown in Figure 52. The maximum applied stress of 900 MPa results in yielding during the first cycle with little accumulated permanent strain as shown in Figure 30. The mean and range of two 30 min thermal residual stress relaxation profiles are shown in addition to the axial and transverse data from the dogbone specimen.

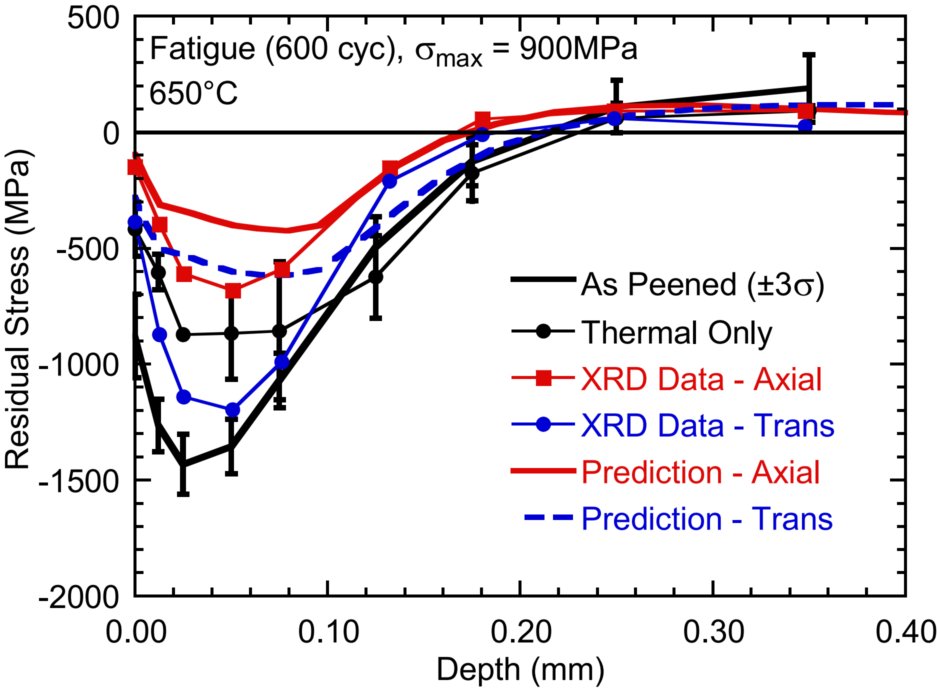

Figure 52. Prediction for Retained Residual Stresses in Shot Peened Dogbone Specimen from 600 Cycles in IN100 at 900MPa and 650°C.

In this case, the 30 min thermal only profiles display a large range in stresses near the peak compressive stress. Overall the predictions capture the surface residual stress while over-predicting relaxation of peak compressive stresses.

Predictions for retained residual stresses under fatigue loading of 12,000 cycles (10 hr) are shown in Figure 53. The maximum applied stress of 900 MPa results in yielding during the first cycle with slightly more accumulated permanent strain than the 600 cycle test, shown in Figure 30. Again, two thermal residual stress relaxation profiles are averaged and shown as a mean and range in addition to the axial and transverse data from the dogbone specimen.

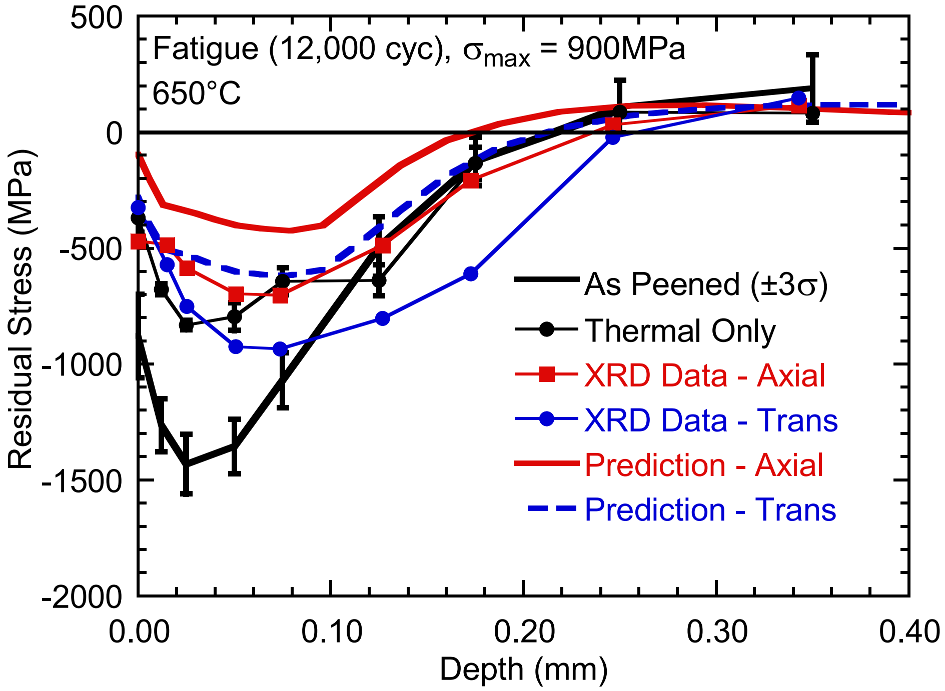

Figure 53. Prediction for Retained Residual Stresses in Shot Peened Dogbone Specimen from 12,000 Cycles in IN100 at 900 MPa and 650°C.

In this instance, the 10 hr thermal only profiles are similar, in contrast to the large difference observed in the 30 min profiles. Overall, the predictions accurately capture the surface residual stress while over-predicting relaxation of peak compressive stresses. In summary, residual stress profiles subject to fatigue loading demonstrate that most of the residual stress relaxation associated with fatigue occurs during the first loading cycle, coincident with the largest change in plastic strain. The small amount of accumulated plastic strain during fatigue does little to change the residual stress profile with increasing cycles.

Predictions for retained residual stresses under sustained load (creep) loading for 30 min are shown in Figure 54. The maximum applied stress of 900 MPa results in yielding during loading.

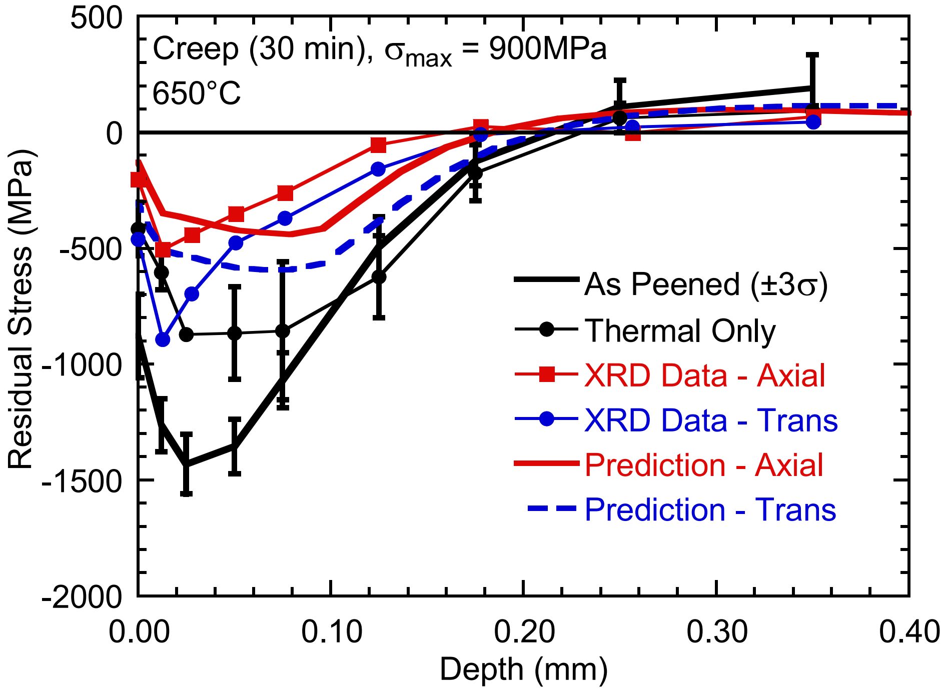

Figure 54. Prediction for Retained Residual Stresses in Shot Peened Dogbone Specimen from 30 Min Creep in IN100 at 900 MPa and 650°C.

Unloading after 30 min of sustained loading reveal more accumulated permanent strain than that observed for 600 cycle fatigue loading for the same exposure time. The predictions capture the surface residual stress and peak compressive stresses in the axial orientation, and to a lesser degree in the transverse orientation. Both the axial and transverse profile measurements display a sharp point for the peak compressive residual stress, which is possibly an artifact of the XRD data reduction, and hence is not captured in the predictions. For sustained loading of 10 hr at the same applied maximum stress of 900 MPa the retained residual stresses are less as shown in Figure 55. Again, the experimental data exhibit a sharp peak compressive residual stress in both axial and transverse profiles. The prediction for the residual stress in the axial orientation is captured accurately, while the transverse prediction displays less retained compressive stress than the reported measurement.

Clearly creep loading is more detrimental than fatigue loading to retained compressive residual stresses from shot peening for applied stresses that develop plastic strain during loading. Additional fatigue cycling does not appear to change the residual stress profile beyond what occurs during the first cycle, whereas sustained loading continues to relax residual stresses with increasing creep time. Although significant relaxation of compressive residual stresses occurs during creep relative to that of fatigue the surface residual stress remains compressive. This is relatively surprising since analysis of the creep strain data for the 10 hr creep test revealed that the specimen was in tertiary creep and close to failure when the test was stopped.

For applied stresses that do not result in plastic deformation during loading, any relaxation must be controlled by thermally activated creep deformation. To promote measurable relaxation results the exposure times were increased to 100 hrs for creep tests below yield. In particular, Figures 56 and 57, 600 MPa tensile and 300 MPa compressive creep tests, respectively, were completed to access the effect of plastic strain on relaxation of residual stresses. For both tensile and compressive creep loading without plastic strain, the axial and transverse profiles are similar. In particular the 600 MPa tensile creep loading does exhibit slightly more relaxation for the axial orientation, while the 300 MPa compressive creep profiles are almost identical. Furthermore, the profiles are very similar to the profile for thermal exposure only. The predicted profiles for tensile and compressive creep are in excellent agreement with measured results.

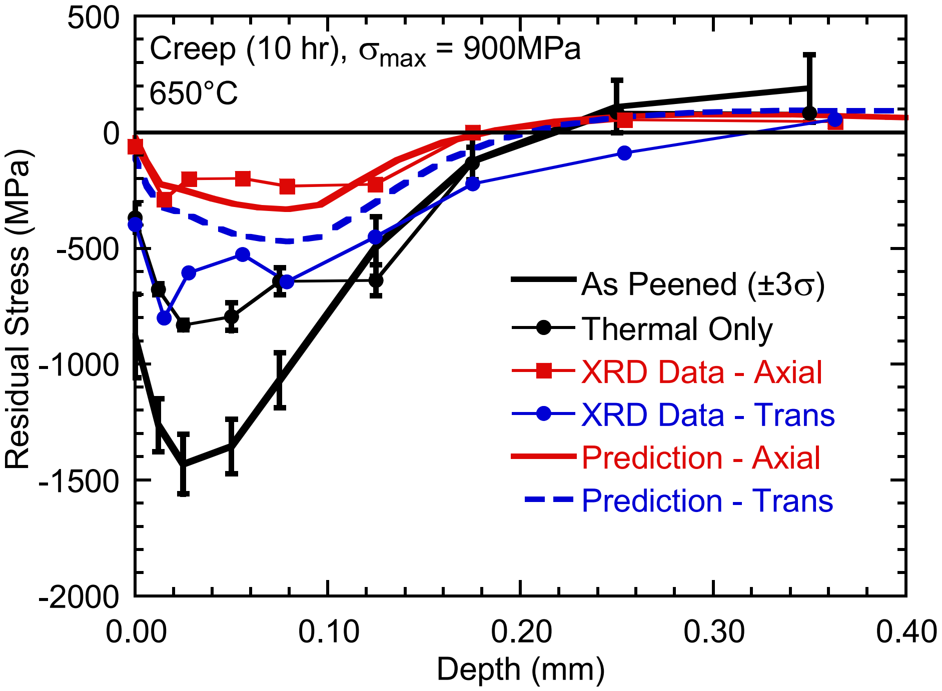

Figure 55. Prediction for Retained Residual Stresses in Shot Peened Dogbone Specimen from 10 hr Creep in IN100 at 900 MPa and 650°C.

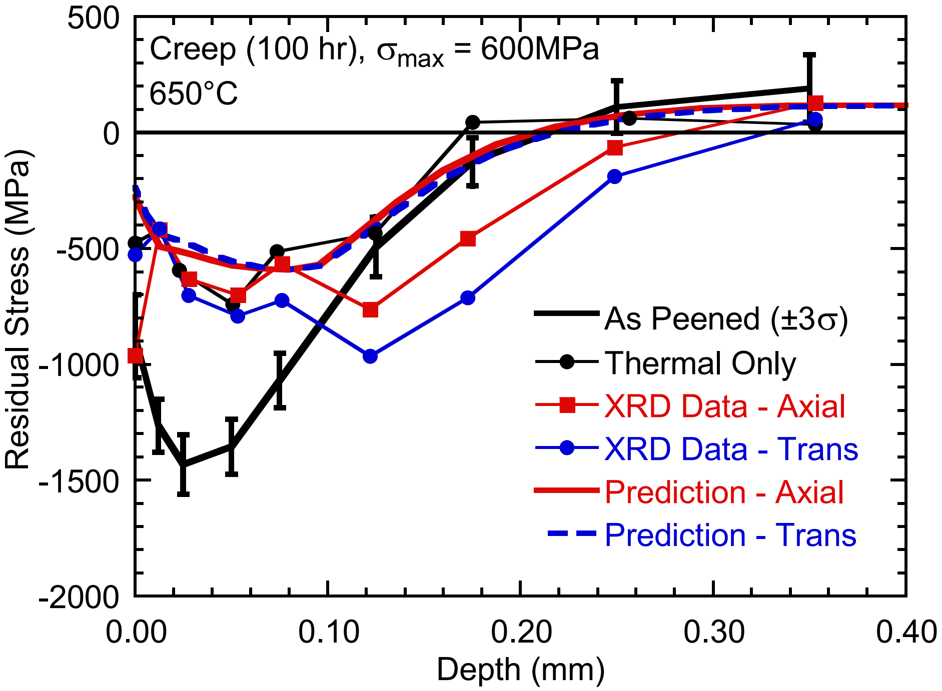

Figure 56. Prediction for Retained Residual Stresses in Shot Peened Dogbone Specimen from 100 hr Creep in IN100 at 600 MPa and 650°C.

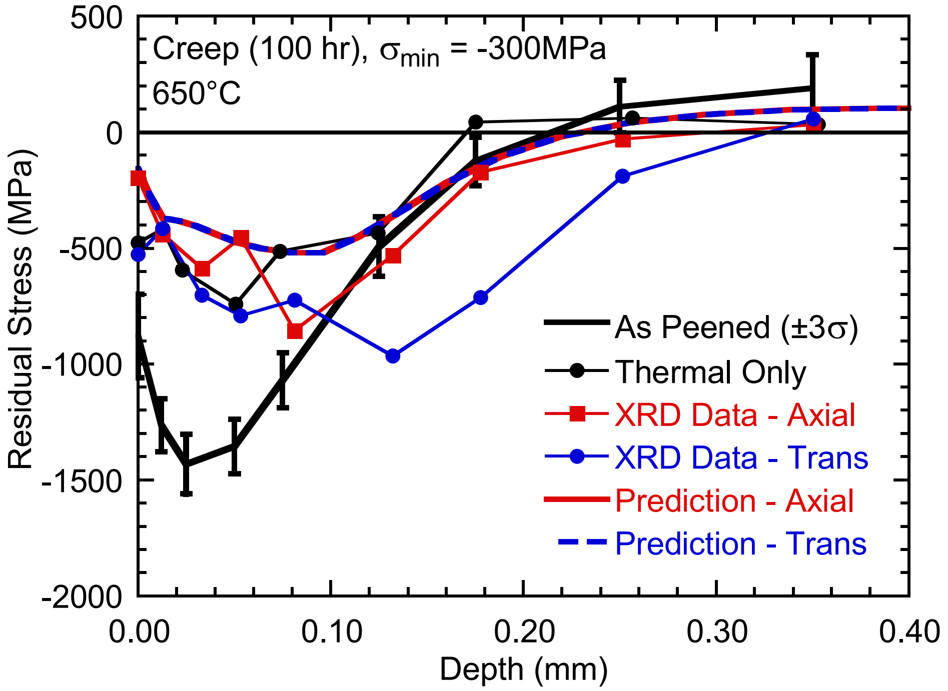

Figure 57. Prediction for Retained Residual Stresses in Shot Peened Dogbone Specimen from 100 hr Creep in IN100 at -300 MPa and 650°C.

An additional creep test on a shot peened flat dogbone sample has been performed at an applied stress of 800 MPa for 10 hr. This is the maximum stress level that could be reached without producing significant plastic strain during loading. The loading and unloading stress strain behavior is shown in Figure 35, which shows that the 800 MPa 10hr creep test results in slightly more accumulated plastic strain than the single cycle 900MPa test. The resulting depth profile is shown in Figure 58 along with the thermal exposure depth profile for comparison. It is clear that the 800 MPa 10 hr creep test retains a significant portion of the residual stress profile similar to the thermal exposure profiles. This result is expected since creep behavior on unpeened cylindrical dogbone samples has shown that this superalloy exhibits little or no creep below 800 MPa and 650°C. Although the 800 MPa 10 hr creep test exhibits slightly higher accumulated inelastic strain after unloading it retained a higher compressive peak residual stress than the 900 MPa single cycle test.

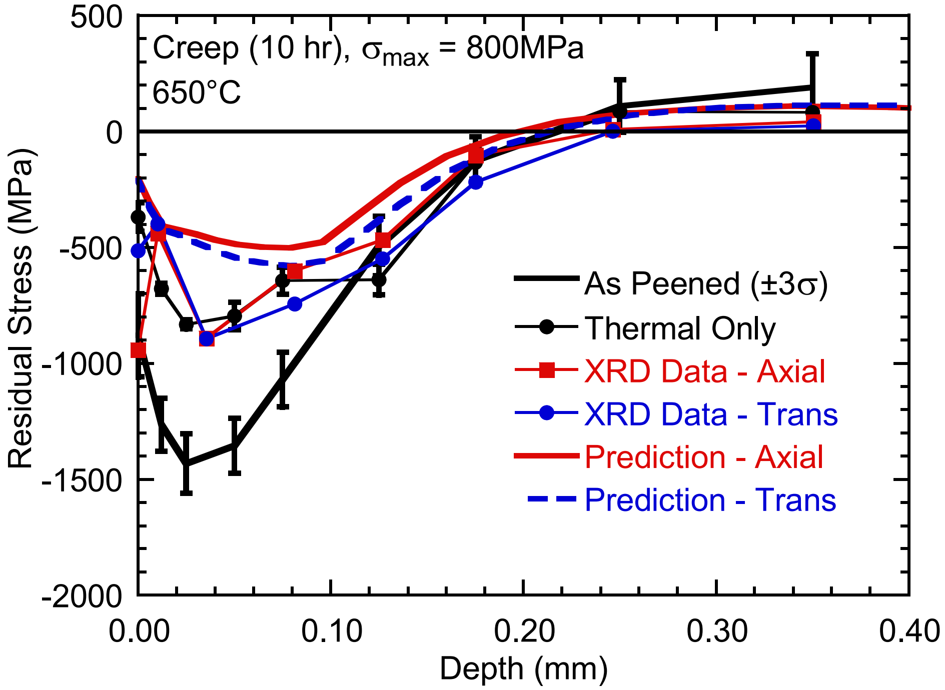

Figure 58. Prediction for Retained Residual Stresses in Shot Peened Dogbone Specimen from 10 hr Creep in IN100 at 800 MPa and 650°C.

CHAPTER VI

CONCLUSIONS AND RECOMMENDATIONS

Shot peening has been employed for decades in many industries to impart compressive surface residual stresses into components for the purpose of improving fatigue life. Aircraft turbine engine components are routinely shot-peened at fracture critical locations for this reason. However, relaxation of residual stresses due to thermal exposure and fatigue loading has prevented designers from incorporating the beneficial effects of shot peening into fatigue crack initiation and fatigue crack growth life predictions used for design and life extension. Furthermore, relaxation of residual stress under sustained loads (creep) has been ignored. Advances in surface treatment processes such as LSP and LPB enable compressive residual stresses to be pushed deeper into the material, and with claims of less cold work (plastic strain) than traditional shot peening. Existing models calibrated for shot peening do not account for differences in plastic strain and yield surface, and cannot predict relaxation accurately. The present model has been shown to capture the material response under complex loading histories in which inelastic prestrain affects primary and secondary creep response. Conclusions resulting from the work in this study and recommendations for future research are detailed below. The integrated experimental and analytical research approach described in the present study to characterize residual stress relaxation in shot-peened IN100 can be applied directly to similar high-temperature nickel-base superalloy materials.

Conclusions

A new coupled creep-plasticity model that incorporates plastic strain and yield surface state variables has been developed, and used successfully for predicting residual stress relaxation in shot-peened IN100. This model reflects the correct dominant deformation mechanism identified for relaxation of shot-peened residual stresses and therefore provides the capability to model relaxation of other surface treatment processes such as LSP and LPB. Creep and plasticity are identified and modeled as different deformation mechanisms, coupled together through state variables representing the evolution of the microstructure during deformation. This treatment is contrary to unified models that treat plasticity and creep as the same deformation mechanism grouped into a single rate equation. The coupled creep-plasticity approach facilitates incorporation of other creep deformation mechanisms into the model without extensive additional experimental testing and calibration.

Tensile, creep and cyclic tests have been completed to characterize the baseline IN100 material at room and elevated temperature. Creep tests with prior room temperature prestrain demonstrate the effect plastic strain has on primary and secondary creep rate behavior. Statistical analysis of the baseline material characterization and material models have been completed and discussed. The proposed model has been demonstrated to give accurate predictions for stress relaxation under complex loading histories.

Two specimen geometries have been used to evaluate relaxation of shot-peened residual stresses. The thermal relaxation geometry covers a range of temperatures and exposure times, and provides a baseline comparison for effects of mechanical loading. Since no mechanical loading was applied to these specimens, relaxation is entirely creep driven. Applied mechanical loading on shot-peened dogbone samples incorporates plastic material behavior into the process of residual stress relaxation. For applied stresses that produce plastic strain during loading, there is a significant decrease in retained residual stresses. Under fatigue loading, no additional residual stress relaxation is observed with additional cycles beyond the first cycle, whereas creep loading continued to cause relaxation with increasing loading time. For applied stress that does not produce plastic strain during loading, residual stress relaxation is similar to that of thermal exposure only. Predictions for residual stress relaxation subject to mechanical loading are in agreement with measured residual stress profiles from x-ray diffraction. The model developed in this study provides the flexibility to simulate relaxation of other surface treatment processes provided they are driven by a dislocation deformation mechanism.

Recommendations

This study has focused on shot-peened residual stresses in IN100. However, the model developed herein can provide predictions for other surface treatment processes with different levels of cold work (plastic strain). A new study is currently being planned to investigate thermal residual stress relaxation in IN100 with LSP surface treatment. A similar thermal exposure test matrix to that discussed in the present study is planned for LSP surface treated samples. LSP has a much deeper level of compressive residual stress with less cold work. The thermal relaxation data from LSP will provide a good test of the predictive capability of the coupled creep-plasticity model.

This study has focused on the effects of plastic strain on relaxation behavior at 650°C. At higher temperatures creep deformation will become more dominant than plastic deformation, while at lower temperatures creep deformation will cease and plastic deformation will dominate. Investigating both higher and lower temperatures will provide insight into the relative contributions of creep and plastic deformation on residual stress relaxation.

All the experiments and analysis in this study have been completed on specimens, subject to externally applied loads, over a uniform cross section. These specimens have large flat areas that enable simple XRD measurements for comparison with model predictions. The next step for further evaluation of this model is application to notched samples that provide a strain gradient at the notch in addition to the plastic strain gradient associated with the surface treatment. The results of these experiments and analyses on notched samples will demonstrate the effectiveness of surface treatment to retain compressive surface residual stresses at fracture critical locations.

Finally, it is recommended that the present relaxation model be incorporated into existing fatigue crack initiation and fatigue crack life prediction codes. Only when residual stress relaxation is accurately modeled and correctly predicted will life prediction design methods be able to take credit for residual stresses and provide reasonable estimates of remaining life.

REFERENCES

1. Miller, H. E., and Chambers, W. L., "Gas Turbine Design and Superalloys," in Superalloys II, High-Temperature Materials for Aerospace and Industrial Power, Eds. C. T. Sims, N. S. Stoloff, and W. C. Hagel, John Wiley & Sons, Inc., New York, 1987, pp. 27-57.
2. Happ, M. B., Mourer, D. P., and Schmidt, R. L., "Residual stress analysis and LCF test results for peened bolt hole and dovetail configurations," Proceedings of ASM's Conference on Residual Stress – In Design, Process and Materials Selection, Ed. William B. Young, Cincinnati, OH, April 1987, pp. 127-136.
3. Happ, M. B., "Shot Peening Bolt Holes in Aircraft Engine Hardware," Proceedings Second International Conference on Shot Peening, 1984, pp. 43.
4. Vukelich, S., Berkley, S., Russ, S., and Bradley, E. F., "Residual stress measurement and its application to achieve predicted full life potential of low cycle fatigue (LCF) engine disks," The 9th International Symposium on Transport Phenomena and Dynamics of Rotating Machinery, Honolulu, Hawaii, February 2002.
5. Prevéy, P., Hornbach, D., and Mason, P., "Thermal residual stress relaxation and distortion in surface enhanced gas turbine engine components," Proceedings of the 17th Heat Treating Society Conference and Exposition and the 1st International Induction Heat Treating Symposium, Eds. D.L. Milam et.al., ASM Materials Park, OH, 1998, pp. 3-12.
6. Gabb, T. P., Telesman, J., Kantos, P. T., Bonacuse, P. J., Barrie, R. L., and Hornbach, D. J., "Stress Relaxation in Powder Metallurgy Superalloy Disks," TMS Letters, The Minerals, Metals & Materials Society, 2004.
7. Lu, J., Flavenot, J. F., and Turbat, A., "Prediction of Residual Stress Relaxation During Fatigue," Mechanical Relaxation of Residual Stresses, ASTM STP 993, Ed. L. Mordfin, American Society for Testing and Materials, Philadelphia, PA, 1988, pp. 75-90.
8. Landgraf, R. W., and Chernenkoff, R. A., "Residual stress effects on fatigue of surface processed steels," Analytical and Experimental Methods for Residual Stress Effects in Fatigue, ASTM STP 1004, Eds. R. L. Champoux, J. H. Underwood, and J. A. Kapp, American Society for Testing and Materials, Philadelphia, PA, 1988, pp. 1-12.
9. Zhuang, W. Z., and Halford, G. R., "Investigation of residual stress relaxation under cyclic load," International Journal of Fatigue, Vol. 23, 2001, pp. S31-S37.
10. Diesner, R. W., "The Effect of Elevated Temperature Exposure on Residual Stresses," SAE Technical Paper No. 710285, SAE, 1971.

11. Childs, W. H., "The Effect of Elevated Temperature on Shot Peened 403 Stainless Steel," Analytical and Experimental Methods for Residual Stress Effects in Fatigue, ASTM STP 1004, Eds. R. L. Champoux, J. H. Underwood, and J. A. Kapp, American Society for Testing and Materials, Philadelphia, PA. 1988, pp. 21-24.
12. Ahmad, J., Chandu, S., Kroupa, J., and Prevéy, P., "An assessment of residual stresses induced by surface treatments," Proceedings of the 6th National Turbine Engine High Cycle Fatigue Conference, HCF 2001, Jacksonville, FL., March 2001.
13. Khadhraoui, M., Cao, W., Brenier, B., Castex, L., and Guédou, J. Y., "Experimental investigation and modeling of relaxation behavior of shot peening residual stresses at high temperature for nickel base superalloys," Material Science and Technology, Vol. 13, April 1997, pp. 360-367.
14. Cao, W., Khadhraoui, M., Brenier, B., Guédou, J. Y., and Castex, L., "Thermomechanical relaxation of residual stress in shot peened nickel base superalloy," Material Science and Technology, Vol. 10, November 1994, pp. 947-954.
15. Fathallah, R., Inglebert, G., and Castex, L., "Prediction of plastic deformation and residual stresses induced in metallic parts by shot peening," Material Science and Technology, Vol. 14., July 1998, pp. 631-639.
16. Prevéy, P., "The measurement of subsurface residual stress and cold work distributions in nickel base alloys," Proceedings of ASM's Conference on Residual Stress – In Design, Process and Materials Selection, Ed. William B. Young, Cincinnati, OH, April 1987, pp. 11-19.
17. Schulze, V., Vöhringer, O., and Macherauch, E., "Thermal relaxation of shot peened residual stresses in a quenched and tempered steel 42 Cr Mo 4," Proceedings of the Fifth International Conference on Shot Peening, Christ Church Oxford University, 1993, pp. 265-274.
18. Hoffman, J., Scholtes, B., Vöhringer, O., and Macherauch, E., "Thermal relaxation of shot peened residual stresses in the differently heat treated plain carbon steel Ck 45," Proceedings of the Third International Conference on Shot Peening, Eds. H. Wohlfahrt, R. Kopp and O. Vöhringer, Garmisch-Partenkirchen (FRG), 1987, pp. 239-247.
19. Vöhringer, O., "Relaxation of residual stresses," Proceedings of the European Conference on Residual Stresses, Eds. E. Macherauch and V. Hauk, Translated from the German by Janet Mordike, Karlsruhe, 1983, pp. 47-80.
20. Holzapfel, H., Schulze, V., Vöhringer, O., and Macherauch, E. "Residual stress relaxation in an AISI 4140 steel due to quasistatic and cyclic loading at higher temperatures," Material Science and Engineering A248, 1998, pp. 9-18.
21. Smith D. J., Farrahi, G. H., Zhu, W. X., and McMahon, C. A., "Experimental measurement and finite element simulation of the interaction between residual stresses and mechanical loading," International Journal of Fatigue, Vol. 23, 2001, pp. 293-302.
22. Schulze, V., "Characteristics of Surface Layers Produced by Shot Peening," Proceedings of the Eight International Conference on Shot Peening in Garmisch-Partenkirchen, Germany, Ed. L. Wagner, September 2002, pp. 145-160.

23. Prevéy, P., "The Effect of Cold Work on the Thermal Stability of Residual Compression in Surface Enhanced 718," Proceedings of the 20th ASM Materials Solution Conference & Exposition, St. Louis, Missouri, 2000.

24. Luo, J., and Bowen, P., "Effects of Temperature and Shot Peening on S-N Behavior of a PM Ni-Base Superalloy UDIMET 720," Metallurgical and Materials Transactions A, Vol. 35A, March 2005, pp. 1007-1016.

25. Buchanan, D. J., John, R., and Ashbaugh, N. E., "Thermal Residual Stress Relaxation in Powder Metal IN100 Superalloy," Journal of ASTM International, Vol. 3, No. 5, March 2006.

26. Drechsler, A., Kiese, J., and Wagner, L., "Effects of Shot Peening and Roller-Burnishing on Fatigue Performance of Various Titanium Alloys," Proceedings of the Seven International Conference on Shot Peening in Warsaw, Poland, 1999, pp. 145-152.

27. Prevéy, P., "Problems with Non-Destructive Surface X-Ray Diffraction Residual Stress Measurement," in Practical Applications of Residual Stress Technology, Ed. C. Ruud, American Society for Metals, Materials Park, OH, 1991, pp. 47-54.

28. Chaboche, J. L., and Jung, O., "Application of a Kinematic Hardening Viscoplasticity Model with Thresholds to the Residual Stress Relaxation," International Journal of Plasticity, Vol. 13, No. 10, 1998, pp. 785-807.

29. Conrad, H., "Experimental Evaluation of Creep and Stress Rupture," in Mechanical Behavior of Materials at Elevated Temperatures, Ed. J. E. Dorn, McGraw-Hill Book Company, Inc., New York, 1961, pp. 149-217.

30. Evans, R. W., and Wilshire, B., Creep of Metals and Alloys, The Institute of Metals, London, 1985.

31. Schoeck, G., "Theories of Creep," in Mechanical Behavior of Materials at Elevated Temperatures, Ed. J. E. Dorn, McGraw-Hill Book Company, Inc., New York, 1961, pp. 79-107.

32. Hertzberg, R. W., Deformation and Fracture Mechanics of Engineering Materials, 4th Edition, John Wiley & Sons, Inc., New York, 1996.

33. McClintock, F. A., and Argon, A. S., Mechanical Behavior of Materials, Addison-Wesley Publishing Company, Inc., New York, 1966.

34. Kennedy, A. J., Processes of Creep and Fatigue in Metals, John Wiley & Sons, Inc., New York, 1963.

35. Lubahn, J. D., and Felgar, R. P., Plasticity and Creep of Metals, John Wiley & Sons, Inc., New York, 1961.

36. Mendelson, A., Plasticity: Theory and Applications, The Macmillan Company, New York, 1968.

37. Kraus, H., Creep Analysis, John Wiley & Sons, Inc., New York, 1980.

38. Skrzypek, J. J., (Hetnarski, R. B., English Edition Editor), Plasticity and Creep: Theory, Examples, and Problems, CRC Press, Boca Raton, FL, 1993.

39. Penny, R. K., and Marriot, D. L., Design for Creep, 2nd Edition, Chapman & Hall, New York, 1995.

40. Ashby, M. F., and Frost, H. J., "The Kinetics of Inelastic Deformation above 0°K," in Constitutive Equations in Plasticity, Ed. A. S. Argon, The MIT Press, Cambridge, Massachusetts, 1975, pp. 117-147.

41. Shames, I. H, and Cozzarelli, F. A., Elastic and Inelastic Stress Analysis, Revised Printing, Taylor & Francis, Philadelphia, PA, 1997.

42. Findley, W. N., Lai, J. S., and Onaran, K., Creep and Relaxation of Nonlinear Viscoelastic Materials, Dover Publications, Inc., New York, 1989, Original Edition published by North-Holland Publishing Co., 1976.

43. Dowling, N. E., Mechanical Behavior of Materials, Prentice-Hall Inc., Englewood Cliffs, New Jersey, 1993.

44. Bannantine, J. A., Comer, J. J. and Handrock, J. L., Fundamentals of Metal Fatigue Analysis, Prentice Hall, 1990.

45. Khan, A. S., and Huang, S., Continuum Theory of Plasticity, John Wiley & Sons, Inc., New York, 1995.

46. Wallis, R. A., and Craighead, I. W., “Predicting Residual Stresses in Gas Turbine Components,” Journal of the Minerals, Metals & Materials Society (JOM), 1995, pp. 69-71.

47. Furrer, D., and Fecht, H., “Ni-Based Superalloys for Turbine Discs,” Journal of the Minerals, Metals & Materials Society (JOM), January 1999, pp. 14-17.

48. Fecht, H., and Furrer, D., “Processing of Nickel-Base Superalloys for Turbine Engine Disc Applications,” Advanced Engineering Materials, Vol. 2, No. 12, 2000, pp. 777-787.

49. Ashby, M. F., “A First Report on Deformation-Mechanism Maps,” Acta Metallurgica, Vol. 20, July 1972, pp. 887-897.

50. Mohamed, F. A., and Langdon, T. G., “Deformation Mechanism Maps: Their Use in Predicting Creep Behavior,” Journal of Engineering Materials and Technology, 1975, pp. 1-6.

51. Pelloux, R. M., and Vasatis, I., “Creep Damage: A Review of Past and Current Work,” Advanced High-Temperature Alloys: Processing and Properties, Proceedings of the Nicholas J. Grant Symposium, Processing and Properties of Advanced High-Temperature Alloys, MIT Cambridge, Massachusetts, Published by American Society for Metals, June 1985, pp. 165-175.

52. Cuitiño, A. M., “A Time-Dependent Deformation Mechanism in Metallic f.c.c. Crystals,” Acta Mater., Vol. 45, No. 6, 1997, pp. 2509-2522.

53. Nategh, S., and Sajjadi, S. A., “Dislocation network formation during creep in Ni-base superalloy GTD-111,” Material Science and Engineering, Vol. A339, 2003, pp. 103-108.

54. Hide, N. J., Henderson, M. B., and Reed, P. A. S., “Effects of Grain and Precipitate Size Variation on Creep-Fatigue Behavior of UDIMET 720LI in Both Air and Vacuum,” Superalloys 2000, Eds. T.M. Pollock, R.D. Kissinger, J.J. Schirra, Published by The Minerals, Metals & Materials Society, 2000, pp. 495-503.

55. Nazmy, M., Denk, J., Baumann, R., and Künzler, A., “Environmental effects on tensile and low cycle fatigue behavior of single crystal nickel base superalloy,” Scripta Materialia, Vol. 48, 2003, pp. 519-524.

56. Vasudevan, A. K., Sadananda, K., and Glinka, G., “Critical parameters for fatigue damage,” International Journal of Fatigue, Vol. 23, 2001, pp. S39-S53.

57. Haugsrud, R., “On the high-temperature oxidation of nickel,” Corrosion Science, Vol. 45, 2003, pp. 211-235.

58. Mannan, S., Patel, S., and deBarbadillo, J., “Long Term Thermal Stability of INCONEL Alloys 718, 706, 909, and Waspaloy at 593°C and 704°C,” Superalloys 2000, Eds. T.M. Pollock, R.D. Kissinger, J.J. Schirra, Published by The Minerals, Metals & Materials Society, 2000, pp. 449-458.

59. Webster, G. A., and Piearcey, B. J., “An Interpretation of the Effects of Stress and Temperature on the Creep Properties of a Nickel-Base Superalloy,” Metal Science Journal, Vol. 1, 1967, pp. 97-107.

60. Miner, R. V., Gayda, J., and Maier, R. D., “Fatigue and Creep-Fatigue Deformation of Several Nickel-Base Superalloys at 650°C,” Metallurgical Transactions A, Vol. 13A, October 1982, pp. 1755-1765.

61. Brown, S. G. R., Evans, R. W., and Wilshire, B., “Creep Strain and Creep Life Prediction for the Cast Nickel-based Superalloy IN-100,” Material Science and Engineering, Vol. 84, 1986, pp. 147-156.

62. Nowick, A. S., and Machlin, E. S., “Quantitative Treatment of the Creep of Metals by Dislocation and Rate Process Theories,” National Advisory Committee for Aeronautics (NACA), Technical Note No. 1039, April 1946.

63. Machlin, E. S., “Dislocation Theory of the Fatigue of Metals,” National Advisory Committee for Aeronautics (NACA), Technical Note No. 1489, January 1948.

64. Weertman, J., “Theory of Steady-State Creep Based on Dislocation Climb,” Journal of Applied Physics, Vol. 26, No. 10, October 1955, pp. 1213-1217.

65. Weertman, J., “Steady-State Creep through Dislocation Climb,” Journal of Applied Physics, Vol. 28, No. 3, March 1957, pp. 362-364.

66. Kelly, J. M., and Gillis, P. P., “Thermodynamics and Dislocation Mechanics,” Journal of The Franklin Institute, Vol. 297, No. 1, January 1974, pp. 59-74.

67. Brehm. H., and Daehn, G. S., “A Framework for Modeling Creep in Pure Metals,” Metallurgical and Materials Transactions A, Vol. 33A, February 2002, pp. 363-371.

68. Hiratani, M., Zbib, H. M., and Khaleel, M. A., “Modeling of thermally activated dislocation glide and plastic flow through local obstacles,” International Journal of Plasticity, Vol. 19, 2003, pp. 1271-1296.

69. Kachanov, L. M., “Time of the Rupture Process Under Creep Conditions,” Izv. Akad. Nauk. SSR, Otd Tekh., Nauk No. 8, 1958, pp. 26-31.

70. Rabotnov, Y. N., Creep Problems in Structural Members, North Holland, Amsterdam, 1969.

71. Chaboche, J. L., “Continuum Damage Mechanics: Part I – General Concepts,” Journal of Applied Mechanics, Vol. 55, March 1988, pp. 59-64.

72. Chaboche, J. L., “Continuum Damage Mechanics: Part II – Damage Growth, Crack Initiation, and Crack Growth,” Journal of Applied Mechanics, Vol. 55, March 1988, pp. 65-72.

73. Sanders, D. R., “A Comparison of Several Creep Constitutive Theories for the Prediction of Elastic-Plastic-Creep Response and Their Application to Finite Element Analysis,” Ph.D. Thesis, Texas A&M University, 1986.

74. Derby, B., and Ashby, M. F. “A Microstructural Model for Primary Creep,” Acta Metallurgica, Vol. 35, No. 6, 1987, pp. 1349-1353.

75. Barbosa, A., Taylor, N. G., Ashby, M. F., Dyson, B. F., McLean, M., “A Model Based Computer Analysis of Creep Data (CRISPEN): Applications to Nickel-Base Superalloys,” Superalloys 1988, Eds. S. Reichman, D. N. Duhl, G. Maurer, S. Antolovich and C. Lund, The Metallurgical Society, 1988, pp. 683-692.

76. McLean, M. and Dyson, B. F., “Modeling the Effects of Damage and Microstructural Evolution on the Creep Behavior of Engineering Alloys,” Journal of Engineering Materials and Technology, Vol. 122, July 2000, pp. 273-278.

77. Dyson, B. F., “Use of CDM in Materials Modeling and Component Creep Life Prediction,” Journal of Pressure Vessel Technology, Vol. 122, August 2000, pp. 281-296.

78. Sondhi, S. K., Dyson, B. F., and McLean, M. “Tension-Compression creep asymmetry in a turbine disc superalloy: roles of internal stress and thermal ageing,” Acta Materialia, 52, 2004, pp. 1761-1772.

79. Basoalto, H., Sondhi, S. K., Dyson, B. F., and McLean, M. “A Generic Microstructure-Explicit Model of Creep in Nickel-Base Superalloys,” Superalloys 2004, Eds. K. A. Green, T. M. Pollock, H. Harada, T. E. Howson, R. C. Reed, J. J. Schirra and S. Walston, The Minerals, Metals, & Materials Society, 2004, pp. 897-906.

80. Bodner, S. R., “Constitutive Equations for Elastic-Visocplastic Strain-Hardening Materials,” Journal of Applied Mechanics, Transactions of the ASME, June 1975, pp. 385-389.

81. Walker, K., “Research and Development Program for Nonlinear Structural Modeling with Advanced Time-Temperature Dependent Constitutive Relationships,” NASA Contractor Report, NASA-CR-165533, 1981.

82. Ramaswamy, V. G., “A Constitutive Model for the Inelastic Multiaxial Cyclic Response of a Nickel Base Superalloy René 80,” NASA Contractor Report 3998, 1986.

83. Robinson, D. N., “A Unified Creep-Plasticity Model for Structural Metals at High Temperature,” ORNL TM-5969, October, 1978.

84. Miller, A. K., “An Inelastic Constitutive Model for Monotonic, Cyclic, Creep Deformation: Part I – Equations Development and Analytical Procedures; Part II – Applications to Type 304 Stainless Steel,” Trans. ASME Journal of Engineering Materials and Technology, Vol. 96, 1976, pp. 97.

85. Larson, F. R., and Miller, J., “A Time-Temperature Relationship for Rupture and Creep Stresses,” Trans. ASME, Vol., 74, 1952, pp.765-771.

86. Avrami, M. J., J. Chem. Phys., Vol. 7, 1939, pp.1103-1112.

87. John, R., Larsen, J. M., Buchanan, D. J., and Ashbaugh, N. E., "Incorporating Residual Stresses in Life Prediction of Turbine Engine Components," Fatigue, 2002.

88. Hartman, G. A., Ashbaugh, N. E., and Buchanan, D. J., "A sampling of mechanical test automation methodologies used in a basic research laboratory," Automation in fatigue and fracture: testing and analysis, ASTM STP 1231, Ed. C. Amzallag, American Society for Testing and Materials, Philadelphia, PA, 1994, pp. 36-50.

89. Moore, M. G., and Evans, W. P., "Correction for Stress Layers in X-Ray Diffraction Residual Stress Analysis," SAE Transactions, Vol. 66, 1958, pp.340-345.

90. Dodds, R. H., "Numerical Techniques for Plasticity Computations in Finite Element Analysis," Computers & Structures, Vol. 26, No. 5, 1987, pp. 767-779.

91. Standard Guide for Use of Thermocouples in Creep and Stress-Rupture Testing to 1800°F (1000°C) in Air, E633-00, ASTM Vol. 03.01.

92. Standard Test Method for Elevated Temperature Tension Tests of Metallic Materials, E21-03a, ASTM Vol. 03.01.

93. Standard Test Methods for Conducting Creep, Creep-Rupture, and Stress-Rupture Tests of Metallic Materials, E139-00, ASTM Vol. 03.01.

94. Standard Practice for Strain-Controlled Fatigue Testing, E606-04, ASTM Vol. 03.01.

95. Standard Test Method for Verifying the Alignment of X-Ray Diffraction Instrumentation of Residual Stress Measurement, E915-96, ASTM Vol. 03.01.

96. Standard Test Method for Determining the Effective Elastic Parameter X-Ray Diffraction Measurements of Residual Stress, E1426-98, ASTM Vol. 03.01.

97. Residual Stress Measurement by X-Ray Diffraction, SAE J784a, ed. M.E. Hilley, Soc. Auto. Eng., Warrendale, PA, 19, 1971.

98. Shot Peening Applications, 8th edition, Metal Improvement Company, Inc., a subsidiary of Curtiss-Wright Corporation, Paramus, New Jersey.

99. Li, K., Ashbaugh, N. E., and Rosenberger, A. H., "Crystallographic Initiation of Nickel-Base Superalloy IN100 at RT and 538°C Under Low Cycle Fatigue Conditions," Superalloys 2004, Eds. K. A. Green, T. M. Pollock, H. Harada, T. E. Howson, R. C. Reed, J. J. Schirra, and S. Walston, TMS, 2004, pp. 251-258.

100. Davies, P. W., Finniear, T. C., and Wilshire, B., "The Effect of Compressive Prestrain on the Creep and Fracture Properties of Pure Nickel at 500°C," Journal of the Institute of Metals, Vol. 91, 1963, pp. 289-292.

101. Parker, J. D., and Wilshire, B., "The Effects of Prestrain on the Creep and Fracture Behavior of Polycrystalline Copper," Material Science and Engineering, Vol. 43, 1980, pp. 271-280.

102. Burt, H., Elliott, I. C., and Wilshire, B., "Effects of room-temperature prestrain on creep-fracture behavior of Nimonic 105," Metal Science, Vol. 15, September 1981, pp. 421-424.

103. Ellyin, F., and Xia, Z., "A Rate-Dependent Inelastic Constitutive Model – Part I: Elastic-Plastic Flow," Journal of Engineering Materials and Technology, Transactions of the ASME, Vol. 113, July 1991, pp. 314-323.

104. Xia, Z., and Ellyin, F., "A Rate-Dependent Inelastic Constitutive Model – Part II: Creep Deformation Including Prior Plastic Strain Effects," Journal of Engineering Materials and Technology, Transactions of the ASME, Vol. 113, July 1991, pp. 324-328.

105. Engine Structural Integrity Program (ENSIP), MIL-HDBK-1783B, September, 2004, pp. 124.

106. IMSL, Problem-Solving Software Systems, User's Manual, Math/Library Version 2.0, Houston, TX, USA, 1996.

107. Microsoft® Office Excel 2003, Part of Microsoft Office Professional Edition, 2003.

108. User Manual for ZENCRACK™ 7.1, Zentech International Ltd., Camberley, Surrey, UK, September 2003.

109. Schwertel, J., and Schinke, B., "Automated Evaluation of Material Parameters of Viscoplastic Constitutive Equations," Journal of Engineering Materials and Technology, Transactions of the ASME, Vol. 118, July 1996, pp. 273-280.

110. Wolberg, J. R., Prediction Analysis, D. Van Nostrand Company, Inc., Princeton, New Jersey, 1967.

111. Neter, J., Wasserman, W., and Kutner, M. H., Applied Linear Regression Models, Richard D. Irwin, Inc., Homewood, IL, 1983.

112. Gerald, C. F., and Wheatley, P. O., Applied Numerical Analysis, 4th Edition, Addison-Wesley Publishing Co., New York, 1989.

113. Armstrong, P. J., and Frederick C. O., "A Mathematical Representation of the Multiaxial Baushhinger Effect," CEGB Report RD/B/N731, Berkeley Nuclear Laboratories, Berkeley, UK, 1966.

114. Johnson, A. E., "The Creep of a Normally Isotropic Aluminum Alloy under Combined Stress Systems at Elevated Temperature," Metallurgia, Vol. 40, 1949, pp. 125.

115. Kennedy, C. R., Harms, W. O., and Douglas, D. A., "Multiaxial Creep Studies on Inconel at 1500°F," J. Basic Eng., Vol. 81, 1959, pp. 599.

116. Norton, F. H., "Creep in Tubular Pressure Vessels," Trans. ASME, 1939, pp. 239.

117. Braisted, W. R., and Brockman, R. A., Laser Shock Peening Analytical Development, UDRI-TR-1999-47, August 1999.

118. Ludwik, P., Elemente der technologishen Mechanik, Springer, Berlin, 1909.

119. Ramberg, W., and Osgood, W. R., "Description of Stress-Strain Curves by Three Parameters," NACA Technical Note, No. 902, July, 1943.

120. Kirk, D., "Effects of Plastic Straining on Residual Stresses Induced by Shot-Peening," Proceedings of the Third International Conference on Shot Peening, Eds. H. Wohlfahrt, R. Kopp and O. Vöhringer, Garmisch-Partenkirchen (FRG), 1987, pp. 213-220.